U.S.N.A. – Trident Scholar project report; no. 293 (2002)

Measurement Methods and Analysis: Forces on Underwater Gliders

by

Midshipmen Benjamin Abraham Drew, Class of 2002
United States Naval Academy
Annapolis, Maryland

Certification of Advisor's Approval

Associate Professor Carl E. Wick
Department of Weapons and Systems Engineering

Acceptance for the Trident Scholar Committee

Professor Joyce E. Shade
Chair, Trident Scholar Committee

USNA-1531-2

REPORT DOCUMENTATION PAGE

Form Approved OMB No. 0704-0188

1. REPORT DATE (DD-MM-YYYY)	2. REPORT TYPE	3. DATES COVERED (FROM - TO)
03-05-2002		xx-xx-2002 to xx-xx-2002

4. TITLE AND SUBTITLE
Measurement Methods and Analysis: Forces on Underwater Gliders
Unclassified

5a. CONTRACT NUMBER
5b. GRANT NUMBER
5c. PROGRAM ELEMENT NUMBER

6. AUTHOR(S)
Drew, Benjamin A. ;

5d. PROJECT NUMBER
5e. TASK NUMBER
5f. WORK UNIT NUMBER

7. PERFORMING ORGANIZATION NAME AND ADDRESS
US Naval Academy
Annapolis, MD21402

8. PERFORMING ORGANIZATION REPORT NUMBER

9. SPONSORING/MONITORING AGENCY NAME AND ADDRESS
,

10. SPONSOR/MONITOR'S ACRONYM(S)
11. SPONSOR/MONITOR'S REPORT NUMBER(S)

12. DISTRIBUTION/AVAILABILITY STATEMENT
APUBLIC RELEASE
,

13. SUPPLEMENTARY NOTES

14. ABSTRACT
See report.

15. SUBJECT TERMS

16. SECURITY CLASSIFICATION OF:			17. LIMITATION OF ABSTRACT	18. NUMBER OF PAGES	19. NAME OF RESPONSIBLE PERSON
a. REPORT	b. ABSTRACT	c. THIS PAGE	Public Release	111	email from USNA, (blank) lfenster@dtic.mil
Unclassified	Unclassified	Unclassified			19b. TELEPHONE NUMBER International Area Code Area Code Telephone Number 703767-9007 DSN 427-9007

REPORT DOCUMENTATION PAGE

Form Approved
OMB No. 074-0188

1. AGENCY USE ONLY (Leave blank)	2. REPORT DATE	3. REPORT TYPE AND DATE COVERED
	3 May 2002	

4. TITLE AND SUBTITLE
Measurement methods and analysis: forces on underwater gliders

5. FUNDING NUMBERS

6. AUTHOR(S)
Drew, Benjamin Abraham

7. PERFORMING ORGANIZATION NAME(S) AND ADDRESS(ES)		8. PERFORMING ORGANIZATION REPORT NUMBER

9. SPONSORING/MONITORING AGENCY NAME(S) AND ADDRESS(ES)		10. SPONSORING/MONITORING AGENCY REPORT NUMBER
US Naval Academy Annapolis, MD 21402		**Trident Scholar project report no. 293 (2002)**

11. SUPPLEMENTARY NOTES

12a. DISTRIBUTION/AVAILABILITY STATEMENT	12b. DISTRIBUTION CODE
This document has been approved for public release; its distribution is UNLIMITED.	

13. ABSTRACT:

Autonomous Underwater Vehicles are unmanned vessel that can used in many applications including offshore oil industry, marine biology research, and salvaging in an effort to replace divers. As today's Naval Explosive Ordinance Disposal Units look for innovative, technological developments in minefield clearance and related missions clearing unexploded ordinance, the further employment of autonomous unmanned vehicles (AUV) is under strong consideration. Instead of developing systems of high complexity and cost, it is worthwhile to investigate the development of low-cost AUVs with more singular and simplistic missions. This research investigates the design of a miniature efficient underwater glider, of dimensions consistent with the proposed mission. Underwater gliding refers to motion in which the force of gravity provides propulsion and steering is maintained by control fins or by controlling the location of the center of gravity. Wings on the vehicle support its weight underwater and subsequently allow horizontal motion. Different configurations of underwater vehicles will be designed in this study in order to develop a methodology for testing and modeling general underwater gliding behavior. The shape of the wings, their angle of attack, body shape, body size, and vehicle velocity will be factors used in formulating efficient underwater vehicle designs. In this paper, the research describes the design and preliminary analysis of several model underwater vehicles, consisting of a cylindrical body and configurable wings, which were built to demonstrate and test dynamics and control of underwater gliding. This Trident Project can later be expanded to build a prototype autonomous underwater glider after the precepts of underwater gliding are understood.

14. SUBJECT TERMS	15. NUMBER OF PAGES
Autonomous underwater vehicles, unmanned vessels, underwater gliders	**111**
	16. PRICE CODE

17. SECURITY CLASSIFICATION OF REPORT	18. SECURITY CLASSIFICATION OF THIS PAGE	19. SECURITY CLASSIFICATION OF ABSTRACT	20. LIMITATION OF ABSTRACT

I ABSTRACT

Autonomous Underwater Vehicles are unmanned vessel that can used in many applications including offshore oil industry, marine biology research, and salvaging in an effort to replace divers. As today's Naval Explosive Ordinance Disposal Units look for innovative, technological developments in minefield clearance and related missions clearing unexploded ordinance, the further employment of autonomous unmanned vehicles (AUV) is under strong consideration. Instead of developing systems of high complexity and cost, it is worthwhile to investigate the development of low-cost AUVs with more singular and simplistic missions.

This research investigates the design of a miniature efficient underwater glider, of dimensions consistent with the proposed mission. Underwater gliding refers to motion in which the force of gravity provides propulsion and steering is maintained by control fins or by controlling the location of the center of gravity. Wings on the vehicle support its weight underwater and subsequently allow horizontal motion. Different configurations of underwater vehicles will be designed in this study in order to develop a methodology for testing and modeling general underwater gliding behavior. The shape of the wings, their angle of attack, body shape, body size, and vehicle velocity will be factors used in formulating efficient underwater vehicle designs. In this paper, the research describes the design and preliminary analysis of several model underwater vehicles, consisting of a cylindrical body and configurable wings, which were built to demonstrate and test dynamics and control of underwater gliding. This Trident Project can later be expanded to build a prototype autonomous underwater glider after the precepts of underwater gliding are understood.

II ACKNOWLEDGMENTS

The author of this report thanks Dr. Carl Wick for serving as the Trident Project Advisor and for providing continuous guidance and insight at the outset of any problems that arose throughout this project. For building the prototype vehicles and offering advice about the construction process, Thomas Price, Dale Boyer, and Bill Beaver of the Technical Support Department deserve my appreciation. In addition, the author thanks Jerry Myers for building the sensor box to the outlined specifications and Gene Miller for welding the different components together to be suspended in water. The author would also like to recognize Bill Lowe, Ralph Wicklund, and Joe Bradshaw of the Weapons and Systems Department for providing the workstation and sensor and control equipment. In the aerodynamics department, the author would like to express gratitude to Asst. Prof David Miklosovic for generating insight and experimental suggestions into the lift and drag coefficients of the glider. Ron Wheeler was also instrumental in scheduling time to use the wind tunnel and mounting the vehicles. The author also thanks Louise Becnel from the Fluid Measurements Lab for providing the honeycomb used to diffuse the water in the recirculation tank and the pitot tubes for measuring the flow rate underwater. For the film footage and videography of the recirculation tank utilized in the presentation, Michael Liskey and Matt McMahon deserve credit and appreciation for their hard work and professionalism. The author also owes a debt of service to Karen Lambert for making the backdrop with title for the poster presentation and Christine Jamison for providing direction on how to improve the aesthetic appeal of the powerpoint presentation. The author also thanks the Trident Scholar Committee and Professor Shade for their unfaltering patience and continual support in lieu of early problems with the project. And finally, the author recognizes Floyd and Wendy Drew for their endless support throughout these past four years at the U.S. Naval Academy.

III Preface

As a leading thinker of naval theory, strategy, and history at the end of the 19th century, Alfred Thayer Mahan was conscious of the growing power of the United States. He thought is had almost unlimited resources and potential. In the context of changing geopolitical realities, Mahan argued that the ability to control the water and high seas are an empirical measurement of military might.

In October of 1950, Mahan's theory proved to be a reality. Suffering seven ship casualties, a 250 ship invasion fleet with 50,000 Marines was held up for seven days past D-Day off Wonsan, Korea. Using pre-World War I technology, laid by vessels that were utilized at the Age of Enlightenment, the world's most powerful navy lost control of the seas to a nation without a Navy, due to mine warfare. Forty years later in May of 1991, the U.S. Navy endured further destruction from mine warfare, rendering three additional ships combat ineffective and again denying the Marines access to beaches in Kuwait. From these reoccurring lessons that never stay learned, mines have finally been recognized as an inexpensive and deadly form of asymmetrical warfare that can inflict damage on military, commercial, or civilian vessels.

As a future officer in the U.S. Navy, the author is channeling his intellectual efforts, intuition, and passion towards a substantial non-textbook problem that seeks to identify a method of developing and testing autonomous underwater vehicles. The application of this understanding will contribute to future technology to map minefields, neutralize mines, and most importantly, reduce risk to human resources.

Imparted with the freedom and independence from a normal classroom routine, this project is pioneering independent graduate level research. The notion of unmanned, unattached, submersible technology offers a multitude of technical problems associated with the design and development of such a complex system. Many of the current AUVs are oversized, which is both inefficient for transport and cumbersome to handle.

In an effort to find a more economical and efficient means of fighting mine warfare, it is imperative that one alters the paradigm and identifies new solutions. Instead of developing a vehicle, which can travel over a large surface area with an immense system of sonar and acoustic sensors, my project explores the facets of a small underwater glider that measures inches in length, maintains the most fundamental mission possible, and covers a relatively small expanse of water. Further applications might entail interoperability, communication, and collaboration between vehicles, possibly saturating areas with hundreds of small, inexpensive and rudimentary AUVs.

Aside from measuring inches in length and weighing less than 2 pounds, the unique element of this research is that the experimental underwater vehicles have no active propulsion. Instead, they rely upon hull shape and wings to glide underwater and conserve energy. The focus of the research has changed from building the control system of an underwater glider to understanding and developing a methodology for testing the behavior of underwater gliders. To date, research in this field has not provided sound reasoning that explains the relationships between fluid dynamics and underwater gliders, furthering the necessity of this research.

In effect, the research of this project will establish the foundation for creating the control system that will make use of this new comprehension in underwater gliding. The data can be used for starting points for modifications to optimize underwater gliding. In finding a solution to the modeling of underwater gliders and different variables of their design, the gliders will be

tested in a water tank, wind tunnel, and recirculation tank. Fundamentally, the knowledge from this report will not only provide new insights as to how to construct an AUV without a propulsion system, but more importantly aid the U.S. Navy in maintaining command of the sea.

IV Report Information

Table of Contents

4.2 Keywords

Angle of Attack – the angle of a body with respect to airflow or water flow

Aspect Ratio – the ratio of span squared to wing area. Early wind tunnel investigations of the wing characteristics showed that the rates of change of the lift and drag coefficients with angle of attack were strongly affected by the aspect ratio [9].

Buoyancy – the weight of fluid displaced by a body resulting in an upward force on the body

Chord – the straight line connecting the leading edge of the wing to the trailing edge of the wing

Drag – force between a body and fluid that arises from relative motion and is parallel to the motion

Glide Ratio – the forward horizontal distance traversed divided by the vertical distance descended over a time interval

Laminar Flow – fluid moveing in definite and observable paths or streamlines

Lift Coefficient - force between a body and fluid that arises from relative motion and is perpendicular to the motion

Turbulent Flow – irregular motion of fluid during a brief time interval with no observable pattern

Wing Angle – the angle of elevation of the wing with respect to the body

Wing Camber – the convex shape of the curve of an airfoil or wing from the leading edge to the trailing edge

Wing Span – the maximum distance laterally from tip to tip of the wing section

4.3 List of Figures

4.4 List of Tables

V Overview

5.1 Introduction

The objective of this research is to understand different variables that can be altered on a miniature underwater glider in order to optimize its glide ratio. Underwater gliders discussed in this paper illustrate the design and construction of miniature vehicles that can travel underwater without active propulsion. The vehicles are designed to achieve maximum glide ratio to optimize an energy efficient "gliding" configuration. Underwater gliding refers to motion in which the force of gravity provides propulsion. Steering is maintained by controlling the location of the center of gravity of the vehicle [1]. Wings on the vehicle allow steerable gliding, which subsequently offers horizontal propulsion.

In relation to existing methods of ocean environmental sampling, autonomous underwater gliders offer a variety of technical advantages: superior spatial and temporal measurement density, longer duration missions, and greater operational flexibility [1]. These advantages are improved when multiple gliders are configured to work together [1].

Henry Stommel conceived the original idea of an underwater glider in 1989 with a far-thinking article foreseeing a world ocean observing system consisting of small neutrally buoyant floats [2]. Today, more than ten years later, his dream is becoming a reality with the Slocum, Spray glider and Seaglider [3,4].

The Seaglider is a small, reusable AUV that has already operated and conducted field trials in the Pudget Sound [3]. The Spray glider is another underwater vehicle with a range of up to 6,000 km that has been developed and field tested [4]. Slocum is a small gliding AUV with an operational range of 40,000 km, which harvests its propulsive energy from the thermal gradients in the water [5]. All of these gliders are controlled by altering an internal mass in order to shift the center of gravity [5]. Another similarity between these gliders is that they are not concerned with precision gliding and minimizing their glide ratio. Although they have steep gliding angles and high velocity, these vehicles can be modified to improve the efficiencies of the horizontal distance achieved to the vertical depth dropped. The paramount importance of drag to performance makes hull and wing shape a prime consideration in the design of new underwater gliders.

In recognition of the limited source of energy in an AUV, it is important to develop a glide motion that allows for the longest search pattern. "By eliminating the need for expensive mooring equipment and research vessels for deployment and recovery, autonomous gliders are able to reduce the cost" of gathering data in accomplishing its objective [2]. The intended application for this research will be directed towards developing a new platform in mine warfare.

5.2 Background

In today's warfare, Mahan's accepted precept of control of the seas remains the cornerstone of the U.S. Navy and Marine Corps mission. Our enemies who employ mine warfare - an inexpensive, yet effective means of protecting a nation's coastal regions and littoral area compromise that objective daily. In the Persian Gulf, a $1500 World War I moored contact mine caused nearly $100 million worth of damage to the USS Samuel B. Roberts (FFG-58).

Additionally, 75 percent of damage to U.S. Navy capital ships in the last ten years came from mines, two of which were WWI technology. Hence, it is imperative that the United States Navy develop a strong mine countermeasures system to avoid the lethality of these potent weapons.

The earliest mine removal system, devised to clear anchor contact mines, consisted of two ships steaming across a minefield towing a wire rope attached between them. Mine mooring lines were cut by sharp projections on the wire or by cutting jaws. When the released mine surfaced within visual sight, it was destroyed by naval gunfire. Nearly two centuries later, technology has developed a new breed of mechanized warriors, known as Autonomous Underwater Vehicles (AUV), to combat mine warfare.

As today's Naval Explosive Ordinance Disposal Units look for innovative, technological developments in minefield clearance and related missions clearing unexploded ordinance, the further employment of autonomous unmanned vehicles (AUV) is under strong consideration. An effective method of unmanned neutralization of mines in shallow waters is not yet understood [6]. A mine countermeasures system needs to integrate a clandestine method of delivering autonomous underwater vehicles in order to map minefields, neutralize mines, and most importantly, reduce risk to human resources.

Unmanned, unattached, submersible technology offers a multitude of technical problems associated with the design and development of such a complex system. Many AUVs are oversized, which make them both inefficient for transport and cumbersome to handle. There is a positive correlation between cost and intricacy of the mission. Hence, in an effort to find a more economical and efficient means of fighting mine warfare, it is imperative that one alters the paradigm and identifies new solutions. Instead of developing systems of high complexity and cost, it is worthwhile to investigate the development of a clandestine AUV with a singular and simplistic mission. Instead of developing a vehicle that can travel over a large surface area with an immense system of sonar and acoustic sensors, it is worthwhile to explore a strategy that uses many small underwater vehicles that each measure inches in length, maintain the most fundamental mission possible, and cover a relatively small expanse of water in an energy-efficient manner. Instead of relying on a one-vehicle solution, it may be more feasible to saturate mined areas with hundreds, or maybe thousands, of small AUVs that are inexpensive and rudimentary.

Consider the possibilities of a new strategy of mine countermeasures. An alternative to an AUV weighing five hundred pounds, might weigh two pounds! In place of an AUV measuring 18 feet in length might be a device that measures 8 inches in length. Instead of one AUV searching several hundred square meters, there would be hundreds of AUVs traversing several hundred square meters at one time. As a substitute for costing several hundred thousand dollars, each would only cost a hundred dollars!

5.3 Conceptual Overview

This paper presents the results of an eight-month initiative to model autonomous underwater gliders. Underwater gliding refers to motion in which the force of gravity provides propulsion and steering is maintained by controlling the location of the center of gravity or a rudder.

The purpose of this research is to predict and validate real-time performance characteristics of underwater gliders with empirical data obtained by testing in water and by use

of experimental wind tunnel techniques. Three separate underwater gliders were constructed with variable characteristics that can be altered in order to understand the forces that enable a vehicle to glide.

Several major initiatives were required in this project - mastering glider hydrodynamic design; demonstrating the effects of wing angle on glide ratio, velocity, and lift; comparing the shape of wings and their effect upon glide ratio, and finally modeling a system to predict the behavior of these factors together. From the inception of the project, the vehicles were anticipated to be inexpensive, miniature, and unsophisticated platforms for mine detection.

In order to gain a basic understanding of the behavior of the glider models relating to velocity, glide ratio, and angle of descent, they were initially analyzed in the hydrodynamic tank at USNA. The models were subsequently mounted in the USNA Eiffel Wind Tunnel to attain authoritative values of their lift, drag, and lift-to-drag ratios in relation to angle of attack. Finally, as proof of concept, a recirculating water tank was constructed in order to test the models in a medium that combines the principles of a water tank and wind tunnel.

To date, nearly all of the underwater gliders in existence have an unsophisticated and inadequate glide ratio. Through this research, others will be able to study the stability and controllability of glide paths, derive design laws, and critically examine a methodology for testing underwater gliders – thereby developing a simplistic and optimal glide ratio.

VI Underwater Glider Models

The glider models that were created for this project were based on research of airfoil designs, aerodynamics, and drag reduction. Since certain characteristics of the vehicles were tested, it was important to design separate models that have similar, but also variable characteristics that can be measured through experimentation. Common between all models is a 5° incremental change in the wing angle relative to the main body axis. The minimum angle possible was 0°; the maximum angle was 20°.

6.1 Vehicle 1 Design Parameters

The first vehicle consisted of a PVC pipe for the body, 12-lb. foam end caps and delta shaped wings that were fabricated from plexi glass as illustrated in figures 1 and 2. In order to change the angle of the wings relative to the body, 5 separate vehicles were constructed with wings positioned at 0°, 5°, 10°, 15°, and 20° as shown in figure 5. An adhesive attached the wings to the fuselage. The cylindrical fuselage was used as a result of its low drag through the water. The vehicle and specifications are shown below.

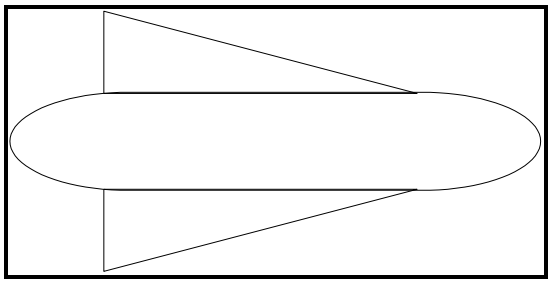

Figure 1: Top illustration of vehicle 1

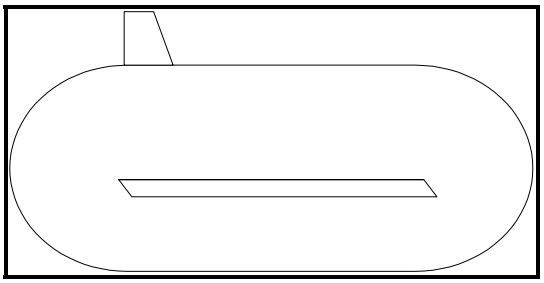

Figure 2: Side illustration of vehicle 1

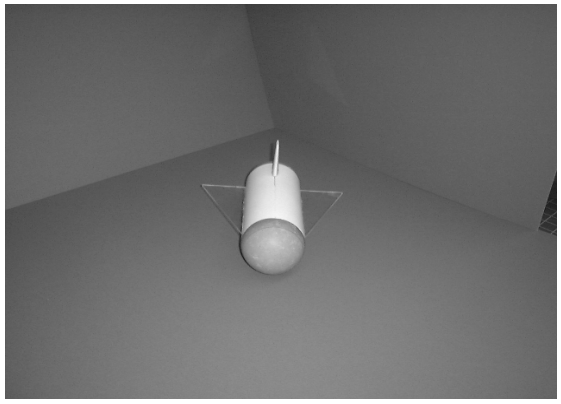

Figure 3: Front view of vehicle 1

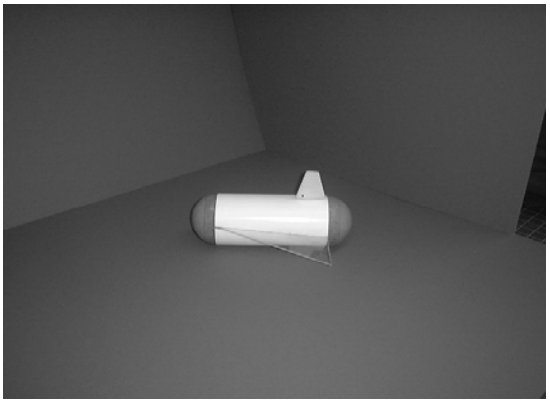

Figure 4: Side view of vehicle 1

Vehicle	Dry Weight	Length	Fuselage Diameter	Wing Chord	Wing Span	Total Volume	Total Surface Area
1	2.11 lbs	12 inches	3.5 inches	7 inches	6 inches	80.1 cubic inches	328.9 square inches

Table 1: Mathematical dimensions of vehicle 1

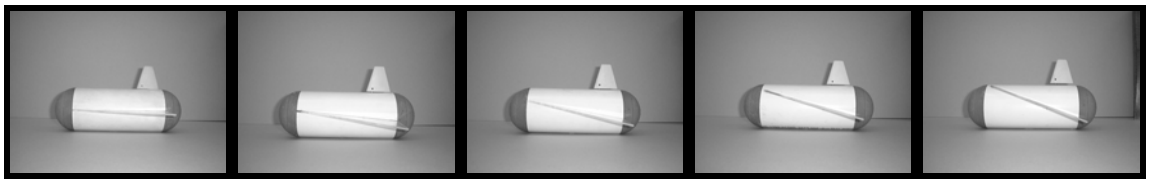

Figure 5: Vehicle 1 with wing angle 0°, 5°,10°,15°,20° (left to right)

6.2 Vehicle 2 Design Parameters

The second vehicle consisted of a PVC pipe for the body, 12-lb. foam end caps, and a cambered wing fabricated from fiberglass as shown in figures 6 and 7. The wing is mounted on the top of the vehicle and the wing angle can be altered. Wedges can be inserted underneath the wing at its attachment point to change the relative angle of the wings from 0° to 20° in increments of 5°, which can be seen in figure 11. The fuselage has a smaller diameter than vehicle 1, and the wings were changed as a result of research into thin airfoils.

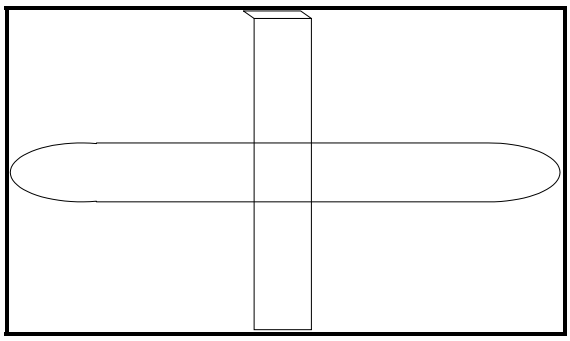

Figure 6: Top illustration of vehicle 2

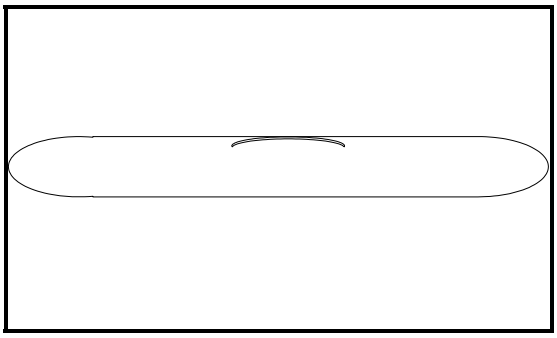

Figure 7: Side illustration of vehicle 2

In figure 7, the wing camber used to develop the shape of the wing is illustrated. The horizontal measurement is the chord of the wing and the vertical measurement is the height. The ratio of height to chord is 1:7 in the diagram. This proportion was selected based on its high lift-to-drag ratio exemplified in section 7.5. In terms of the constructed wing, the chord is 2 inches and the maximum curved height is 2/7 of an inch.

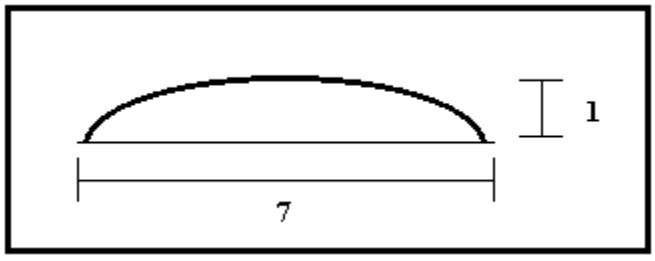

Figure 8: Wing camber of vehicle 2

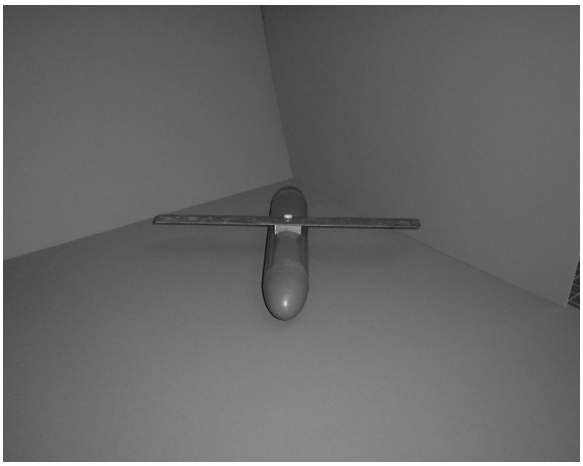

Figure 9: Front view of vehicle 2

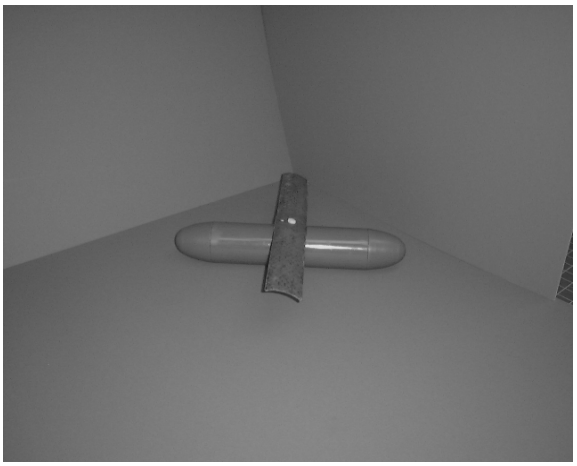

Figure 10: Side view of vehicle 2

Vehicle	Dry Weight	Length	Fuselage Diameter	Wing Chord	Wing Span	Total Volume	Total Surface Area
2	2.43 lbs	16 inches	2.5 inches	2 inches	15 inches	56.4 cubic inches	206.12 square inches

Table 2: Mathematical dimensions of vehicle 2

Figure 11: Vehicle 2 with wing angle 0°, 5°,10°,15°,20° (left to right)

6.3 Vehicle 3 Design Parameters

The third vehicle offers a combination of characteristics from the first and second vehicle. Although the fuselage dimensions are consistent with that of the first vehicle, the cambered wing is the same as the second vehicle, displayed in figure 8. Similarly, wedges can be inserted underneath the wing with a screw in order to change the relative angle of the wings from 0° to 20° in increments of 5°, as seen in figure 16. This vehicle offers a method to compare the first and second vehicle.

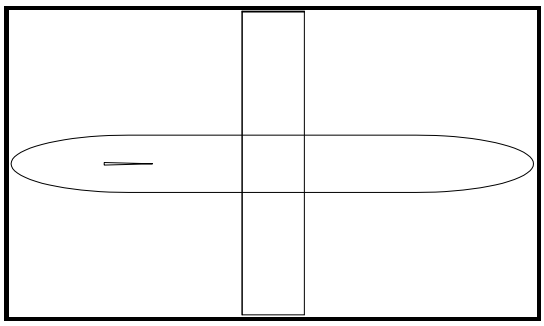

Figure 12: Top view of vehicle 3

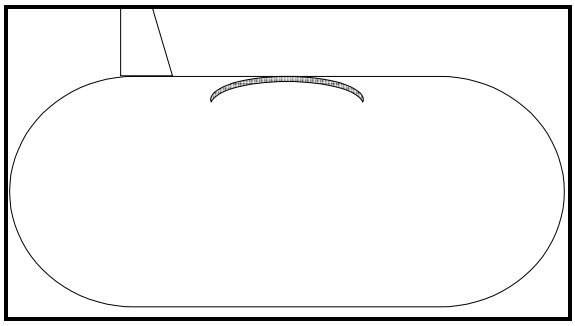

Figure 13: Side view of vehicle 3

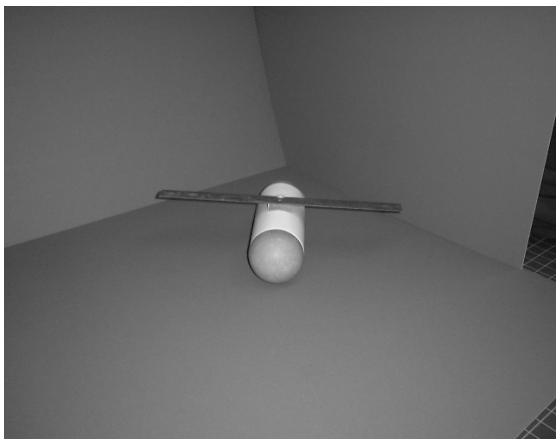

Figure 14: Front view of vehicle 3

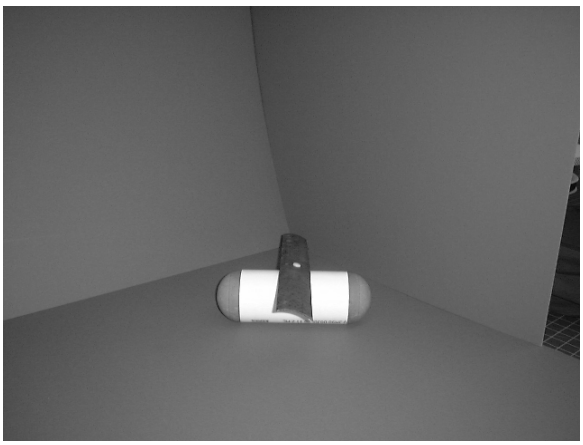

Figure 15: Side view of vehicle 3

Vehicle	Dry Weight	Length	Fuselage Diameter	Wing Chord	Wing Span	Total Volume	Total Surface Area
3	2.14 lbs	12 inches	3.5 inches	2 inches	15 inches	79.4 cubic inches	337.9 square inches

Table 3: Mathematical dimensions of vehicle 3

Figure 16: Vehicle 3 with wing angle 0°, 5°,10°,15°,20° (left to right)

VII Glider Parameters

In the design and construction of the underwater glider models, this researcher relied upon conventional theories of aerodynamics and hydrodynamics. In underwater gliding without acceleration, the weight of a vessel is counteracted by displaced mass, lifting surfaces, and drag surfaces. The parameters discussed in this chapter of the report serve as a baseline for future modification and study.

7.1 Buoyancy

Buoyancy is an upward force that is naturally exerted on an immersed body. For a condition of neutral buoyancy to exist, the weight of the underwater vehicle (W) must equal the weight of the volume of water that the submerged vessel displaces (Δ). Displacement (Δ) is the product of the volume of displacement, V, and the density, γ , of the surrounding water.

$$\Delta = V \cdot \gamma \text{ , where:} \qquad (1)$$

Δ = Displacement of water (lbs) V = Volume of water ($inches^3$)

γ = density of water (lb/ft^3)

$\Delta = F_B$ = Buoyant Force

In a situation of neutral buoyancy, the vessel will neither sink or float, but will remain at a constant operating depth until the weight of the vessel is altered. Displacement volume alone determines buoyancy. If the F_B exceeds the weight of the vessel, then the vessel will float, a condition known as positive buoyancy; if less, the vessel will sink, a condition known as negative buoyancy. Shown in figure 17, the weight vector is greater in magnitude than the F_B vector, and the AUV will sink because of negative buoyancy.

$$\text{Net Buoyancy (B)} = W - F_B \qquad (2)$$

W = Weight (lbs)

$F_B < W$	$F_B = W$	$F_B > W$
Negative Buoyancy	Neutral Buoyancy	Positive Buoyancy

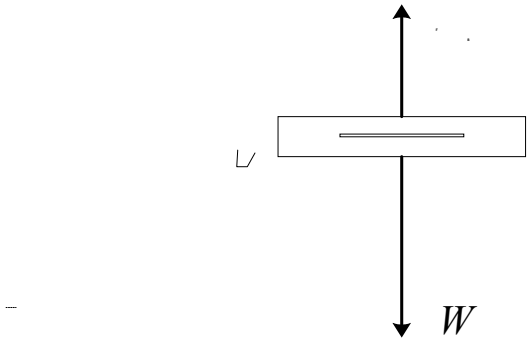

Figure 17: Gliding AUV with buoyant force F_B and weight W

For the purpose of this project, weights were added to the underwater gliders in order to induce negative buoyancy and achieve a maximum glide ratio. As shown in Figure 18 and 19, the weights were milled from brass and placed on a thin bolt in order to adjust the position of the ballast and the location of the center of gravity.

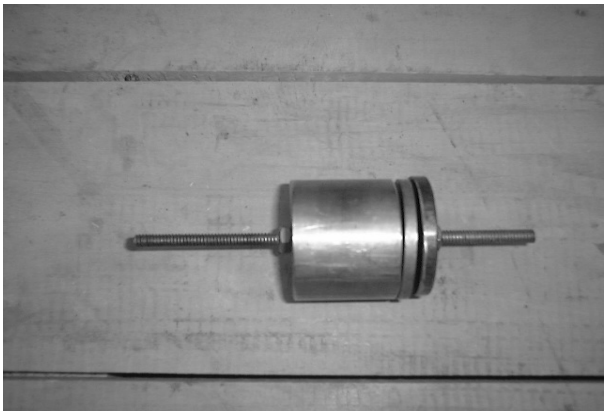

Figure 18: Ballast of vehicle 1 and 3

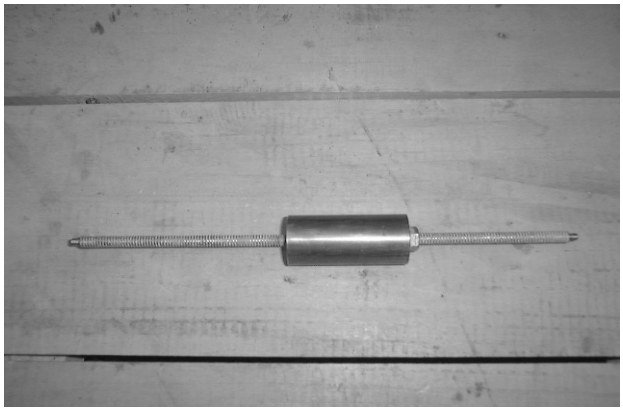

Figure 19: Ballast of vehicle 2

Each of the vehicles was carefully weighed on a scale in the U.S. Naval Academy Hydrodynamics Lab. Volumes and water displaced were also calculated. Ballast was added depending on the required buoyancy. For this investigation, the overall buoyancy of each vehicle was made negative approximately 0.7 lb. Table 4 shows the weight, volumes, displacement, and final buoyancy.

	Weight	Volume	Displacement	Ballast	Net Buoyancy	Buoyancy
	(lbs)	(cubic ft)	(lbs)	(lbs)	(lbs)	Condition
Vehicle 1	1.840	0.046	2.944	1.830	-0.726	Negative
Vehicle 2	2.140	0.032	2.048	0.610	-0.702	Negative
Vehicle 3	1.850	0.046	2.944	1.830	-0.736	Negative

Table 4: Weight, volumes, displacement, and buoyancy of underwater vehicles

7.2 Lift and Drag forces

Figure 20 depicts a gliding AUV with a lifting wing. The vehicle is gliding at an angle θ with respect to the surface (inertial coordinate system). The wing produces lift L and drag D. The net difference between vehicle weight and vehicle displacement is the net buoyancy, B. The vehicle glides at some forward velocity V.

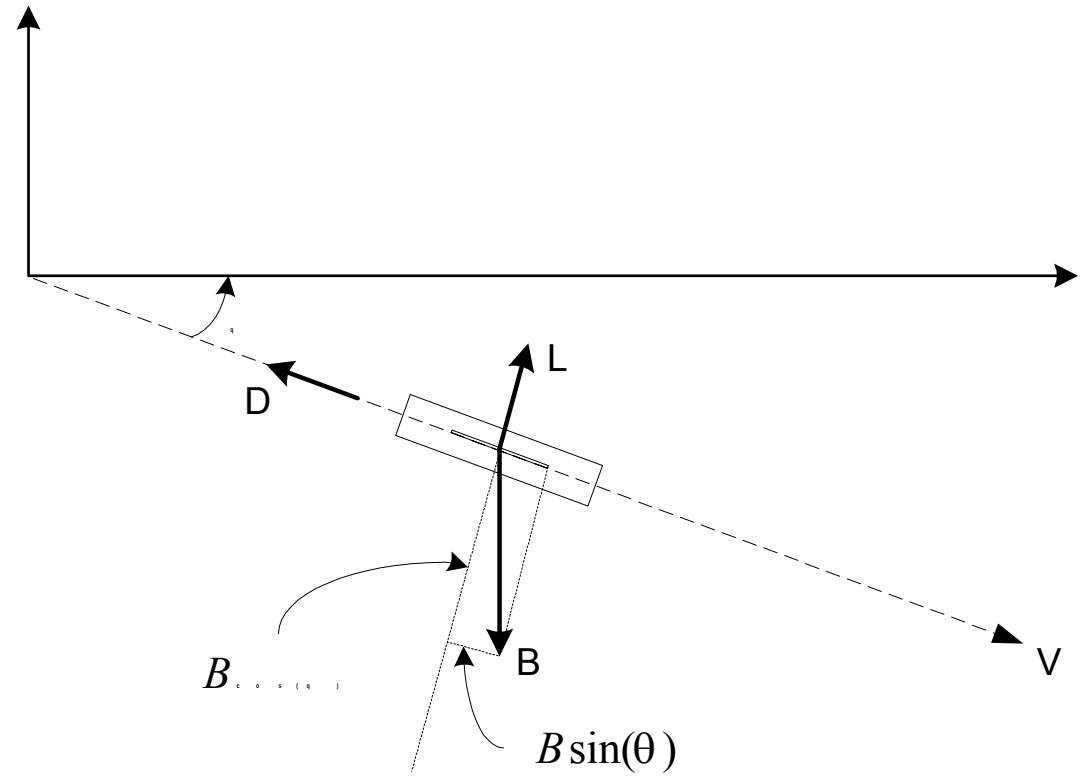

Figure 20: Gliding AUV with net buoyancy B, wing lift L, wing drag D, and forward velocity V

$$L = B\cos(\theta) \quad (3)$$

$$D = B\sin(\theta) \quad (4)$$

Note: The diagram and equations above depict unaccelerated gliding

If the vehicle is descending at a constant velocity, then the sum of forces must be conserved. The projection of buoyancy B onto lift vector L ($B\cos(\theta)$) must equal the lift provided by lifting surfaces (wing and body), and the projection of buoyancy B onto drag vector D ($B\sin(\theta)$) must provide a propelling force equal to drag D.

7.3 Glide Ratio

For the purpose of this investigation, glide ratio is defined as the horizontal distance-to-vertical distance traveled by an underwater vehicle in the medium of water. A characteristic of a glider's performance is its glide ratio, which relates to the lift-to-drag of a vehicle. When the glider is placed in water, gravity and negative buoyancy pull the vehicle under the surface. The vehicle moves a certain number of feet forward for a certain number of feet downward. The glide ratio is therefore a comparison of the distance traveled forward in water to the loss of altitude in that forward distance as shown in section 8.1. It should also be noted that the angle of the glide ratio, as referenced in this report, refers above to θ in Figure 20.

7.4 Wing Angle

As with any aircraft in the air, the wing angle relative to the airflow is important in maintaining altitude. A glider acquires its lift and drag from forward speed, wing shape, and the angle at which the wings are placed during flight. Wing angles or wing elevation, in this report, refer to the wing angle referenced to the body. If wing angle is too large, the wing will stall as illustrated at the apex of the L/D curve in Figure 21 [7]. The other curves display the relationships between wing angle versus lift and drag.

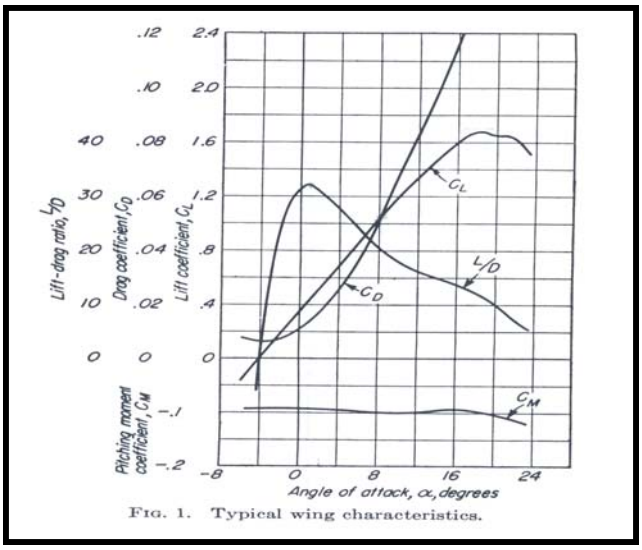

Figure 21: Wing angle vs. lift, drag, and L/D

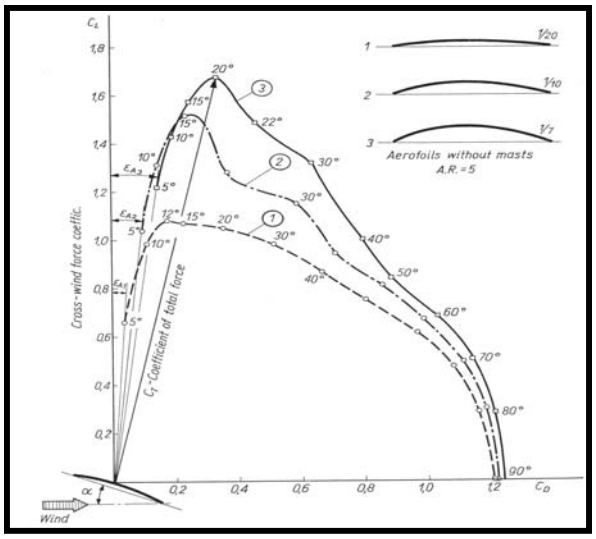

Figure 22: Wing camber relationship between lift and drag

7.5 Wing Camber

The lift and drag of hydrodynamic forces considerably depend on the shape of a wing and its camber. Camber is the curvature under the wing as shown in figure 8 of section 6.2. In Figure 22, three airfoils having cambers of 1/7, 1/10, and 1/20 respectively and a common aspect ratio of 5 are given [8]. Angle of attack is the variable that is altered in order to determine lift and drag coefficients. The greater the wing's camber, or curvature, the better the wing will perform at slow air speeds.

VIII Underwater Performance Analysis

In the initial phase of testing, three underwater gliders (described in section 6) were analyzed to determine their internal volume, weight, and buoyancy force. These values then determined the required ballast to maintain stability and negative buoyancy. As demonstrated in section 7.1, internal weights were added to each glider in order to make the vehicle negatively buoyant. Through calculations and empirical testing, the ballasting was placed at the approximate center of buoyancy.

8.1 Underwater Test

Test trials for each vehicle were conducted in a 12 ft by 24 ft hydrodynamic tank with a depth of 3 ft as shown in figures 23 and 24. The temperature of the fresh water was 69° Fahrenheit and there were no disturbances (i.e. waves, ripples) in the water. Therefore, realistic nonlinear effects that are present in the ocean did not affect the empirical observations of the vehicle. A tape measure was extended from end to end in the tank in order to measure the horizontal distance traversed by the gliders. Each glider was placed at the beginning of the tank and then slowly released from a level plane with a gentle push to initiate forward momentum. The glide path of the vehicle was then observed carefully in order to assure that the vehicle followed a straight and level descent. Each vehicle was tested as many times needed in order to obtain ten satisfactory trial runs. In order to accurately record data, there were conditions placed on each trial to determine whether it should be considered for analysis. Initially, only test runs in which the vehicle followed straight paths were recorded. Secondly, if the vehicle stalled and simply sank to the bottom as a result of its wing angle or ballasting, then the clock was stopped and the maximum horizontal distance was recorded. Finally, if the ballast needed repeated adjustment, then the test period was ended and a new set of tests were conducted. Each respective vehicle was tested with wing angles of 0°, 5°, 10°, 15°, 20°. In actuality, there were more than 500 trials conducted; however, only 150 of those tests met the experimental requirements and were recorded.

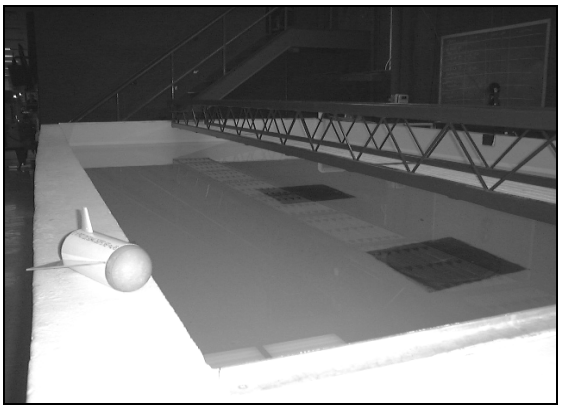

Figure 23: Left side of hydro tank

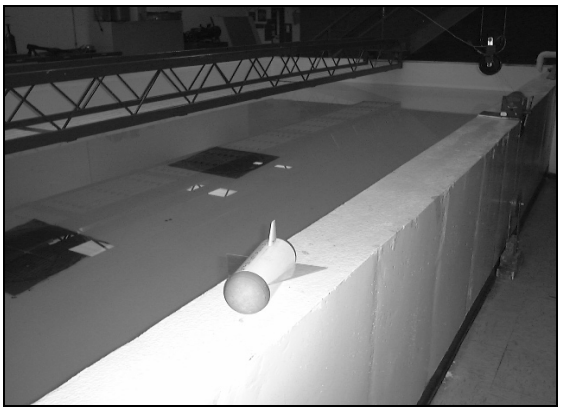

Figure 24: Right side of hydro tank

Illustrated below is a visual representation of experiment 1, in which vehicles were gently placed on the surface of the water at one end of the tank. After its release, each vehicle was then allowed to glide down its flight path by force of gravity, alone.

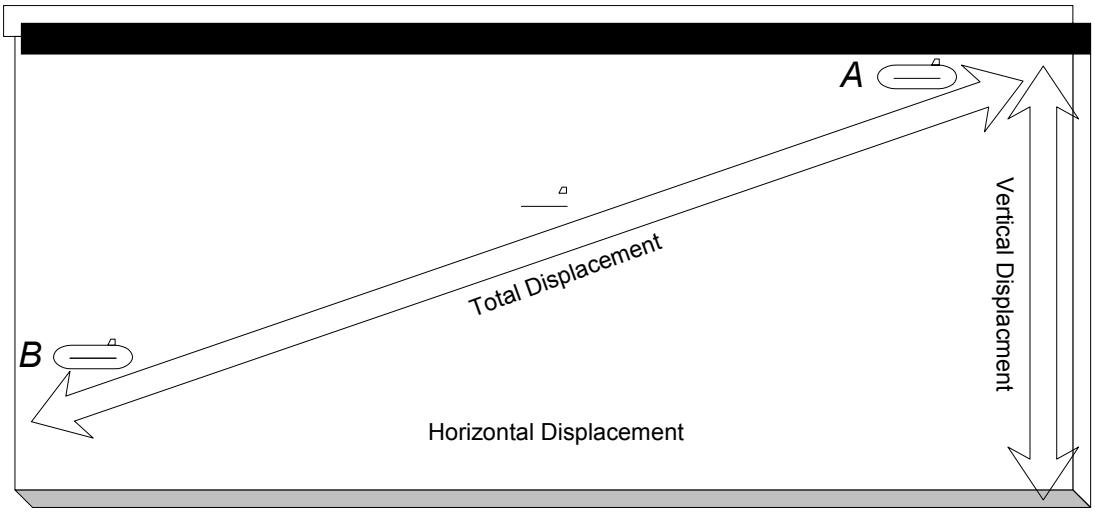

Figure 25: Underwater testing in hydro tank

Upon obtaining the horizontal and vertical displacement, which was held constant (the depth of the tank), the total displacement of each glider was calculated by the Pythagorean theorem:

$$\text{Total Displacement} = \sqrt{Horizontal^2 + Vertical^2} \tag{5}$$

After each glider was submerged in water at the surface, it was released and a stopwatch was started as illustrated in figure 25 at point A. The stopwatch recorded the time required for the glider to reach the bottom of the tank at point B. The velocity was then calculated from the time taken between points A and B.

$$\text{Velocity} = {}^{Total(Displacmenet)}\!\!\diagup\!\!_{Time} \tag{6}$$

The glide ratio represents the horizontal distance traversed per 1 foot of vertical drop. The angle of the glide ratio, θ, denotes the angle of the glide path below the surface of the water as shown in figure 20 (section 7.2).

$$\text{Glide Ratio} = ({}^{Vertical}\!\!\diagup\!\!_{Horizontal}) \tag{7}$$

$$\text{Angle of Glide Ratio} = \tan^{-1}({}^{Vertical}\!\!\diagup\!\!_{Horizontal}) \tag{8}$$

In the analysis of results, it should be noted that the scope of this project is limited to the study of the underwater behavior in terms of velocity, glide ratio, and angle of descent. The data displayed in the tables, graphs, and appendices can also provide substantive information for additional analysis.

8.2 Vehicle 1 Underwater Results

The results of the underwater tests are located in appendix 1. Averages of the underwater testing results of vehicle 1 are based upon 50 test trials and displayed below in table 5. Each row provides data by wing angle, ranging from 0° to 20°, in reference to the body.

Vehicle	Wing Angle	Horizontal Displacement	Total Displacement	Time of Descent	Velocity	Glide Ratio	Angle of Glide Ratio
	(degrees)	(inches)	(inches)	(seconds)	(ft/s)		(degrees)
1	0	89.93	96.96	8.08	1.03	2.50	24.76
1	5	85.22	92.58	5.84	1.33	2.37	26.18
1	10	85.40	92.85	8.16	0.96	2.37	26.82
1	15	77.20	85.28	7.85	0.93	2.14	29.51
1	20	67.30	76.33	6.87	0.93	1.87	34.00

Table 5: Average values derived from data in appendix 1

Table 6 displays the standard deviations for the average values in table 5. The purpose of displaying this information is to ensure confidence in the underwater testing.

Vehicle	Wing Angle	Horizontal Displacement	Total Displacement	Time of Descent	Velocity	Glide Ratio	Angle of Glide Ratio
	(degrees)	(inches)	(inches)	(seconds)	(ft/s)		(degrees)
1	0	12.26	11.41	1.63	0.16	0.34	3.63
1	5	9.13	8.33	0.71	0.09	0.25	3.73
1	10	14.74	13.46	1.74	0.13	0.41	6.16
1	15	10.35	9.39	1.76	0.10	0.29	4.51
1	20	2.11	1.86	0.88	0.11	0.06	1.31

Table 6 - Standard deviations derived from data in appendix 1

Based upon the results reported in appendix 1, figure 26 shows the 0° wing angle has the highest average glide ratio of 2.50. A 5° wing angle achieved the highest average velocity at 1.33 ft/s. A 20° wing angle obtained the lowest glide ratio at 1.87 and lowest average velocity at .93 ft/s.

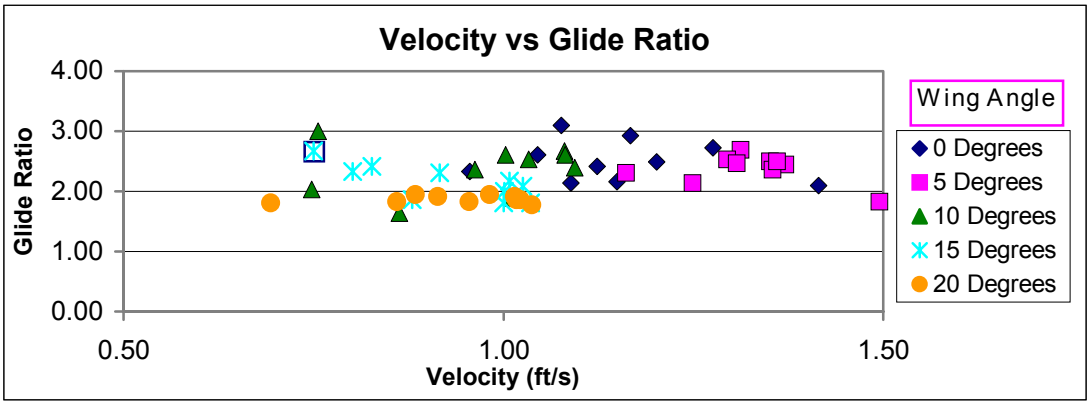

Figure 26: Velocity vs. glide ratio for vehicle 1

The graph in figure 27 confirms the data in table 1. It shows that the lowest average angle of glide ratio was 24.76° and achieved by the 0° wing angle. With the exception of the 5° wing angle, as the velocity of the vehicles decreased, a steeper angle of descent resulted. The steep angles achieved with the wings at 15° and 20° provided excessive drag and not enough lift, resulting in stalls and uncontrollable glide paths.

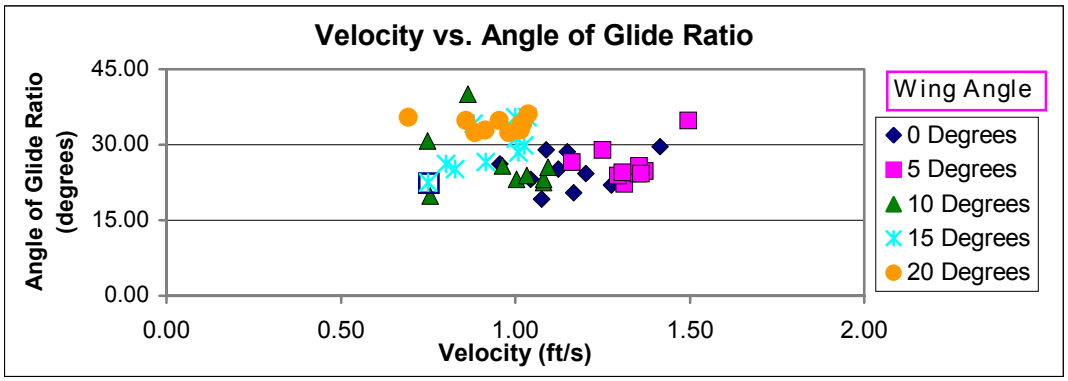

Figure 27: Velocity vs. angle of glide ratio for vehicle 1

8.3 Vehicle 2 Underwater Results

The results of the 50 underwater test trials for vehicle 2 are located in appendix 2. The averages of the vehicle's results are exhibited below in table 7. Each row provides data for a single wing angle, ranging from 0° to 20°.

Vehicle	Wing Angle	Horizontal Displacement	Total Displacement	Time of Descent	Velocity	Glide Ratio	Angle of Glide Ratio
	(degrees)	(inches)	(inches)	(seconds)	(ft/s)		(degrees)
2	0	83.80	98.22	6.34	1.30	1.64	40.83
2	5	128.90	138.91	10.95	1.08	2.53	25.16
2	10	109.80	121.42	9.63	1.06	2.15	30.42
2	15	105.90	117.79	10.10	1.00	2.08	31.20
2	20	91.20	104.69	11.07	0.80	1.79	37.05

Table 7: Average values derived from data in appendix 2

Below in table 8, the standard deviations for the average values in table 7 are shown. The rationale for showing this information is to verify the confidence in the underwater testing.

Vehicle	Wing Angle	Horizontal Displacement	Total Displacement	Time of Descent	Velocity	Glide Ratio	Angle of Glide Ratio
	(degrees)	(inches)	(inches)	(seconds)	(ft/s)		(degrees)
2	0	9.87	8.47	0.70	0.13	0.19	6.05
2	5	23.58	21.64	2.20	0.17	0.46	6.49
2	10	23.67	21.54	1.73	0.09	0.46	7.30
2	15	18.43	16.59	2.37	0.16	0.36	6.50
2	20	15.16	13.54	1.58	0.13	0.30	6.18

Table 8: Standard deviations derived from data in appendix 2

The graph of figure 28 shows a 5° wing angle on vehicle 2 has the highest average glide ratio of 2.53. A 0° wing angle achieved the highest average velocity at 1.30 ft/s. The 0° wing angle also obtained the lowest glide ratio at 1.64, while a 20° wing angle obtained the lowest average velocity at .80 ft/s.

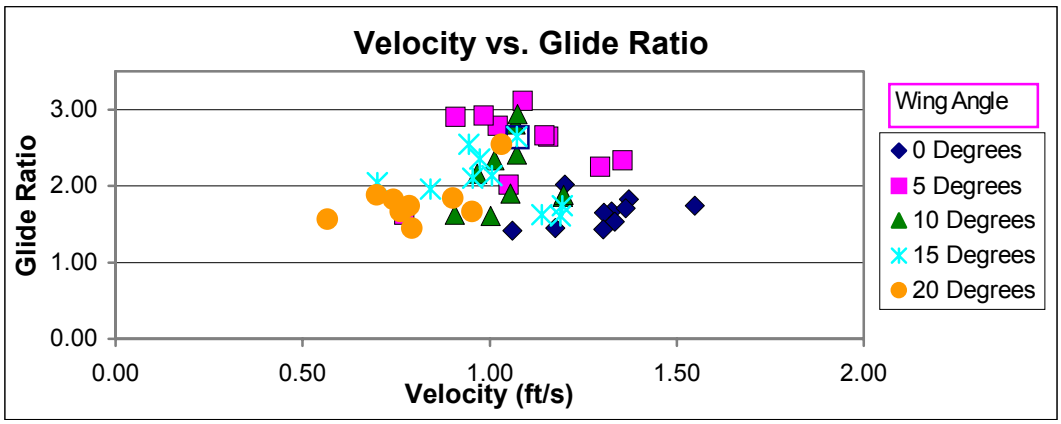

Figure 28: Velocity vs. glide ratio for vehicle 2

The graph in figure 29 confirms the data in table 7. It shows that the lowest average angle of glide ratio was 25.16° and achieved by a 5° wing angle. With the exception of the 0° wing angle, as the velocity of the vehicles decreased, a steeper angle of descent resulted.

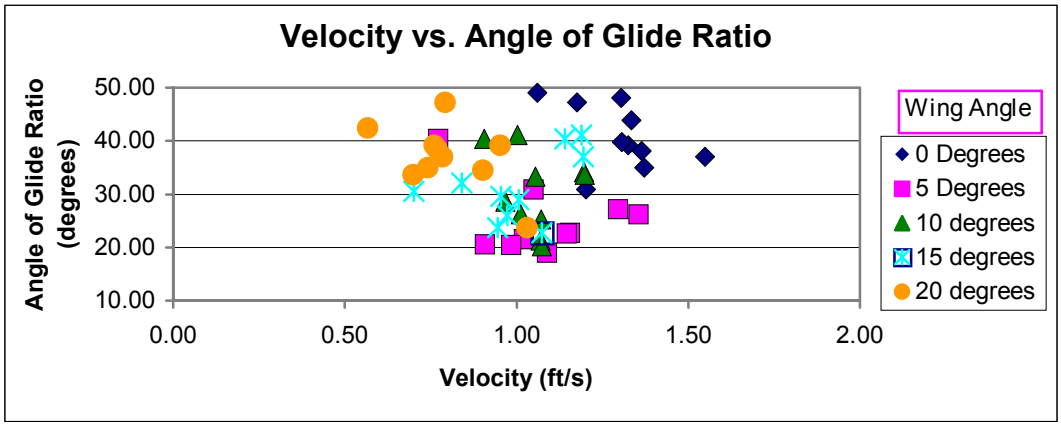

Figure 29: Velocity vs. angle of glide ratio for vehicle 2

8.4 Vehicle 3 Underwater Results

Based upon the 50 test trials for vehicle 3 found in appendix 3, the average values of underwater testing on vehicle 3 are displayed in table 9. Each row provides data for wing angles that range from 0° to 20° referenced to the body

Vehicle	Wing Angle	Horizontal Displacement	Total Displacement	Time of Descent	Velocity	Glide Ratio	Angle of Glide Ratio
	(degrees)	(inches)	(inches)	(seconds)	(ft/s)		(degrees)
3	0	80.05	87.83	8.93	0.85	2.22	28.04
3	5	64.10	73.66	7.01	0.88	1.78	37.28
3	10	60.40	70.38	6.03	0.98	1.68	39.53
3	15	52.20	63.48	5.83	0.92	1.45	48.25
3	20	37.70	52.16	5.34	0.82	1.05	82.64

Table 9: Average values derived from data in appendix 3

Table 10 displays the standard deviations for the average values in Table 9. From this data, the confidence of the wing at 20° is questionable with a standard deviation of angle of descent being 11.55.

Vehicle	Wing Angle	Horizontal Displacement	Total Displacement	Time of Descent	Velocity	Glide Ratio	Angle of Glide Ratio
	(degrees)	(inches)	(inches)	(seconds)	(ft/s)		(degrees)
3	0	8.27	7.53	1.97	0.17	0.23	3.42
3	5	10.49	9.32	0.43	0.10	0.29	6.32
3	10	5.93	5.06	0.44	0.09	0.16	5.35
3	15	5.67	4.74	0.54	0.12	0.16	6.66
3	20	2.63	1.91	0.44	0.06	0.07	11.55

Table 10: Standard deviations derived from data in appendix 3

The graph of figure 30 shows the 0° wing angle has the highest average glide ratio of 2.22. A 10° wing angle achieved the highest average velocity at 0.98 ft/s. The 20° wing angle obtained the lowest glide ratio at 0.82 and lowest average velocity at 1.05 ft/s.

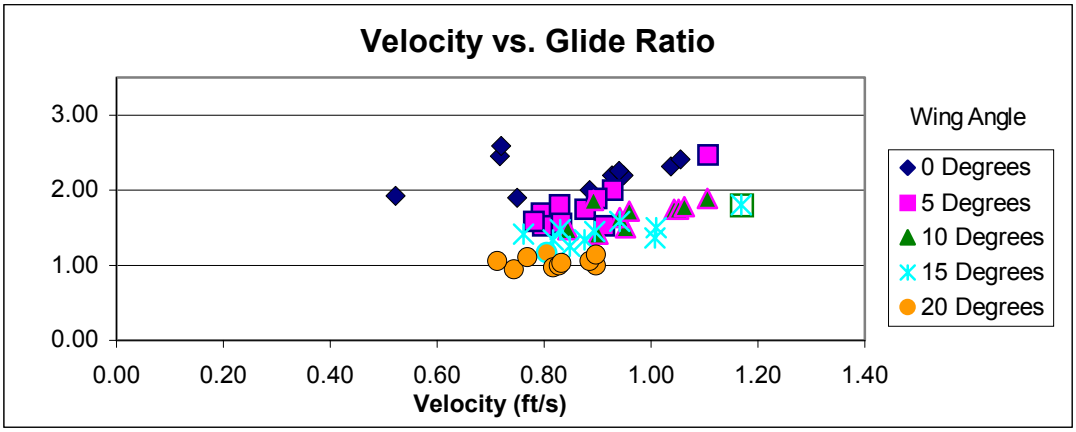

Figure 30: Velocity vs. glide ratio for vehicle 3

The graph in Figure 31 confirms the data in Table 9. It shows that the lowest average angle of glide ratio was 28.04° and achieved by a 0° wing angle. Unlike vehicles 1 and 2, there is a parabolic relationship between velocity and angle of glide ratio. The highest average velocity occurs with a 10° wing angle with an average glide ratio of 39.53°. The steep angle of descent achieved with the wing at 20° exemplifies an immediate tendency to stall with resulting short glide ratio and low velocity for the glider.

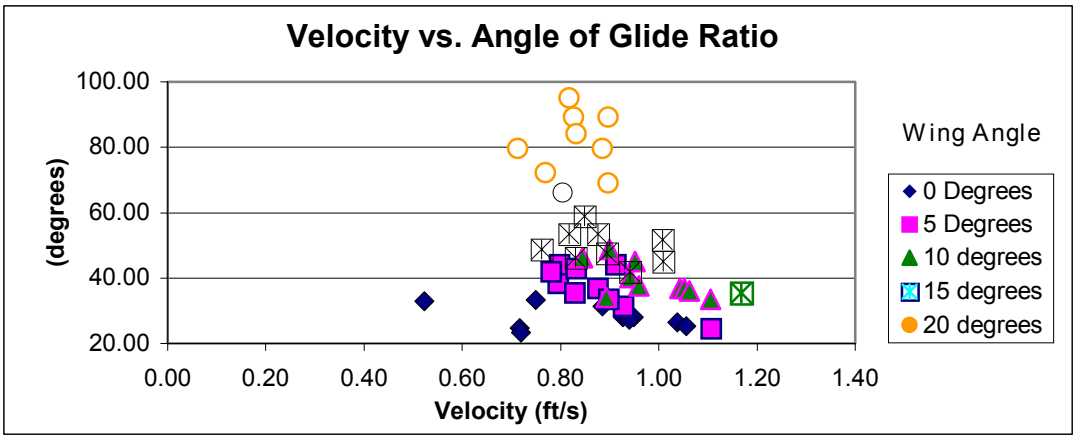

Figure 31: Velocity vs. angle of glide ratio for vehicle 3

8.5 Comparing Vehicles from Hydro Tank Results

In order to analyze the influence of wing shape and body shape on gliding behavior, it was useful to demonstrate the relationship between velocity and glide ratio for each vehicle on the same graph. As shown in figures 32-36, the delta wing on vehicle 1 achieved a higher average glide ratio and velocity than the cambered wing on vehicle 3, leading to the conclusion that the delta wing actually achieved a better lift-to-drag ratio. In maintaining the same wings and altering the body shape and size, vehicle 2 proved to be more effective than vehicle 3. With a longer, more slender fuselage, vehicle 2 achieved higher velocities underwater than vehicle 3. Likewise, it also recorded lower angles of glide ratio in every graph except figure 33. The smaller body evidently obtained a lower drag and higher lift from the cambered wing.

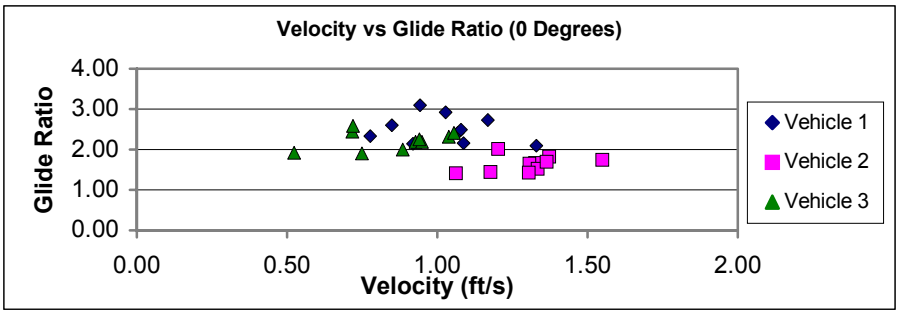

Figure 32: Velocity vs. glide ratio for 0° wing angle

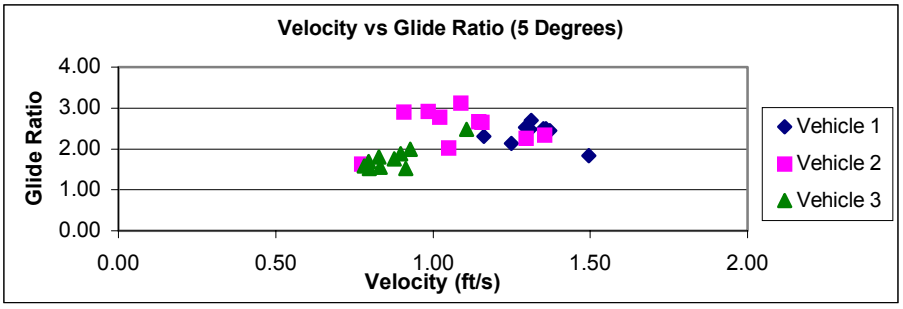

Figure 33: Velocity vs. glide ratio for 5° wing angle

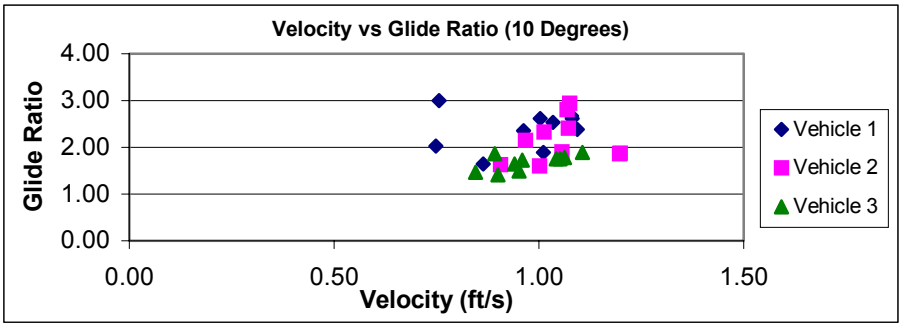

Figure 34: Velocity vs. glide ratio for 10° wing angle

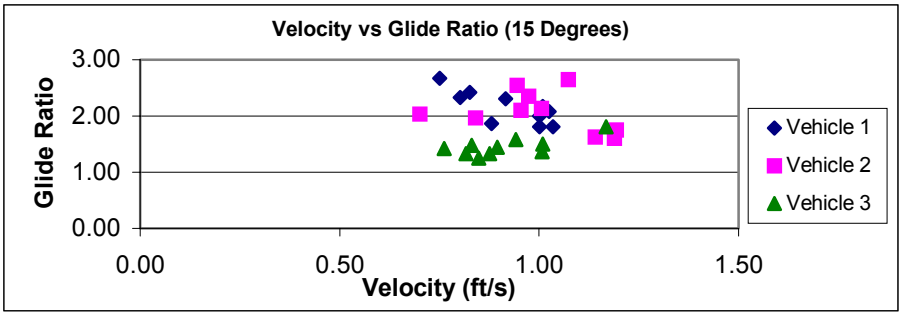

Figure 35: Velocity vs. glide ratio for 15° wing angle

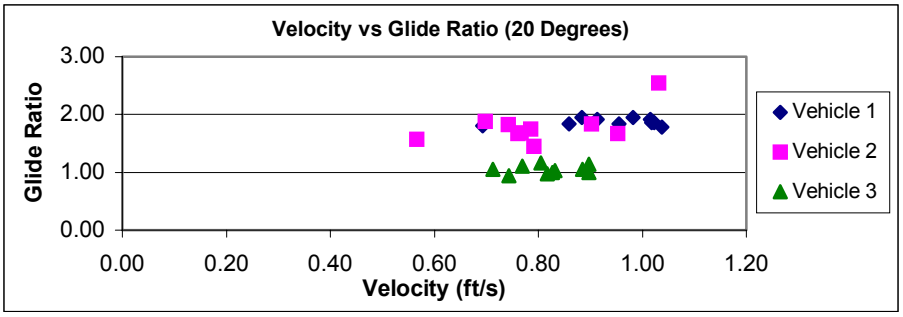

Figure 36: Velocity vs. glide ratio for 20° wing angle

In comparing the graphs of the relationship between velocity and angle of descent, it is possible to make conclusions about the effectiveness of a model's underwater behavior. Figures 37-41 show that vehicle 1 has a smaller angle of descent and higher velocity than vehicle 3, proving that it has a higher glide ratio and more efficient glide path with its delta wings. In observing the differences between vehicle 2 and 3, figures 37-41 demonstrate a higher velocity for vehicle 2 resulting from its longer, thinner hull shape. However, in terms of angle of descent, figures 38-41 exemplify a higher angle of descent for vehicle 3, which indicates the tendency to stall with a shorter, thicker hull shape.

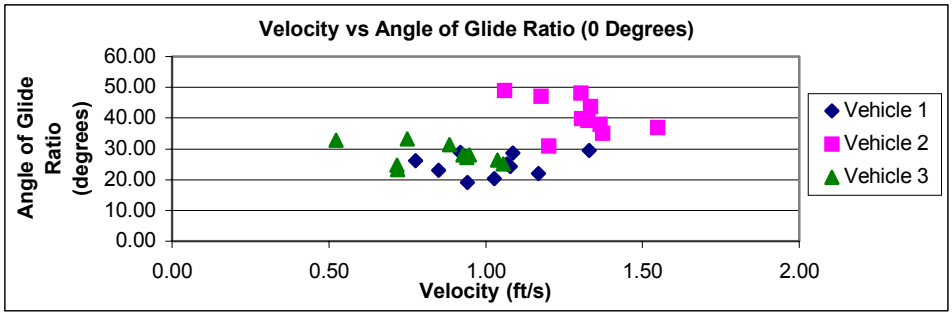

Figure 37: Velocity vs. angle of glide ratio for 0° wing angle

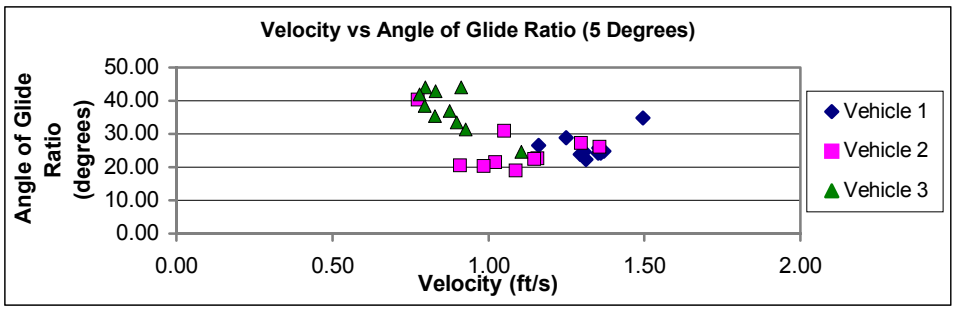

Figure 38: Velocity vs. angle of glide ratio for 5° wing angle

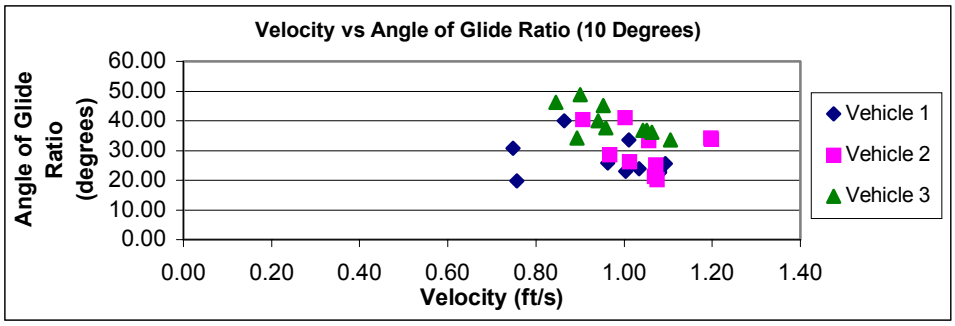

Figure 39: Velocity vs. angle of glide ratio for 10° wing angle

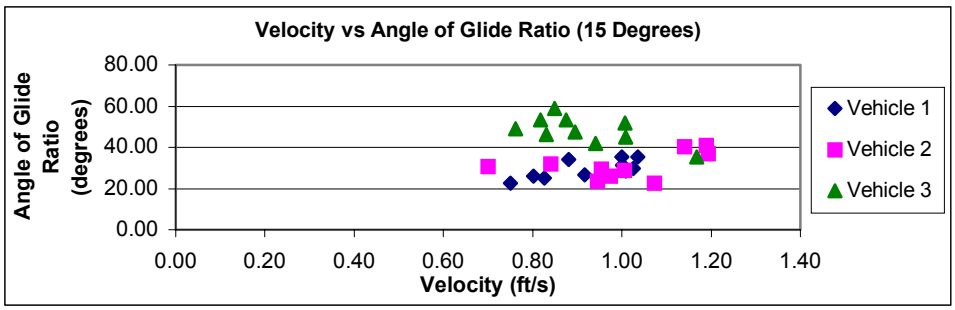

Figure 40: Velocity vs. angle of glide ratio for 15° wing angle

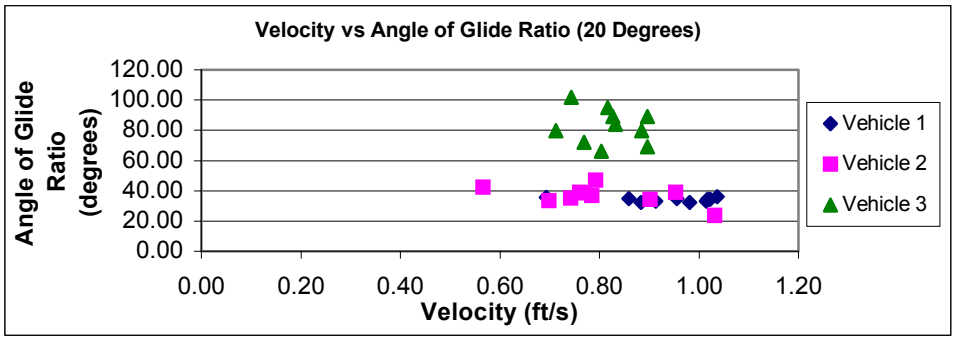

Figure 41: Velocity vs. angle of glide ratio for 20° wing angle

8.6 Lift, Drag, and Lift-to-Drag ratios of underwater gliders

In order to accurately reflect the behavior of the gliders in water, it was necessary to apply another comparison between vehicles. The following relationships were used to calculate the lift, drag, and lift-to-drag ratios:

$$L = B\cos(\theta) \quad (3)$$

$$D = B\sin(\theta) \quad (4)$$

Note: The equations above depict the net buoyancy (B), which is the difference between the upward force of buoyancy and the weight of the vehicle, in unaccelerated gliding.

By utilizing the known values for buoyancy (B) listed in table 4 of section 7.1, equations 3 and 4 were applied. Below in tables 11-13 are the results of this data reduction. The principal forces acting on a glider model are lift, L (opposes weight), and drag, D (opposes forward motion). The lift-to-drag (L/D) ratio varies with the wing angle. In comparing vehicles 1 and 3, the L/D ratio is higher with every wing angle. Similarly, vehicle 2's L/D ratios are higher than vehicle 3 for every wing angle, which reaffirms that the delta wing and longer, thinner hull shape are more effective in underwater gliding.

Vehicle	Wing Angle	Angle of Glide Ratio	Buoyancy (lbs)	Lift (lbs)	Drag (lbs)	Lift-to-Drag Ratio
	(degrees)	(degrees)				
1	0	24.76	0.73	0.66	0.30	2.17
1	5	26.18	0.73	0.65	0.32	2.03
1	10	26.82	0.73	0.65	0.33	1.98
1	15	29.51	0.73	0.63	0.36	1.77
1	20	34.00	0.73	0.60	0.41	1.48

Table 11: Underwater Results of Lift, Drag, and L/D ratio for vehicle 1

Vehicle	Wing Angle	Angle of Glide Ratio	Buoyancy (lbs)	Lift (lbs)	Drag (lbs)	Lift-to-Drag Ratio
	(degrees)	(degrees)				
2	0	40.83	0.70	0.53	0.46	1.16
2	5	25.16	0.70	0.64	0.30	2.13
2	10	30.42	0.70	0.61	0.36	1.70
2	15	31.20	0.70	0.60	0.36	1.65
2	20	37.05	0.70	0.56	0.42	1.32

Table 12: Underwater Results of Lift, Drag, and L/D ratio for vehicle 2

Vehicle	Wing Angle	Angle of Glide Ratio	Buoyancy (lbs)	Lift (lbs)	Drag (lbs)	Lift-to-Drag Ratio
	(degrees)	(degrees)				
3	0	28.04	0.73	0.64	0.34	1.88
3	5	37.28	0.73	0.58	0.44	1.31
3	10	39.53	0.73	0.56	0.46	1.21
3	15	48.25	0.73	0.49	0.54	0.89
3	20	82.64	0.73	0.09	0.72	0.13

Table 13: Underwater Results of Lift, Drag, and L/D ratio for vehicle 3

In general, the underwater analysis of the glider models was effective in showing the true behavior of the vehicles underwater. Measurements taken were based on distance and time. From the results and graphs, it can be concluded that the delta wing shape was more effective at achieving a higher velocity, lower glide angle and higher glide ratio than the cambered wing. Additionally, the thinner, longer and more streamlined hull shape was more effective at maintaining a higher glide ratio than the shorter, thicker hull. For future study, it would be worthwhile to fit the models with delta wings and a thinner, longer fuselage to improve the gliding characteristics. Additionally, if more time permits, it would also be worthwhile to develop a series of equations to model the behavior of the underwater glider, predict its angle of descent, and predetermine the flight trajectory. Prior to completing this task, it would be helpful to compare the data that has already been collected with a datum that provides accepted results of the lift and drag forces on vehicles. Thus, the question of validating the real time performance of the underwater gliders leads the investigation directly to the wind tunnel experimental analysis in the next section of this report.

IX Wind Tunnel Testing of Gliders

9.1 Reynolds Number

The relative motion and the drag of a vehicle are the same whether a body moves at uniform speed through a stagnant ocean of fluid, or whether a large body of fluid streams past the body, as in a wind tunnel. In this next phase of the investigation, the glider models were held stationary in a moving stream, rather than moving through still fluid. The two circumstances are equivalent, and the results of the experiments may be interpreted without reference to which experimental method is used. This change in the viewing position of the observer, from one in which he is attached to the body to one in which he is attached to the flow, is commonly known as "Galilean transformation" [9]. In order to compare tests between different mediums, the value of a Reynolds number offers an equation of relation. The ratio of density/viscosity offers a constant in which a glider's velocity in the water can provide a comparable value at which the wind must travel in a wind tunnel.

$$\mathrm{Re} = \rho VL / \upsilon \tag{9}$$

ρ = density $\qquad$ υ = viscosity

$\rho_{WATER} = 1.936 \ \mathrm{slugs}/\mathrm{ft}^3$ $\qquad$ $\rho_{AIR} = .002374 \ \mathrm{slugs}/\mathrm{ft}^3$

$\upsilon_{WATER} = 21*10^{-6} \ lb*s/ft^2$ $\qquad$ $\upsilon_{AIR} = .374*10^{-6} \ lb*s/ft^2$

V = Velocity of vehicle $\qquad$ L = Length of vehicle

$$\mathrm{Re}_{WATER} = R_{AIR}$$

Vehicle 1	
Indicated Airspeed (mph)	Reynolds Number
20.00	126952
25.00	158690
30.00	190428
35.00	222166
40.00	253904
45.00	285642
50.00	317380
55.00	349118
60.00	380856
65.00	412594
70.00	444332
75.00	476070
80.00	507807

Vehicle 2	
Indicated Airspeed (mph)	Reynolds Number
20.00	177733
25.00	222166
30.00	266599
35.00	311032
40.00	355465
45.00	399898
50.00	444332
55.00	488765
60.00	533198
65.00	577631
70.00	622064
75.00	666497
80.00	710930

Vehicle 3	
Indicated Airspeed (mph)	Reynolds Number
20.00	126952
25.00	158690
30.00	190428
35.00	222166
40.00	253904
45.00	285642
50.00	317380
55.00	349118
60.00	380856
65.00	412594
70.00	444332
75.00	476070
80.00	507807

Appendixes 1-3 contain Reynolds numbers corresponding to underwater test trials. Due to a limitation of the wind tunnel requiring a nominal speed of 40 mph to achieve accurate results from the strain gauge balance, the Reynolds numbers between air and water do not equate. In the underwater test trials, the speed of the vehicles relating to the wind tunnel was approximately 20 mph, which equates to a Reynolds number of 90,000. Wind tunnel tests were conducted at the nominal speed of 40 mph, which corresponds to a Reynolds number of 250,000-350,000 as shown in tables 11-13. Ultimately, the sensitivity of the wind tunnel is a limitation in the ability to precisely measure forces of underwater gliders in a wind tunnel at the necessary speeds. Nevertheless, data from the wind tunnel tests still provides valuable insight about the behavior of underwater gliders and the ability to evaluate the lift and drag forces acting on wing and body shapes.

9.2 Wind Tunnel

The purpose of this experiment was to predict and validate full-scale performance characteristics of the underwater gliders using experimental wind tunnel techniques. The U.S. Naval Academy Eiffel Wind Tunnel is an induction type wind tunnel. The airflow is generated through the tunnel by means of a large fan driven by an electric motor. The Eiffel tunnel was designed and manufactured by Aerolab Industries in 1994. I t has a testing section of 44” by 31” and can generate wind speeds ranging from 2 to 250 mph.

The models were mounted on an internal strain gauge balance as shown in figure 42, installed on a sting mounting system, and tested at various angles of attack and airspeeds. The sting system allows for altering the pitch and yaw of the model during a wind tunnel run.

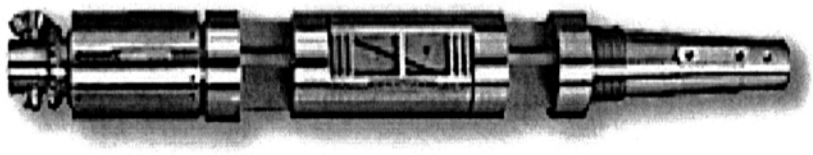

Figure 42: Typical 6-component internal strain gauge balance

9.3 Glider Lift and Drag Determination

When measuring aerodynamic forces using a sting force balance, lift (L) and drag (D) cannot be measured directly, because the sting balance can only measure normal (N) and axial (A) forces. These unknown values can be determined through trigonometric formulas using the sting angle of attack (α).

$$L = N\cos(\alpha) - A\sin(\alpha) \tag{10}$$

$$D = N\sin(\alpha) - A\cos(\alpha) \tag{11}$$

9.4 Balance Tare Corrections

It is important to note that prior to using normal and axial force data, they must be adjusted to account for the weight of the model and minor voltage offsets in the electronics. Therefore, several measurements must be taken with the sting by itself. This process is known as obtaining the balance tare and directly enables the balance to read zero loads at zero velocity. The balance tare must be measured at all intended test angles of attack because shifts in the sting will produce shifts in the balance output. In order to obtain the corrected values for the normal and axial force, the tare measurements must first be subtracted using the following equations:

$$N = N_{raw} - N_{tare} \tag{12}$$

$$A = A_{raw} - A_{tare} \tag{13}$$

9.5 Wind Tunnel Procedure

In the wind tunnel, the ambient temperature and atmospheric pressure were recorded. Then, prior to turning on the fan, the sting tare data for α, N, and A. Starting at 0° α and ending at +20° α in the values of α, N, and A were recorded in increments of +2° α to provide the tare data. In Figures 43 and 44, vehicle 1 is displayed at 0° and 20° respectively, in the wind tunnel test section.

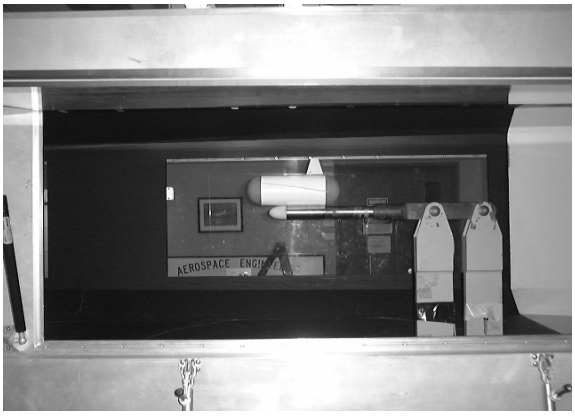

Figure 43: Vehicle at 0° in wind tunnel

Figure 44: Vehicle at 20° in wind tunnel

During this first test phase, nominal wind flow speed was set at 40 mph, which was a predetermined minimum value relating to the Reynolds number calculated in the earlier underwater gliding trials as shown in Tables 11, 12, and 13. In order to calibrate wind tunnel speeds, dynamic pressure was calculated in inches of alcohol and read through the series of

manometers, displayed in figure 45. The pressures and inches of alcohol and water were determined by the following formulas:

$$P = \frac{1}{2}\rho v \tag{14}$$

P = Pressure v = velocity ρ = density

$$P(psi) = \frac{1}{2} \times \rho(\frac{slug}{ft^3}) \times v(\frac{1mi}{hour})(\frac{5280\,ft}{1mi})^2(\frac{hour}{3600\,\sec})(\frac{ft^2}{144in^2})$$

q = inches of water in manometer

$$q(in)_{Water} = P \times (\frac{406.8(in)_{Water}}{14.70\,psi})$$

$$q(in)_{Alcohol} = q(in)_{Water} \times (\frac{502.2(in)_{Alcohol}}{406.8(in)_{Water}})$$

Velocity (mph)	Pressure (psi)	q (in. of water)	q (in. of alcohol)
20	0.0071	0.1960	0.2420
25	0.0111	0.3062	0.3781
30	0.0159	0.4410	0.5444
35	0.0217	0.6002	0.7410
40	0.0283	0.7840	0.9679
45	0.0358	0.9922	1.2250
50	0.0443	1.2250	1.5123
55	0.0535	1.4822	1.8299
60	0.0637	1.7639	2.1777
65	0.0748	2.0702	2.5558
70	0.0867	2.4009	2.9641
75	0.0996	2.7561	3.4026
80	0.1133	3.1359	3.8715

Table 14: Calculations of true airspeeds through dynamic pressure of alcohol

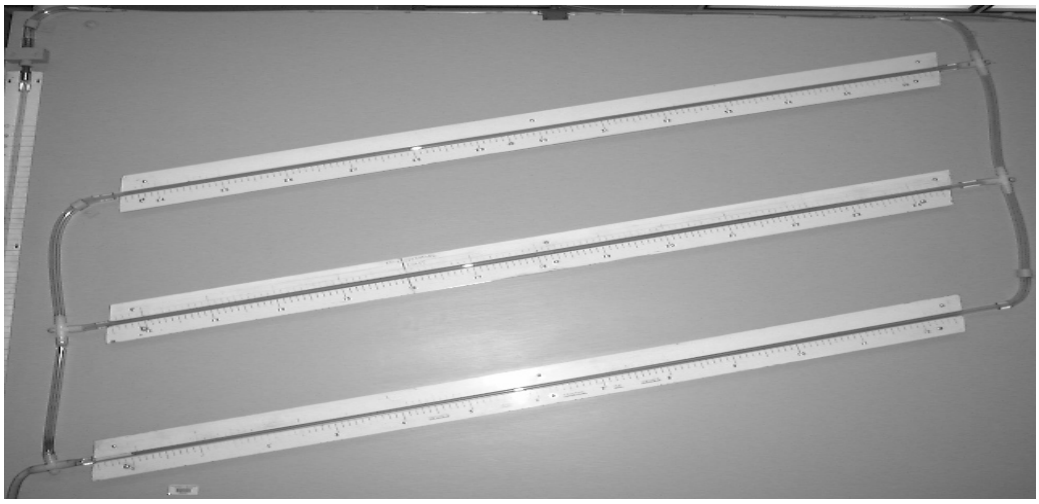

Figure 45: Manometers displaying true airspeed in the test section using dynamic pressure

Then an alpha sweep was conducted in which angle of attack was increased from 0° to +20° in increments of 2°. A computer program enabled the data to be recorded in a stepwise process that lasted 0.2 seconds. For each angle of attack, three separate measurements were taken in order to subsequently determine an average and standard deviation for each data point, as shown in appendixes 4-6. Values of α, N, and A were recorded. From these results, it was feasible to then calculate and then determine relationships between lift, drag, coefficient of lift, coefficient of drag, and lift-to-drag ratio.

Finally, a Reynolds Number sweep was conducted whereby the test section velocity was varied in increments of 5 mph from a minimum value of 20 mph to 80 mph. Values of velocity, N, and A at each point were recorded. The vehicles were mounted at an angle of attack that was consistent with the maximum lift-to-drag ratio as determined by the alpha sweep. The maximum lift-to-drag value was used for this analysis because it offered an optimal performance and definitive results. Again, the wind speeds were calibrated according to dynamic pressure and the units of inches alcohol. In terms of the data reduction for the wind tunnel testing, the following calculations were performed:

- Air density as evidenced in figure 45.
- True airspeed in the test section for each run condition using the dynamic pressure equations as illustrated in table 14.
- Reynolds numbers for each run condition and vehicle in tables 11-13.
- Corrected balance data for normal (N) and axial (A) forces at each angle of attack by subtracting the corresponding tare values from the raw data as shown in appendixes 4-6.
- Converted N and A into L and D at each α as shown in appendices 4-6.

After manipulating the data, the following relations were plotted:

- Angle of attack (α) vs. coefficient of lift (C_L)
- Coefficient of lift (C_L) vs. lift-to-drag (L/D) ratio

9.6 Vehicle 1 Wind Tunnel Results

Based on the data appearing in appendix 4, the graph in figure 46 illustrates the positive correlation between coefficient of drag and coefficient of lift of vehicle 1. In terms of lift vectors, vehicle 1 with a wing angle of 20° has a comparable coefficient of lift to vehicle 1 with a 0° wing angle and 20° angle of attack with respect to the airflow. This indicates that the majority of lift is derived from the wings. The negative slopes in the graph illustrate the angle of attack at which vehicle 1 stalls. The peak value is the optimal angle of attack to achieve the greatest lift.

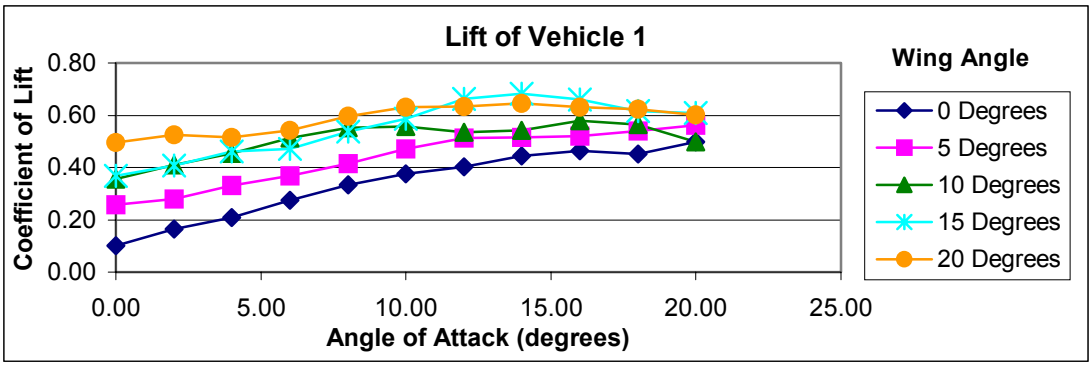

Figure 46: Angle of attack vs. coefficient of lift for vehicle 1

In figure 47, the efficiency of vehicle 1 is denoted by the relationship between the coefficient of lift and the lift-to-drag ratio. As the coefficient of lift increases, the coefficient of drag likewise increases. As shown in appendix 4, the 10° wing angle yielded the highest ratio of lift-to-drag at 3.64, which is optimal towards gliding. At higher angles, the coefficient of drag negates the higher coefficients of lift.

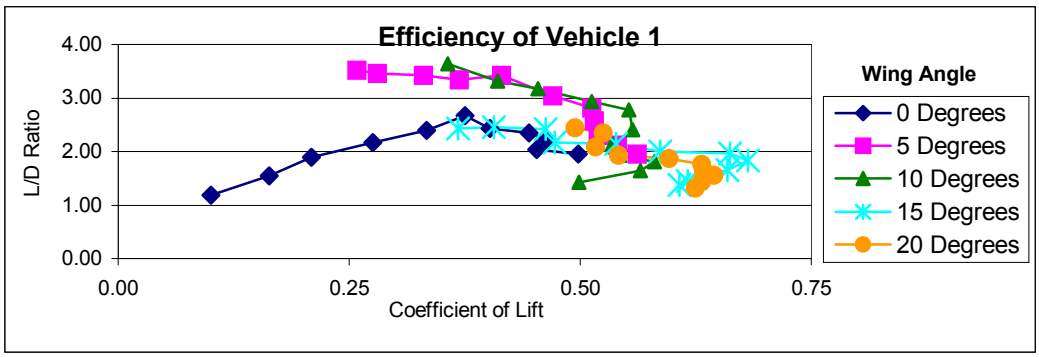

Figure 47: Coefficient of lift vs. lift-to-drag ratio for vehicle 1

9.7 Vehicle 2 Wind Tunnel Results

The graph in figure 48 shows the positive correlation between coefficient of drag and coefficient of lift of vehicle 2. The peak value is the optimal angle of attack to achieve the greatest lift. The 5° wing angle positioned at 10° angle of attack obtains a maximum lift coefficient of 1.09. In this series of trials, the 10°, 15°, and 20° wing angle positioned at 20° angle of attack achieved a consistent coefficient of lift of approximately 0.62. Therefore, it can be inferred that the cambered wing provides a limited and constant degree of lift regardless of the wing and body angles of attack being larger than 20°.

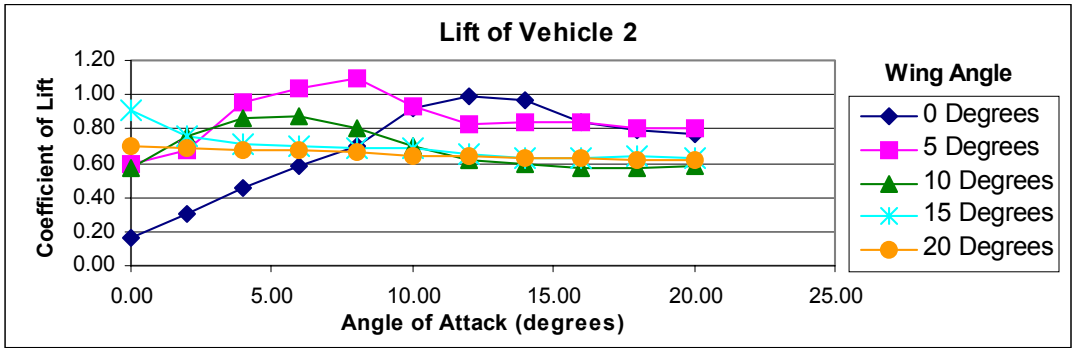

Figure 48: Angle of attack vs. coefficient of lift for vehicle 2

The efficiency of vehicle 2 is denoted by the relationship between the coefficient of lift and the lift-to-drag ratio in figure 49. As the coefficient of lift increases, the coefficient of drag decreases. Displayed in appendix 5, the 0° wing angle of attack yielded the highest ratio of lift-to-drag at 10.28, which is optimal for gliding. At higher angles of attack, the coefficient of lift actually decreases while the coefficient of drag remains steady.

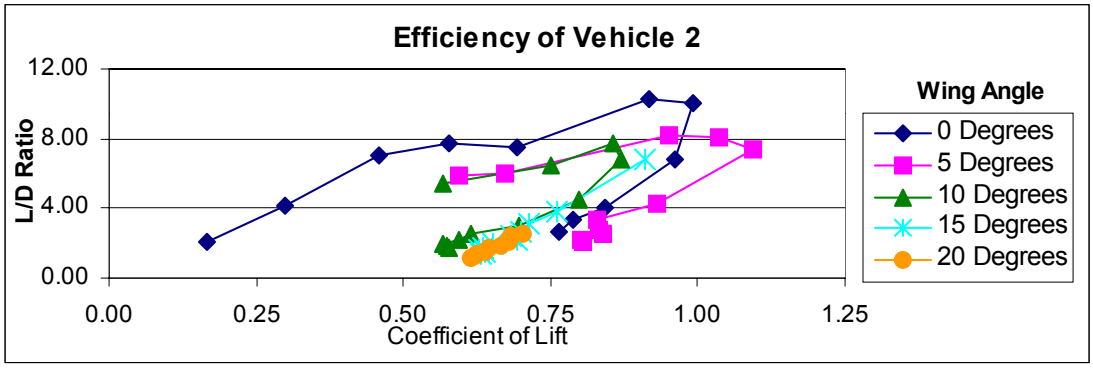

Figure 49: Coefficient of lift vs. lift-to-drag ratio for vehicle 2

9.8 Vehicle 3 Wind Tunnel Results

Figure 50 exemplifies the positive correlation between coefficient of drag and coefficient of lift of vehicle 3. The optimal angle of attack occurs at the peak values because those values achieve the maximum lift. The 0° wing angle positioned at 12° angle of attack attains a maximum lift coefficient 1.15. The 5°, 10°, and 15° wing angles positioned at 20° angle of attack obtained a regular coefficient of lift of approximately 0.75, which suggests the cambered wing provides a unvarying degree of lift regardless of the angle of the wing relative to the body.

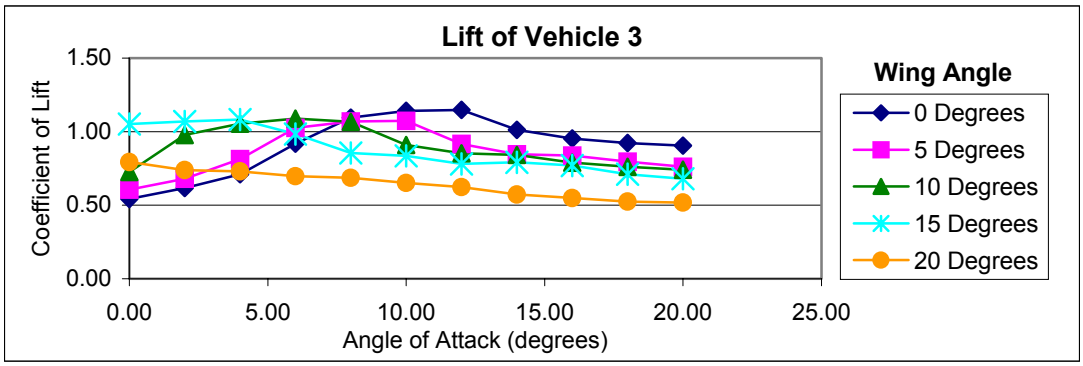

Figure 50: Angle of attack vs. coefficient of lift for vehicle 3

As seen below in figure 51, vehicle 3's efficiency is characterized by the relationship between the coefficient of lift and the lift-to-drag ratio. As the coefficient of lift increases, the coefficient of drag declines. A 15° wing angle yielded the highest ratio of lift-to-drag at 7.74, which is optimal towards gliding. At higher angles of attack, the coefficient of lift decreases while the coefficient of drag remains steady.

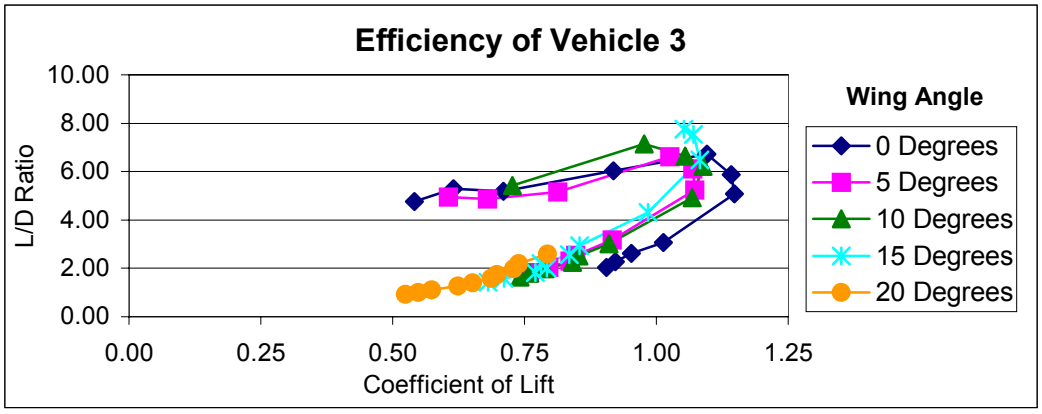

Figure 51: Coefficient of lift vs. lift-to-drag ratio for vehicle 3

9.9 Comparing Vehicles from Wind Tunnel Results

In order to comprehend the difference between the different glider models' behavior and their characteristics, it is necessary to graph the results of each model on the same diagram as shown below. Based on figures 52-54, it is clear that the cambered airfoil for vehicle 3 is significantly more effective than the delta wing on vehicle 1 in terms of achieving lift. There is a marked difference between each line at every wing angle of attack positioned between 0° and 20°. Therefore, it can be concluded that a more favorable pressure gradient occurs over the cambered airfoil than the delta wing shape at low wing angles. Figures 52-54 also show a positive slope for the coefficient of lift. Figures 55 and 56 illustrate the propensity of the wing to stall, for the coefficient of lift diminishes as the wing angle increases. Therefore, under these circumstances, the vehicle with the cambered wing at a lower wing angle achieves a higher lift while at a higher wing angle, the delta wing then achieves more lift. In comparing the shape and size of vehicle 2 and 3, it is clear that the shorter and thicker frame of vehicle 3 enables the airfoil to achieve a higher degree of lift as illustrated in figures 52-56. At each angle of attack, the data points from vehicle 3 are superior to those of vehicle 2 illustrating that there also might be less induced drag from the shorter length of vehicle 3.

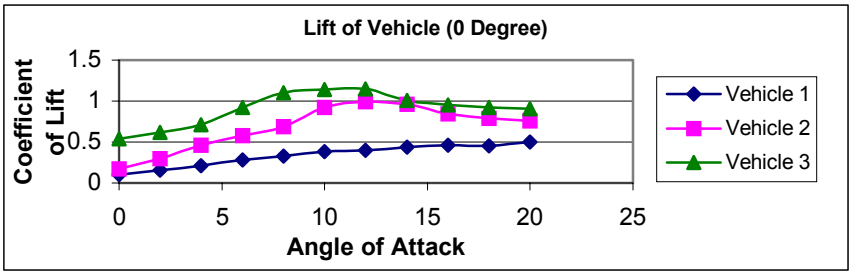

Figure 52: Angle of attack vs. coefficient of lift for 0° wing angle

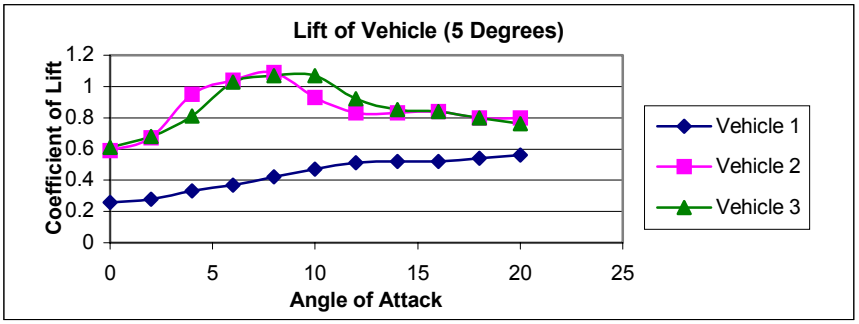

Figure 53: Angle of attack vs. coefficient of lift for 5° wing angle

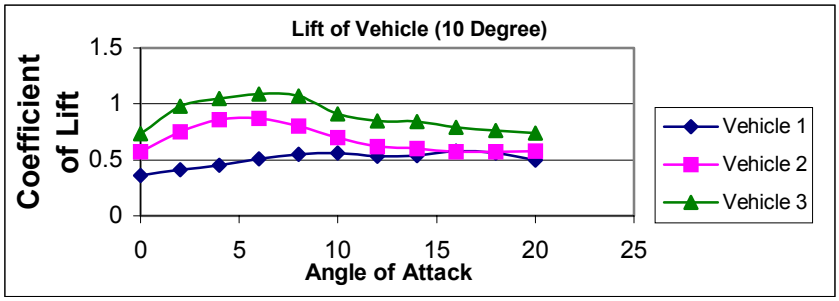

Figure 54: Angle of attack vs. coefficient of lift for 10° wing angle

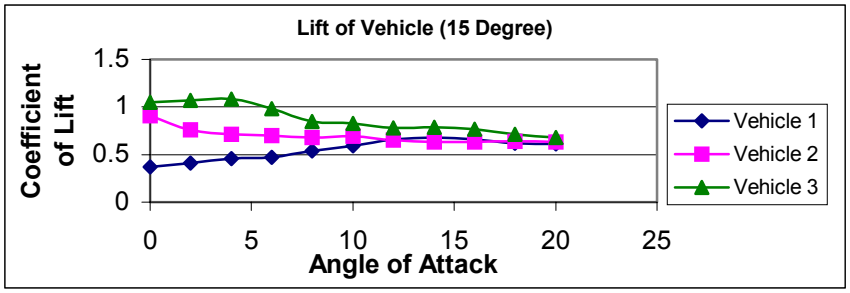

Figure 55: Angle of attack vs. coefficient of lift for 15° wing angle

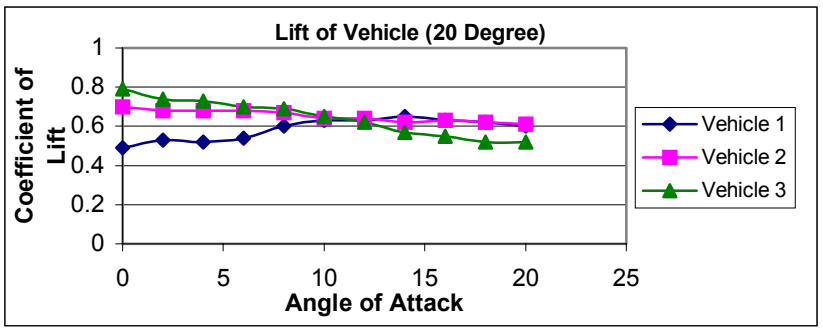

Figure 56: Angle of attack vs. coefficient of lift for 20° wing angle

In analyzing the efficiency between the cambered wing and delta wing, figures 57-61 show the positive correlation between lift and angle of attack. In each of these graphs, vehicle 3 displays a higher L/D ratio than vehicle 1. It should also be noted that the vehicles experience stalling moments, which are evidenced by the negative slope of the data points. With regard to the body shape and size, the smaller and thinner shape from vehicle 2 shows a higher lift-to-drag ratio and therefore an improved utilization of the lifting force. This conclusion can be seen in Figures 57-60, where the curves for vehicle 2 achieve a smaller coefficient of lift, but larger lift-to-drag ratio.

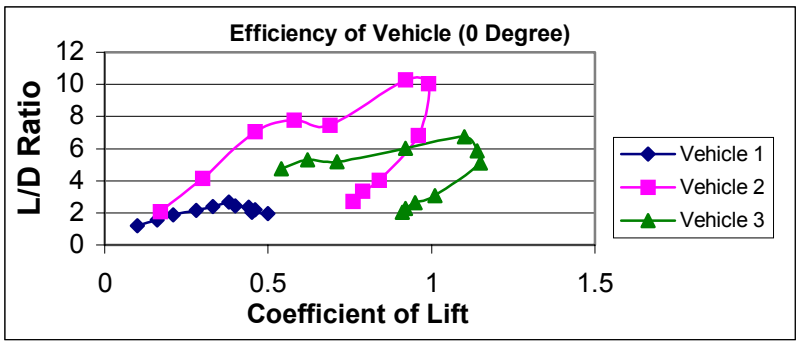

Figure 57: Coefficient of lift vs. L/D ratio for 0° wing angle

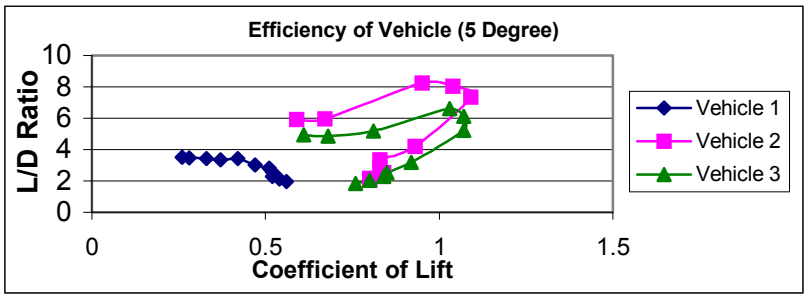

Figure 58: Coefficient of lift vs. L/D ratio for 5° wing angle

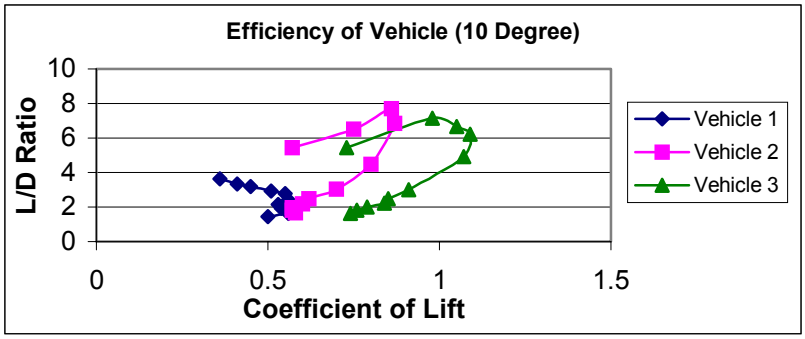

Figure 59: Coefficient of lift vs. L/D ratio for 10° wing angle

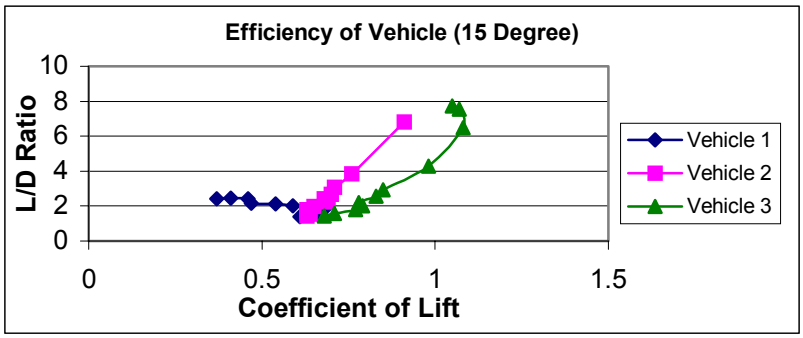

Figure 60: Coefficient of lift vs. L/D ratio for 15° wing angle

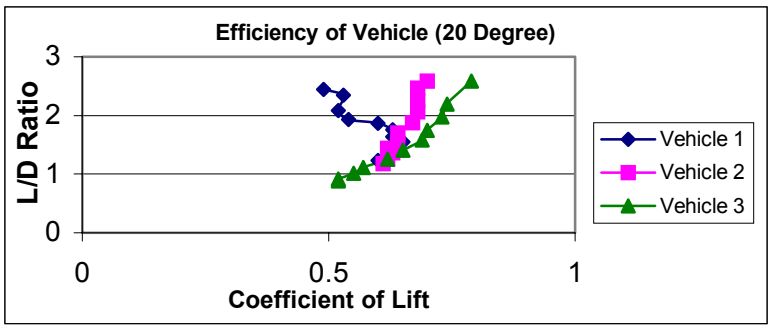

Figure 61: Coefficient of lift vs. L/D ratio for 20° wing angle

9.10 Summary Comparison between Underwater Results and Wind Tunnel Results

Results from the underwater and wind tunnel tests offer unique insights into the behavior of the underwater gliders. The wind tunnel results illustrate similarities and differences when compared tothe hydrodynamic test. The underwater analysis displayed in figures 26-41 provides data relating to velocity, angle of descent, and glide ratio, while the wind tunnel results depicted in figures 46-61 addresses trends in coefficients of lift and lift-to-drag ratios.

In terms of similarities, both experiments showed the 5° wing angle of vehicle 2 and 0° wing angle of vehicle 3 achieved the highest lift and lift-to-drag ratio. For higher wing angles at 15° and 20°, the wind tunnel and hydro tank also proved vehicle 1's delta wing yielded a higher glide ratio than the cambered wing on vehicle 3. For body shape and size, both experiments favor the smaller, thinner and more streamlined body of vehicle 2 over that of vehicle 3 - a result derived from a higher glide ratio underwater and higher lift-to-drag ratio in the wind tunnel. Another commonality is that at wing angle 20°, the majority of test trails underwater represent stalls, which were definitely confirmed by the wind tunnel experimental results.

In observing differences between both experiments, wing shape data from both experiments was different at higher wing angles. At every wing angle in the hydro tests, the delta shaped wing induced a higher glide ratio and velocity. In the wind tunnel however, the lower wing angles of 0°, 5°, and 10° provided higher lift-to-drag ratios and coefficients of lift with the cambered wing. With 15° and 20° wing angles, wind tunnel data shows the delta wing to have a higher coefficient of lift and higher lift-to-drag ratio. Another primary difference discussed in section 9.1 is the minor differences in Reynolds numbers between airflow and underwater velocity. As a result of this disagreement, different numerical results were recorded, but similar trends that can be interpreted into behaviors.

X Recirculation Tank

As a result of the limitations of the wind tunnel experimental technique and the complexity in relating the wind tunnel data to the underwater test trials, the next step in this project focused on developing another methodology for analyzing underwater gliders. In this next experiment, the idea of a water recirculation tank was conceived in order to combine the principles of a wind tunnel with underwater performance analysis. The primary advantage of studying glider models in a water recirculation tank is the potential to test and observe the vehicles in the medium of water rather than air. Another vital benefit is gaining accurate and precise data about the forces acting on a model through observation rather than interpretation. The problems facing this investigation involve creating a steady laminar flow across a vehicle and building a dual-axis sensor system to measure lift and drag forces underwater. Since this experimental apparatus has not been extensively studied, this final portion of the project will represent a simple proof of concept.

10.1 Basics of Fluid Flow

In fluid flow, effects of friction and viscosity introduce shear stresses between neighboring fluid particles when they move at different velocities. In the case of an ideal fluid flowing through a straight conduit, all particles move in parallel lines with equal velocity. In reality, real fluid flow will have zero velocity adjacent to a wall; it will increase rapidly within a short distance from the wall to produce a velocity profile [10].

10.2 Flow Rate

The idealized objective in designing and building a water recirculation tank is that the flow will be steady and laminar. A truly uniform flow is one in which the velocity is the same in both magnitude and direction at a given instant at every point in the fluid. The quantity of fluid flowing per unit time across any section is referred to as flow rate. It is expressed in cubic feet per second (ft^3/s) or gallons per minute (gpm), which are known as the volume flow rate. For the purpose of this research, the desired flow rate will occur over a 22" x 6" area because those dimensions will entirely encompass the body and wings of underwater vehicles 1, 2, and 3. In addition, the desired velocity of flow rate will be 1.0 ft/s, which is equivalent to the recorded velocities of the underwater tests illustrated in appendices 1-3. Flow measurement is determined by average velocity multiplied by the cross-sectional area. Therefore, the desired flow rate is as follows:

$$Q(flowrate) = A(area) \times V(velocity) = 6in \times 22in \times 12\,{}^{in}/_{s} \Rightarrow \tag{15}$$

$$= 1584\ {}^{inches^3}/_{s} \Rightarrow$$

$$= 1584\left(\frac{in^3}{\sec}\right)\left(\frac{60\sec}{\min}\right)\left(\frac{ft^3}{1728in^3}\right)\left(\frac{7.481gal}{ft^3}\right) = 411.5\ {}^{gal}/_{\min} \Rightarrow$$

$$= 411.5\left(\frac{gal}{\min}\right)\left(\frac{60\min}{hour}\right) = 24690\ {}^{gal}\!/_{hour}\,(gph)$$

10.3 Water Recirculation

The objective of this experiment was that water flow would induce lift and drag forces upon the glider model. The key features of the recirculation tank were high flow quality and horizontal orientation. The tank was operated as a continuous flow channel, negating the need for a sealed cover around the vehicle. This also provided model access while the water flow was running.

The flow straightener was constructed of PVC and made up of four parts: bilge pumps, inlet manifolds, honeycomb, and a test section. Six pumps shown in figure 62 generated the flow. Each pump was capable of moving 1100 gallons of water per hour and aligned with each other as shown in figure 63.

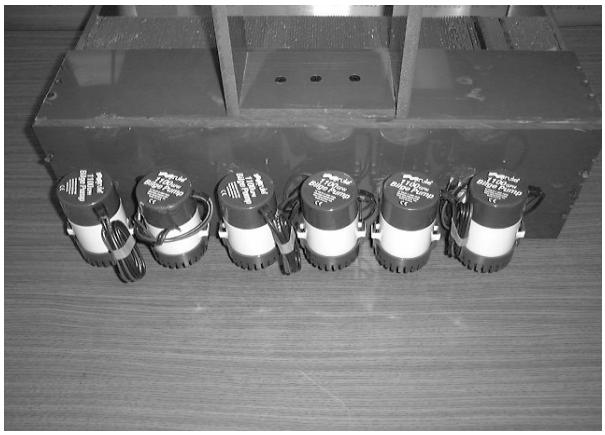

Figure 62: 6 bilge pumps to circulate water

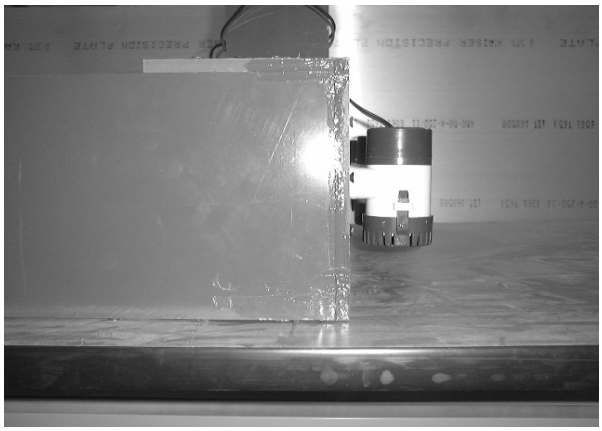

Figure 63: Side view of pumps aligned

Although not visible in figure 63, the pumps are affixed to the PVC, which encloses the honeycomb displayed in figures 65. Between the honeycomb and the pumps is a small void of space, 3 inches in length. This empty space is intended to fill up with water, creating a manifold of water, acting as a boundary between the pressure of the pumps and the initial flow before it is straightened. The fundamental purpose of this manifold is to reduce turbulence to an acceptable level, and reduce the mean velocity variations directly from the pumps. Additionally, by having this barrier, the proportion of water that moves by through the channel will be increased.

Each pump uses 12 volts and 6 amps; however, to produce a higher flow rate and drive the electric motors faster, more current and voltage were provided. As shown in figure 64, the DC energy sources actually supplied 13.8 volts and 6 amps to a pump. Each pump was attached to a constant DC voltage supply in order to insure that each of them were running at the same speed and moving the same amount of water.

Figure 64: 3 DC power sources

As shown in Figures 65 and 66, the primary flow straightener is the honeycomb. It reduced turbulence levels and created a uniform flow in the test section of the water channel. With cells elongated in the flow direction, the honeycomb naturally produced some turbulence, but was still effective in maintaining laminar flow.

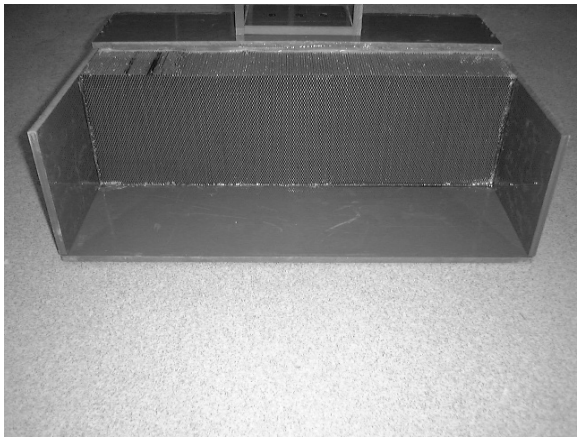

Figure 65: Close-up view of honeycomb

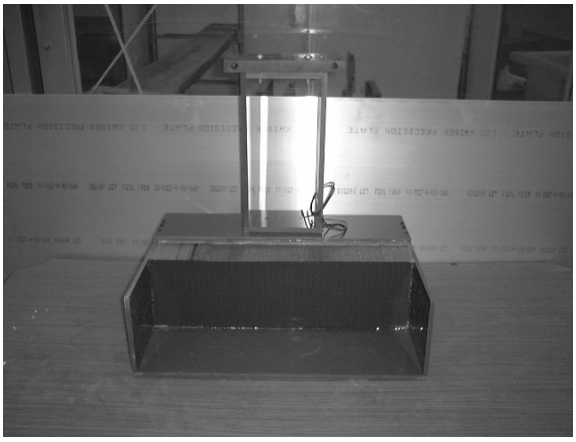

Figure 66: Front view of honeycomb

The test section of the recirculation tank is 22” x 6” – a flat plate area that was intended to be larger than the front surface area of the underwater gliders including the body and wings. The test section is exactly 8” beyond the honeycomb.

10.4 Measuring flow rate

It is important to note that optimization of the flow field is not the objective of this experiment; however, it was important to verify a steady, laminar flow. In order to accomplish this verification, a flow sensor was needed to accurately measure water velocity. The conditions

for selecting a sensor included accuracy, cost, reliability, and ease to use. Through research in fluid mechanics and guidance from the Fluid Measurements Lab at the U.S. Naval Academy, a manometer and pitot tube were identified to be useful in this application. As shown in figure 67, the tube has a small aperture, which can be adjusted to face parallel and perpendicular to the flow. Figure 68 demonstrates that when the tube faces upstream, it is referred to as a pitot tube and it can measure the stagnation pressure. When the tube was rotated, presenting the opening 90° to the flow, then the tube became a static tube and measured static pressure. In this figure, the downward arrows simulate the water flow.

The manometer and pitot tube were mounted to the side of the recirculation tank for accessibility. The height h, inside the tube, to which the liquid rises above the surrounding free surface, is equal to the velocity head in the stream approaching the tip of the tube.

$$P_{Stagnation} = P_{Static} + \rho \frac{v^2}{2} \tag{16}$$

P_{Static} = Static Pressure (psi) P_{Static} = Static Pressure (psi)

v = *velocity* ρ = *density*

Since the water channel is a closed conduit under pressure, it was necessary to also measure the static pressure and subtract this from the pitot reading to secure the differential head h. The differential pressure was measured with a manometer. The formula for the static tube is as follows:

$$P_{Static} = \gamma h \tag{17}$$

γ = specific weight of water h = height of water in column

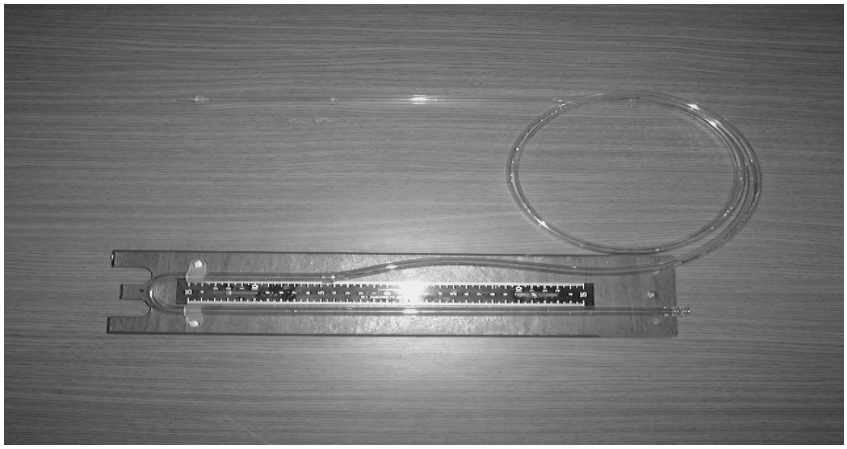

Figure 67: Pitot tubes measuring pressure differential

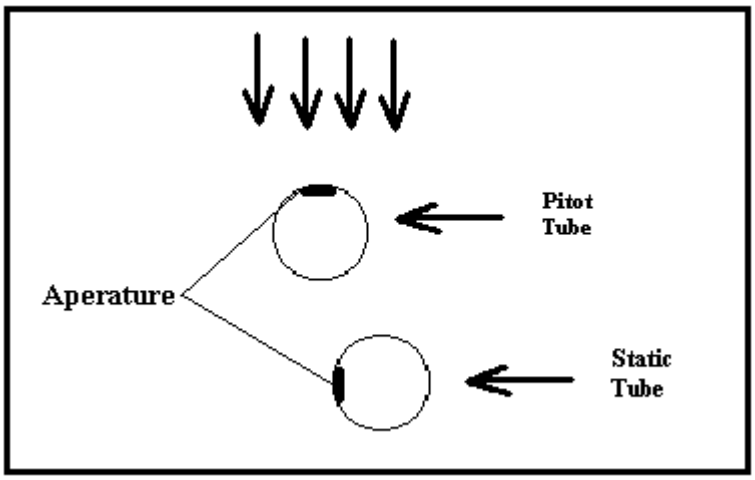

Figure 68: Top view diagram of pitot tube and static tube

In order to insure that some uniformity exists, the velocity of the flow was tested by recording measurements at 1" by 1" intervals and then graphing those results. The Cartesian grid system as shown in figure 69 will provide a means of comparing different areas of the water channel and identifying which areas achieve a desired 1 ft/s flow rate and which lack that desired flow rate. Hence, if square C14 measures a velocity of 1.0 ft/s and square C15 measures a velocity of 1.05 ft/s, then the flow rate will be comparable and a uniform stead flow will be achieved in those two squares of the grid plot.

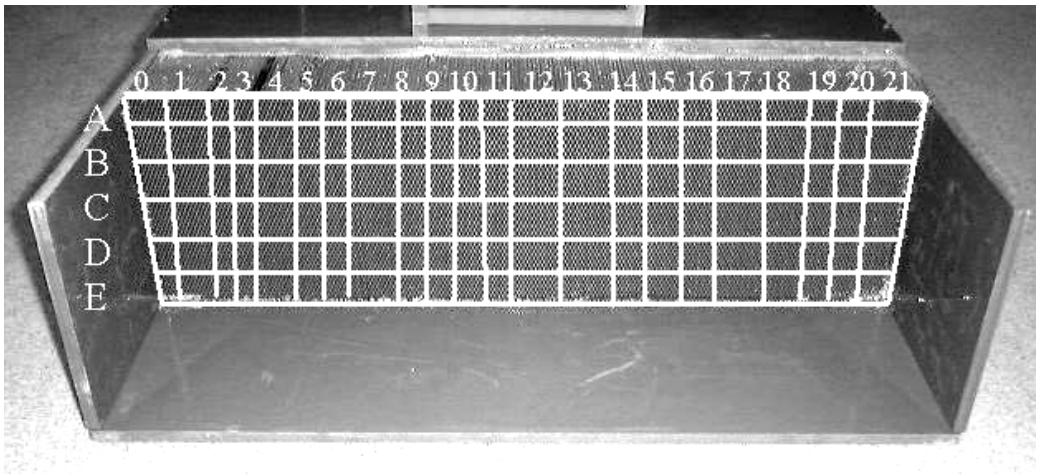

Figure 69: Cartesian plane measuring position of flow rate

In order to ensure an accurate positioning of the tube when it is pitot and static, a ruler was place along the width of the tank and a framework for holding the tube steady was engineered. As shown in figures 70 and 71, this framework allowed the pressure sensing tube to be moved accurately in the horizontal and vertical directions.

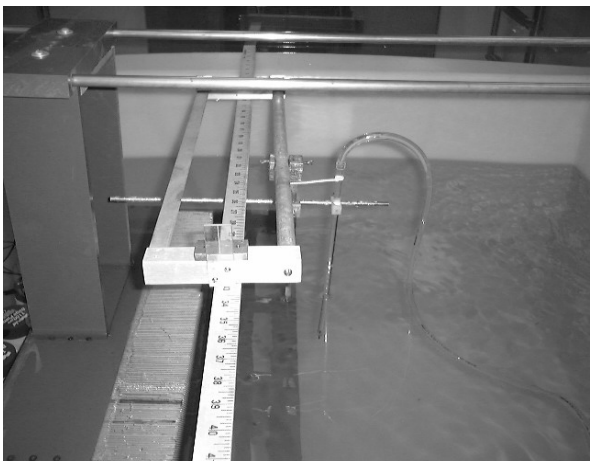

Figure 70: Side view of tube

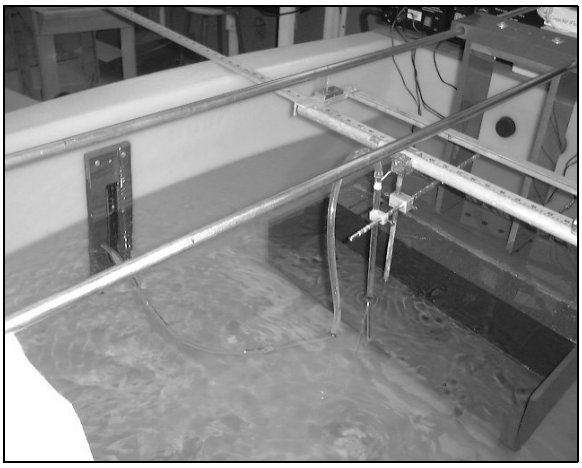

Figure 71: Horizontal and vertical frame

The results of the velocity profile are contained in appendix 7 and display the static pressure, stagnation pressure, and the velocities in each square grid coordinate. The velocities were then plotted in figure 72 according to horizontal and vertical coordinates. Under ideal circumstances, steady uniform flow would be achieved if the magnitude of velocity for each grid coordinate were the same at 1 ft/s. As shown in figure 72, the velocities of each coordinate are clearly not the same; however, the desired flow rate of 1 ft/s is consistently achieved in row D.

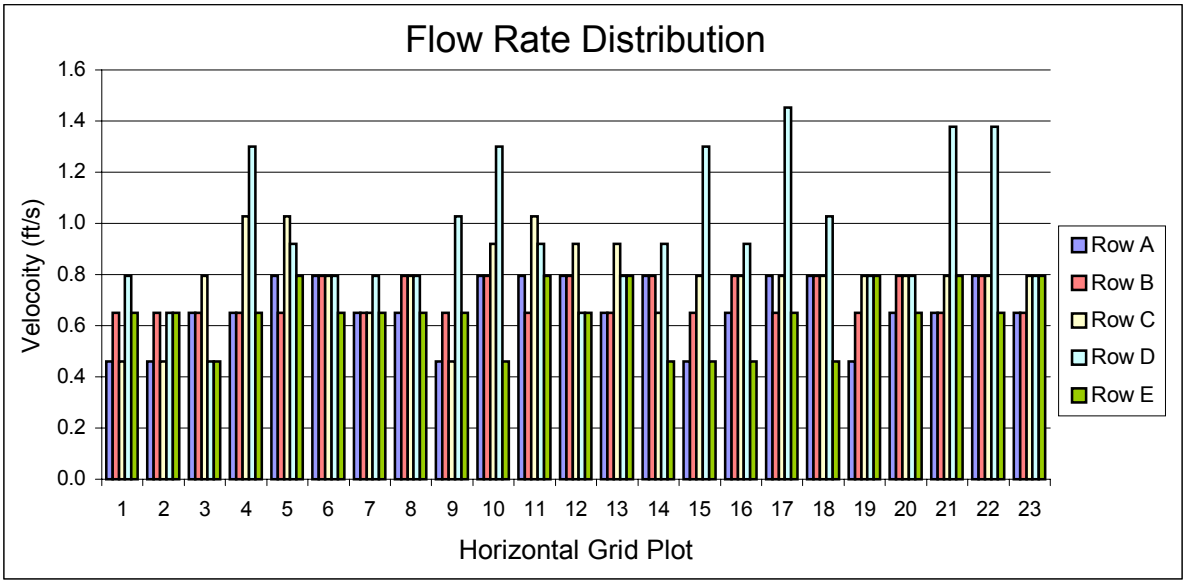

Figure 72: Velocity profile of water flow

In accordance with appendix 7, table 15 below displays the average velocities for each row. Ideally, each grid row would have had an average velocity of 1 ft/s. Again, it is evident that row D obtained the highest water flow rate. The justification for this result is that the pumps were attached to the flow straightener at the height of row D and projected a stronger flow through that row than any others.

Grid Row	Average Velocity (ft/s)
A	0.7
B	0.7
C	0.8
D	1.0
E	0.6

Table 15: Average velocity profile for the recirculation tank

From this velocity profile in the graph and table, it is evident that certain areas of fluid flow achieved the objective in forming a laminar and steady flow. By the basic principles of fluid, the flow coming through the holes in the honeycomb will tend to stick together in irregular patterns and produce flow non-uniformities. With a average flow rate of 0.8 ft/s across the flat plate area, this exercise proved that the recirculation tank was effectively built for two reasons. Primarily, the value of 0.8 ft/s is approximately equal to the desired 1 ft/s outlined in section 10.2. Additionally, based on equation 9 in section 9.1, this flow rate offers a Reynolds number equal to 50,000, which is also equivalent to the values of the Reynolds numbers calculated in appendixes 1-3. In future research, it would be worthwhile to acquire pumps with a higher flow rate to simulate higher velocities that gliders can achieve underwater.

10.5 Sensor System

The sensor system for the water recirculation tank is based upon the idea of the strain gauge balance employed in the wind tunnel. The sensor system in this segment of the investigation is contained in a box that is mounted directly behind and below the glider model in the recirculation tank. The advantage of placing the sensor in the medium and at that location is that the forces being measured are not transposed outside of the water or far from where they are inducing an effect on the vehicle. In terms of the design, the apparatus is very simplistic in theory; however, the degree of accuracy and precision required in the design and machinery is significant. The sensor box and mounting system can be used in the future for future glider models depending on the dimensions of the vehicle regarding shape and size. The apparatus is an achievement in the development of a new methodology, because it represents a dual-axis sensor that is capable of measuring two forces simultaneously in orthogonal directions underwater.

10.5.1 UniForce Sensors

In an effort to accurately measure the forces in normal and axial directions, technology from Force Imagining Inc. known as UniForce sensors, shown in figure 73, were employed. The UniForce sensor functions similar to a variable resistor in an electrical circuit. As force is exerted on the sensor, the two layers of pressure sensitive material compress together and cause a change in resistance (conductance), which corresponds to the force on the sensor. With no load present on the sensor, its resistance is very high. As force increases, the resistance decreases. As force decreases, the resistance increases.

Figure 73: Standard UniForce sensor

The standard UniForce sensor illustrated in figure 74 is about 0.003" thick in the sensing area, 0.0022" thick in other areas. The sensing area is the ¼" diameter silver colored dot on the front side of the sensor . Overall, it is about 0.5" wide and 4.5" long as shown in figure 74.

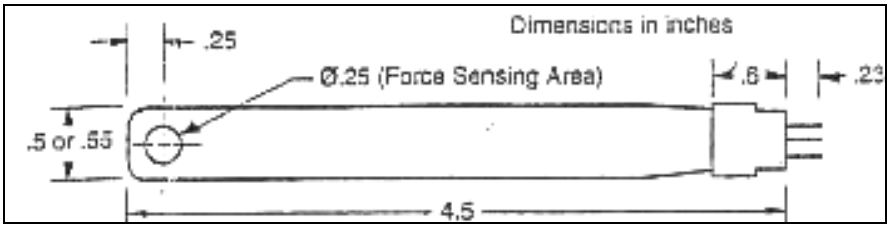

Figure 74: Measurements and diagram of UniForce Sensor

The sensor is constructed with two layers of substrate, polyester and polyimide film. The area of pressure sensitive material in contact with the silver conductive materials is the active sensing area of the sensor. The conductive material extends from the active sensing area to a connector to form conductive leads for connecting the sensor in a circuit. This standard sensor includes a 3-pin connector where the outer two pins are connected to the sensing area.

Typically, the simplest way of reading the force on the sensor is to connect a digital multimeter to the outer two pins of the connector to measure the resistance. Placing pressure on the silver disc part of the sensor produces a corresponding change in electrical resistance. The resistance range will be several M-ohms to fewer than 100 K-ohm. The operation resistance range for a sensor is dependent on the voltage applied. This is due to non-linear voltage-current characteristics of the semi-conductive components of the pressure sensitive material.

Uniforce sensors are durable and ready for use in this application. The sensor technology allows reading forces perpendicular to the plane of the sensor. It is worthwhile to take note that strong shear forces will reduce the life and consistency of sensor performance.

The entire sensing area of a UniForce sensor is read as a single contact force point. For accurate detection of forces, the sensor needs to be loaded in a consistent manner. Ideally, the

entire sensing area should be loaded, and the load should be evenly distributed over the sensing area. If the load was applied to different parts of the sensor area, or the load distribution changed over the sensing area, the sensor resistance, and therefore the force readings, would vary. In order to rectify this problem, the sensors shown in figures 75 and 76 were both preloaded and fixed so the contact surfaces would be flush against the sensing areas.

10.5.2 Original Prototype

The objective of the sensor system is to measure the forces of an underwater glider in the normal and axial directions, which will then be translated into lift and drag. In order to accomplish this task, it is necessary to configure the sensors in a dual-axis system that will register both values into a computer code simultaneously. Figures 75 and 76 exhibit a working prototype sensor consisting of a wooden box ¾" x ¾" x ¾" with a mouse ball. The ball is forcibly placed inside, flush against the back and bottom of the open-faced box. Between the walls and surface of the balls are the UniForce sensors hooked up to digital multimeters. By pushing on the ball from the top, the bottom sensor's resistance will vary, while pushing from the front direction will alter the back sensor's resistance. When pushing from any one direction, there is some modicum of change in the supplementary sensor. Finally, when pushing on the ball from a direction of diagonal origins, both sensors vary their resistance and illustrate that they can mutual sense forces in two directions.

In observing the relationship between force and resistance changes, it should be noted that there is no apparent movement in the ball, because it is tightly placed inside the box and against the wall. The change in resistance is due solely the influence of static pressure. Additionally, when the pressure subsided after each trial, the resistance returned to its open state and pre-loaded status. In order to measure the applied force versus resistance in the actual sensor system, it will be important to test the sensors with weights and measure the linearity of these passive devices in a circuit.

Figure 75: Prototype of dual-axis sensor

Figure 76: Top view of prototype sensor

10.5.3 Final Prototype

The final prototype sensor system is shown below positioned in the recirculation tank in figures 77-79 with vehicle 2 mounted on the sting. The normal and axial force sensors are located directly behind the vehicle inside a box that can be pictured in figure 77 and 78. The vehicle and sensor box are attached to a 12" channel welded to the 3" I-beam that traverses the

length of the tank, both consisting of aluminum. The rationale behind selecting these materials to suspend the vehicle in the water was based on the assumption that the glider models needed to be still in the water and required a robust and efficient means of eliminating minor movements under different water flow rates.

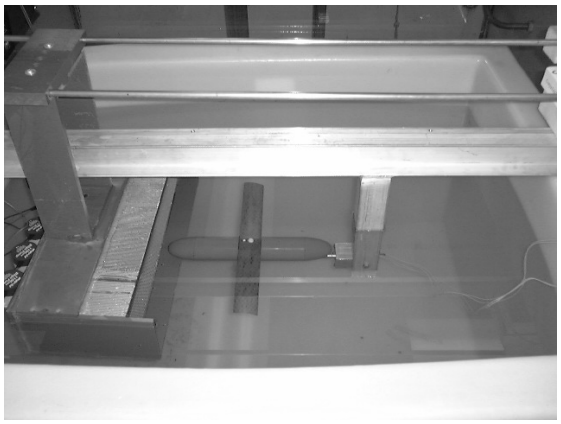

Figure 77: Side view of final prototype

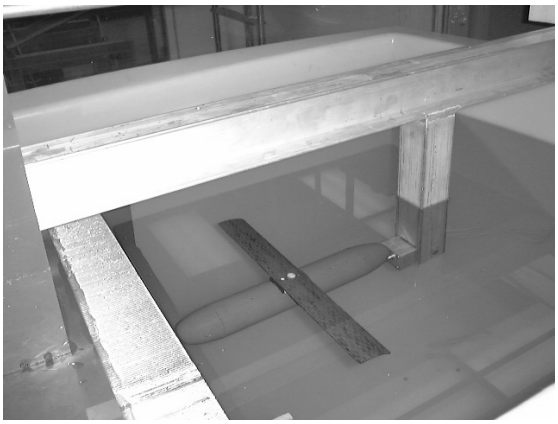

Figure 78: Front view of final prototype

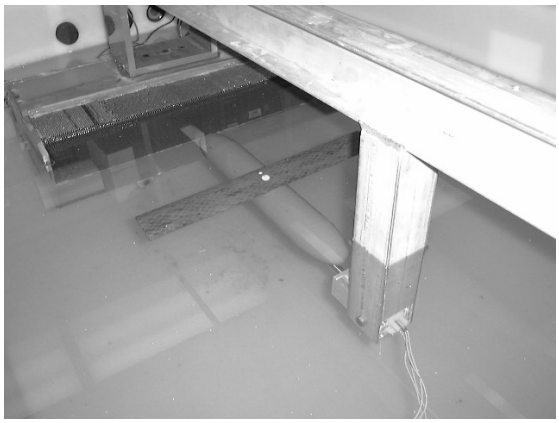

Figure 79: Rear view of final prototype

Below in figures 80 and 81 is the sensor box containing the UniForce sensors that measure the normal and axial forces of the vehicle. The sensors, identified and described in 10.5.1 of this report are arranged in the box as seen in figure 82-83. The sensor box is entirely submerged in water, so it was necessary to waterproof the wires and sensors before placing them in the sensor box. It should be noted that the precision at which the sensor box was constructed was based on .001 inch, which exemplifies the need for accuracy when dealing with sensitive sensor readings.

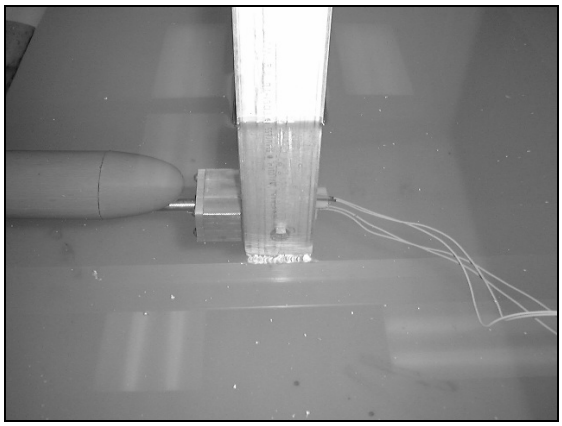

Figure 80: Side view of sensor box

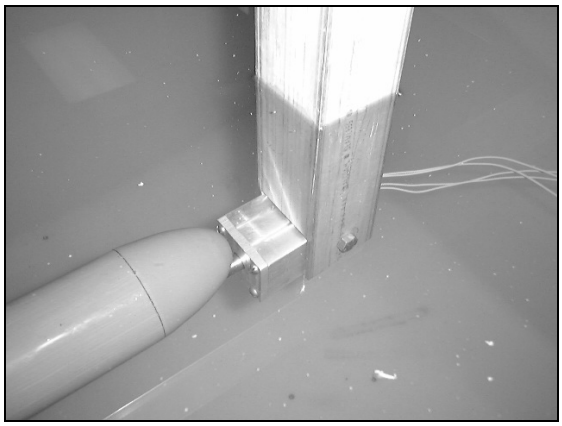

Figure 81: Diagonal view of sensor box

The UniForce sensors are positioned on the top and back of the sensor box to measure the normal and axial forces, respectively as shown in figures 82 and 83.

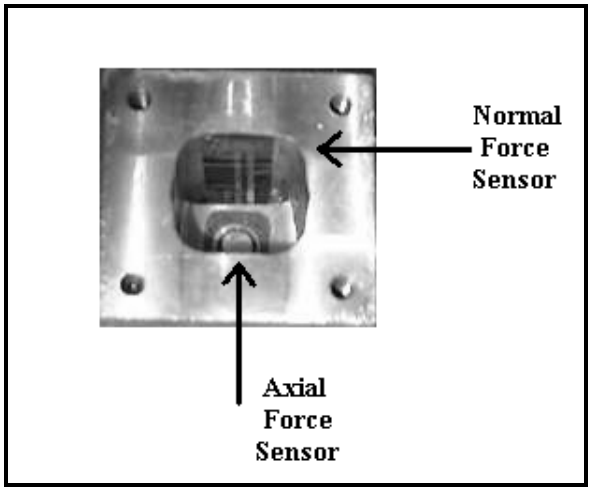

Figure 82: Placement of UniForce sensors

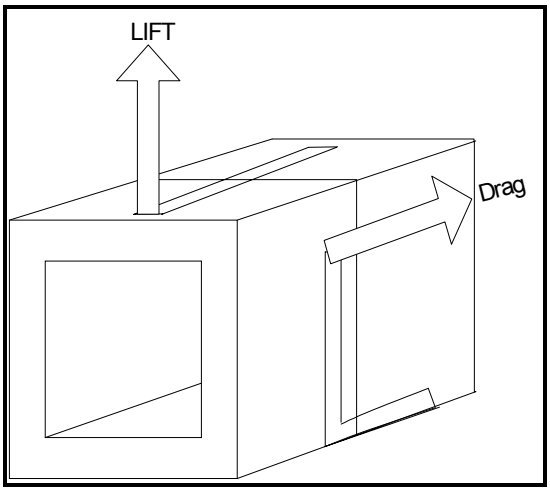

Figure 83: Position of Uniforce sensors

The connecting member between the glider models and the variable resistance sensors is the sting mount pictured in figure 84. This hexagonal piece of bronze was machined to fit precisely into the opening in the sensor box, so that the topside and backside would be flush against the sensors. A hexagon shape was selected because of the ease in placing it inside the box and ensuring that it would be stable and not rotate. In addition, the cylindrical front of the mount was machined to rest underneath the glider models utilizing the same holes that were used to mount the vehicles in the wind tunnel. This was done to minimize any further changes on the underwater gliders.

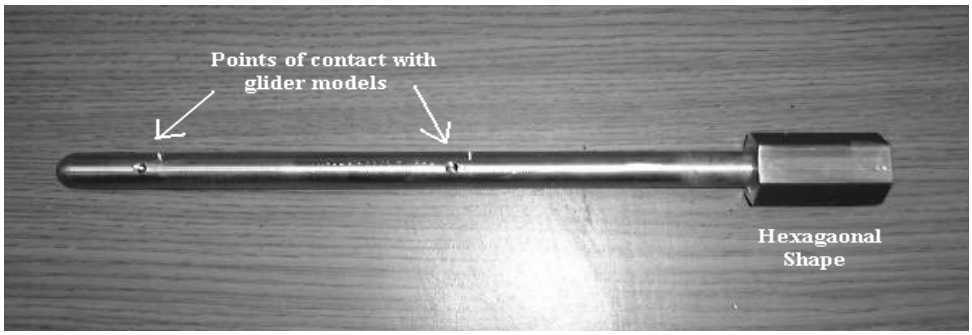

Figure 84: Sting mount connecting the underwater glider to the sensor box

As seen in figure 85, the sting mount also has a front plate that is used for additional stability in the sensor box and can be tightly secured in order to preload the axial sensor.

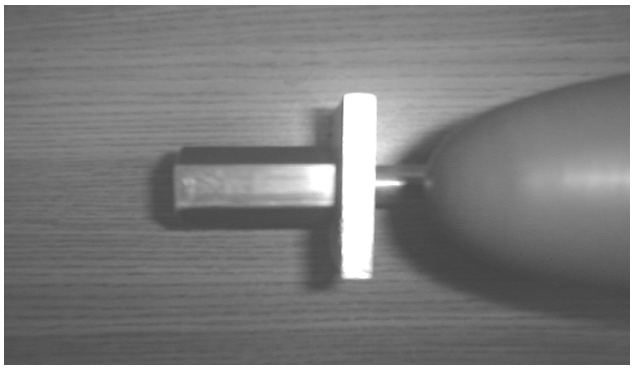

Figure 85: Sensor mount with front plate attached to vehicle 2

After the glider model is attached to the sting mount as shown in figure 85, it is then placed inside the sensor box with the front plate securely attached as seen in figure 86. In order to validate the dual axis sensor, the forces corresponding to the lift and drag forces illustrated in figure 86 must be observed and recorded.

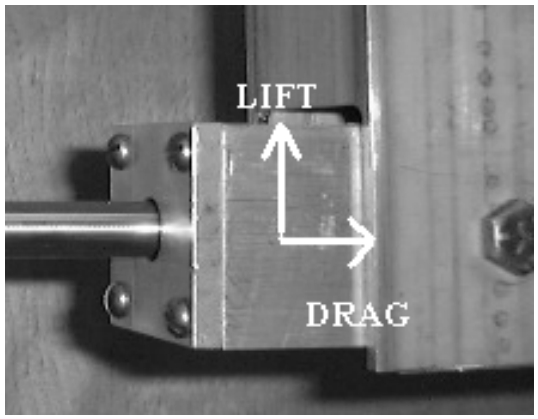

Figure 86: Measuring lift and drag from the UniForce sensors

10.5.4 Protoboard Circuit

In order to obtain sensor readings, a sensor was designed to convert the variable resistance from the UniForce sensors into force readings. The wires appearing in figures 80 and 81 attached the waterproof sensors to the circuit, read the resistance and converted the reading into a voltage using a wheatstone bridge and a INA118 microprocessor. Displayed in figure 87, the circuit provides a driving voltage and current to the sensor. The circuit was connected to a PC using an analog-to-digital converter, which changed the analog voltage (or current) to a digital value. This interface system provided power to the sensors and observes experimental results

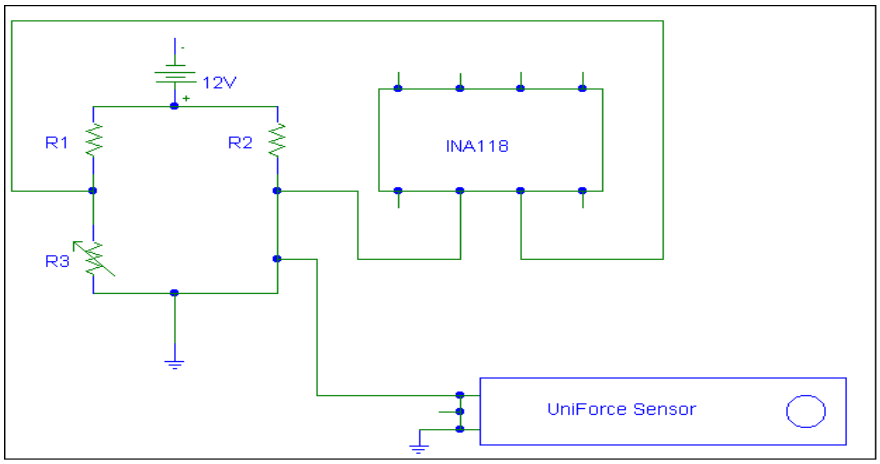

Figure 87: Circuit utilized to convert force to voltage

Since the sensor system measures forces in the normal (N) and axial (A) directions with two separate sensors, it was necessary to build two separate circuits to convert variable resistances into force readings. Figure 88 exhibits the two identical circuits from figure 87 side by side, which lead to the two separate sensors.

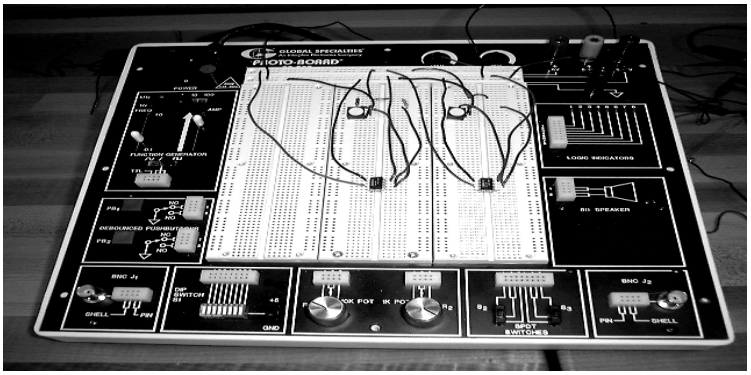

Figure 88: Protoboard with two identical circuits

10.5.5 Sensor Calibration

In order to calibrate the sensors, a series of weights were used as shown in figure 89. Due to the cylindrical shape of the sting mount and the holes at the center each mass, the weights were carefully balanced upon the top of the sting mount and the front of the sting mount as shown in figures 90 and 91.

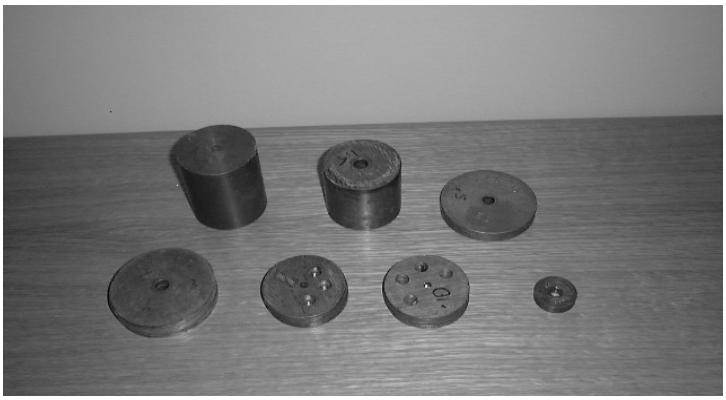

Figure 89: Calibration weights

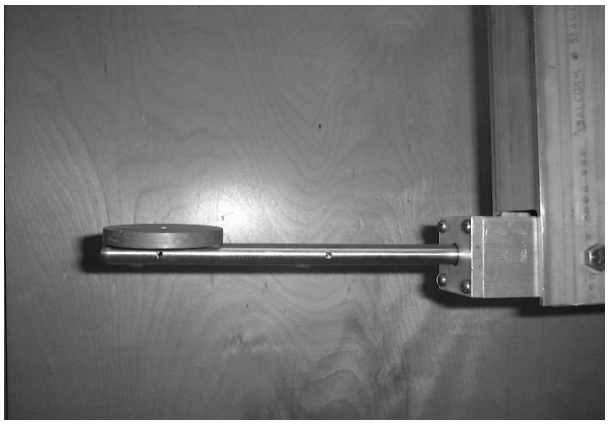

Figure 90: Balancing weight in normal direction

Figure 91: Balancing weight in axial direction

In order to determine the range and sensitivity of the sensor system, incremental weights of .05 lbs, ranging from 0 to 2 lbs, were employed to provide graphical and numerical displays of the force level on the sensor. In order to derive the relationship of the sensor measuring the normal force, the boxes containing the sensors were placed upside down in the mount, as depicted in Figure 92 and 93, and weights were placed upon the topside of the sting mount.

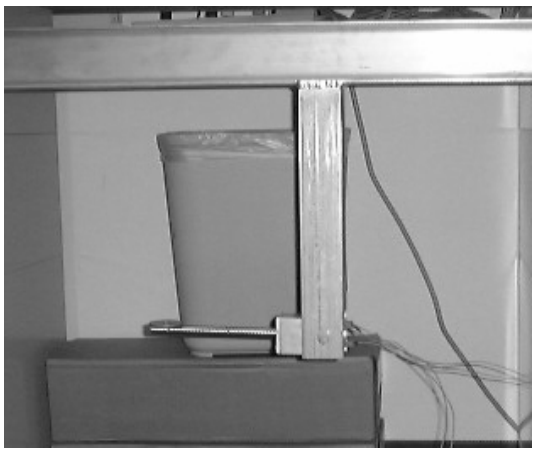

Figure 92: Side view of calibration

Figure 93: Full view of calibration

For the sensor measuring the axial force, the I-beam of the sensor system was placed vertically on the floor, suspended between two chairs as illustrated in Figures 94 and 95.

Figure 94: Front view of calibration

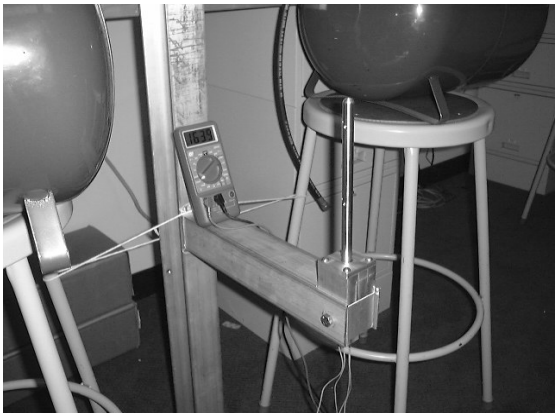

Figure 95: Full view of calibration

In order to test the relationship between force and variable resistance readings of the UniForce sensors, values of resistance were recorded. (Appendix 8) The results were then plotted in figure 96 to display a multipoint calibration, thus allowing correction for any non-linearity of the sensors' responses, and also to convert the displayed force readings into engineering units of pounds. It is clear from the graph that the sensor calibration follows a polynomial line of best fit. The equation of the line was evaluated using Microsoft Excel and is shown in equations 18-19.

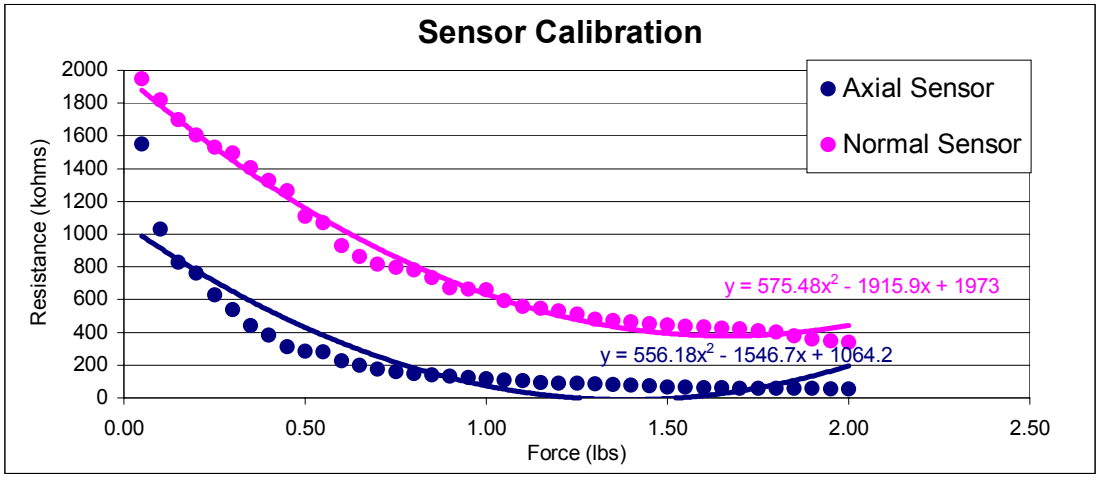

Figure 96: Sensor relationship and line of best fit between force and resistance

Below are the equations for the line of best fit for the normal and axial sensor, respectively:

$$y = 575.48x^2 - 1915.9x + 1973 \quad (18)$$

$$y = 556.18x^2 - 1546.7x + 1064.2 \quad (19)$$

It is important to note that the sensor calibration was conducted outside of the recirculation tank due to difficulty in handling the weights underwater - an obvious limitation of working with sensors underwater.

10.5.6 Signal Conditioning

Applying a curvilinear relationship between force and resistance served as the basis for developing a relationship between force and voltage. This process is known as signal conditioning. Using a Wheatstone bridge circuit with 4 separate resistors, it was possible to measure small changes if 1 resistor changed. By attaching this circuit to the power amplifier, a voltage can then be amplified. A variable resistor, representing the UniForce Sensor, was then substituted into the bridge and altered according to the resistor values from the sensor calibration in appendix 8 to obtain the voltage levels for each particular resistance. As seen in appendix 9, the level of force ranged from 0.2 lb to 0.65 lb. for the axial sensor and 0.35 lb to 1.05 lb for the normal sensor. From this process, a nonlinear relationship was identified and plotted in figure 97. The equations for the lines of best fit are displayed in equation 20 and 21.

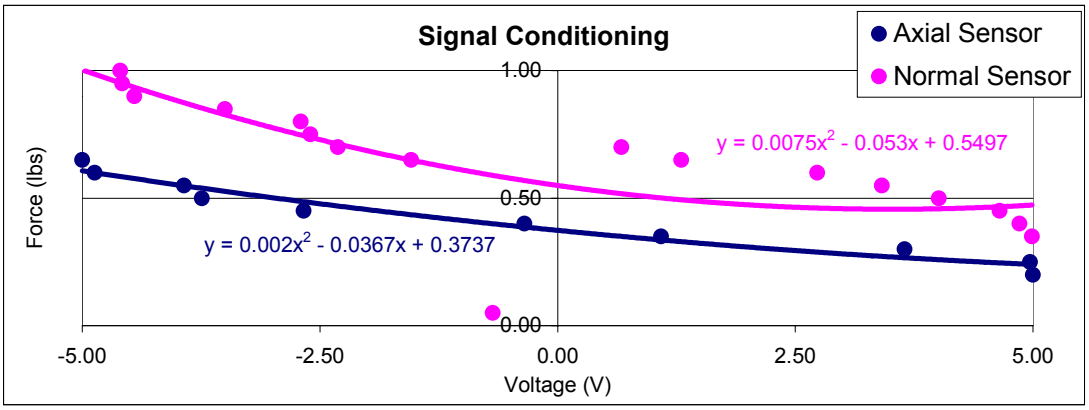

Figure 97: Signal conditioning of force sensors

Below are the equations for the line of best fit for the normal and axial sensor, respectively:

$$y = 0.0075x^2 - 0.053x + 0.5497 \quad (20)$$

$$y = 0.002x^2 - 0.0367x + 0.3737 \quad (21)$$

10.5.7 Software Revised

Initially, the digital values read by the sensor were voltages; however, through the process of signal conditioning and the relationship illustrated in figure 97, the voltages are now automatically transformed into pounds of force. Adding equations 20 and 21 into the computer program on the PC allowed this relationship between force and variable resistance to be displayed, recorded, and analyzed in this investigation.

10.5.8 Problems with Sensor System

In the process of designing and building the sensor system, the problems overcome offered lessons for future study in measuring forces on underwater gliders. In the beginning tests, a primary problem was positioning the strongest areas of water flow in line with the wings of the vehicle, which were responsible for the greatest amount of lift. In order to fix this problem, the pumps were elevated to the necessary level.

Another challenge involved waterproofing the sensors. Although the normal sensor functioned properly, mounting the axial sensor created problems. In four separate cases, the axial sensor shorted out due to problems associated with waterproofing.

The sting mount, although engineered to $1/1000$ of an inch, required two sections of metal shim so that the top and back of the hexagonal shape were flush against the sensors. It was anticipated that achieving the precision needed would be difficult. To visualize this phenomenon, figure 98 below displays an exaggerated depiction of the sting mount contacting the normal force sensor and missing the axial force sensor.

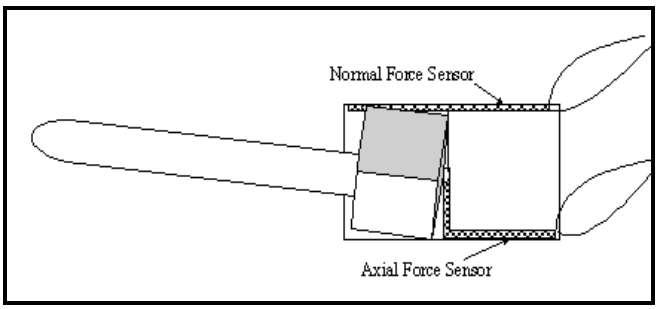

Figure 98: Exaggerated orientation of sting mount

Another problem in the sensor system occurred when sliding the sting mount into the sensor box. There was a tendency for the sensors to change in position and slide out of place, causing other segments to bend and possibly affecting the reading. As a solution, the sensors were taped into placed with double-sided tape, attached using rubber silicon, and eventually glued into place using superglue. Concern was taken in each of these instances to ensure that no substance was attached to the pressure sensitive areas. It is also important to note that possible shear forces rubbing against the sensors could have influenced the sensor readings.

Another consideration in preloading the sensors was the buoyancy of the vehicle and weight of the mount. Using vehicle 3 with 0.25 lb of internal ballast, the normal sensor was preloaded using the upward buoyant force acting on the submerged vehicle.

10.6 Water Recirculation Procedure

Since the functionality of the water recirculation tank and the sensor system was based upon the principles of the wind tunnel, it was reasonable to apply similar procedural methods in order to collect and analyze the data. When measuring hydrodynamic forces using the system of Uniforce sensors, lift (L) and drag (D) cannot be measured directly, because the sensor box can only measure normal (N) and axial (A) forces. These unknown values can be evaluated through trigonometric formulas using sting angle of attack (α).

$$L = N\cos(\alpha) - A\sin(\alpha) \quad (22)$$

$$D = N\sin(\alpha) - A\cos(\alpha) \quad (23)$$

In order to determine values for the normal and axial forces, the data must be adjusted to account for the weight of the model. Prior to turning on the recirculating water, it was necessary to record the values for the normal and axial forces. For each angle of attack, a measurement was taken with the vehicle mounted in still fluid by itself. This process is known as obtaining the tare data and directly enables the balance to be preloaded. In order to obtain the corrected values for the normal and axial force, the tare measurements and raw measurements were recorded in the form of resistances (k-ohms) as shown in appendix 10. These values were then converted into forces (lbs) by applying equations from the sensor calibration (section 10.5.6). The calculated forces in the normal and axial direction must first be subtracted using the following equations:

$$N = N_{raw} - N_{tare} \tag{24}$$

$$A = A_{raw} - A_{tare} \tag{25}$$

The sting tare data for α, N, and A were recorded. Beginning with an initial position of 0° angle of attack and ending with a final position of 10° angle of attack, the values of α, N, and A were recorded in increments of 2° to provide the tare data. Unlike the wind tunnel data, which recorded values from 0° to 20°, the test section of the water recirculation tank was not as large as that of the wind tunnel. This is a constraint of the testing methodology that can be improved upon later. In figures 99 and 100, an underwater glider vehicle is displayed at 0° and 10°, respectively, before being placed in the water tank test section.

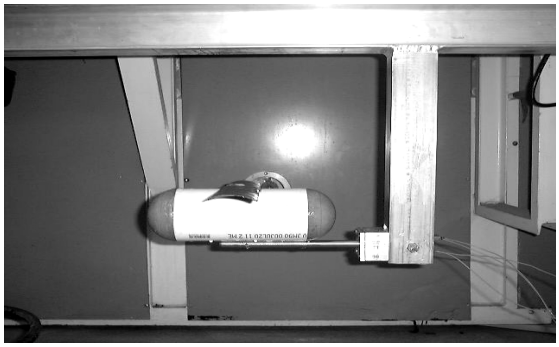

Figure 99: Vehicle 3 at 0° in water tank

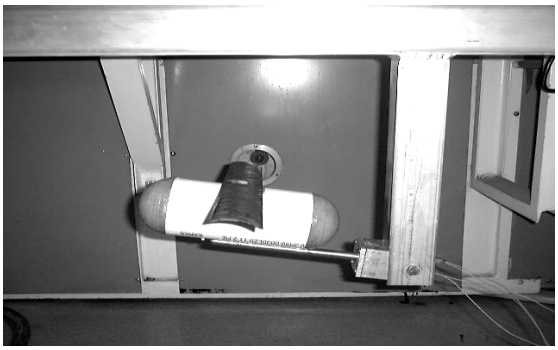

Figure 100: Vehicle 3 at 20° in water tank

At each angle of attack, after tare data was recorded, the bilge pumps were powered to begin steady laminar flow. After ten seconds of establishing the flow, the raw data was recorded for the axial and normal force sensors. The pumps were then turned off and the water in the tank was allowed 1 minute to settle. The angle of attack was then incremented by 2° and the process recommenced.

10.7 Results of Vehicle 3 for Recirculation tank

As noted in the problems with the sensor system, the axial sensor repeatedly shorted out and did not function as a result of problems with waterproofing. The test trials continued and the only force measured was in the normal direction. The sensor system proved to be resilient and versatile in measuring the lifting forces. The results of the sensor readings, the calculated normal force, and the interpolated lifting force are enclosed in appendix 10. In the later segment of this section, figure 101 displays the results of the recirculation tank while Figure 102 exemplifies the results of the wind tunnel. When the two graphs are displayed next to each other, it is possible to see similar trends between the different tests. The graph lines are most apparent for wing angles at 0°, 5°, 10°, and 20°. It should also be noted that the values of the graphs do not correspond because the Reynolds numbers are different between the wind tunnel and the recirculation tank.

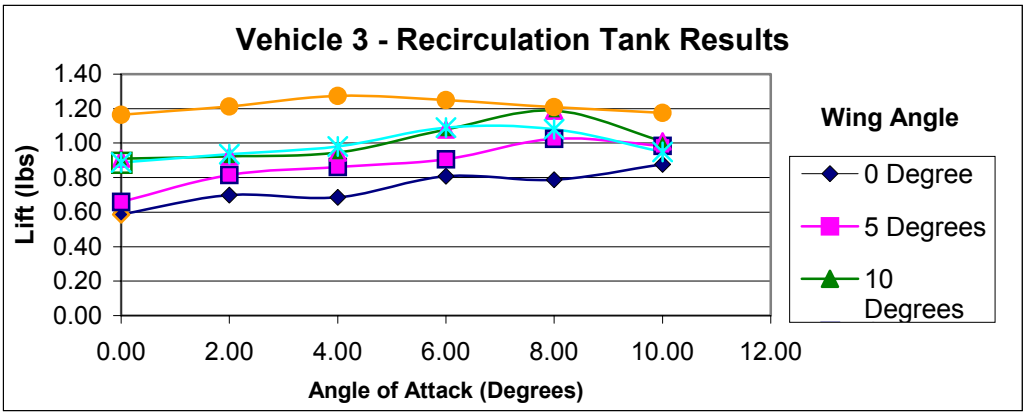

Figure 101: Angle of attack vs. lift for vehicle 3 in the recirculation test

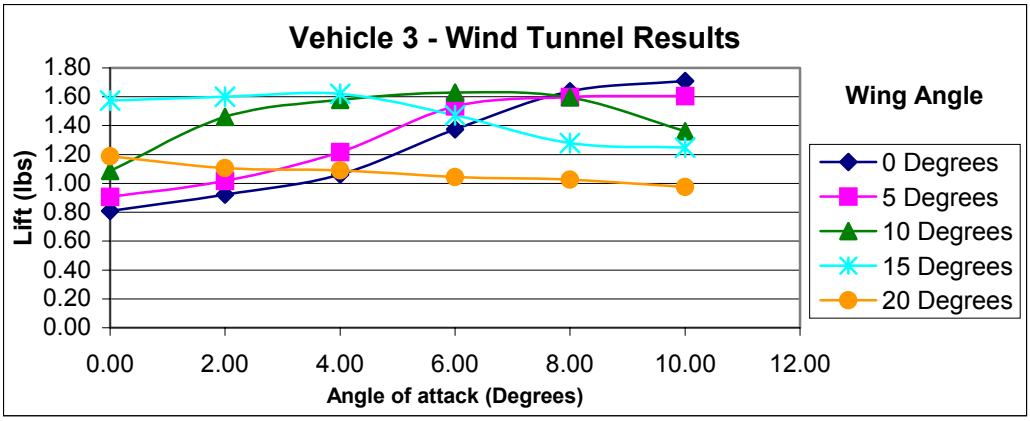

Figure 102: Angle of attack vs. lift for vehicle 3 in the wind tunnel test

The final prototype of the water recirculation tank and dual axis sensor system was successful to a degree. Since there was a correlation between the flow field and the lifting force on the underwater glider, the concept was demonstrated. Conversely, the inoperative axial sensor limited the scope of the project. The research concludes that the recirculation tank can be useful in measuring the underwater forces on glider models. In the future, it would be valuable to continue the experiment and make the sensor box fully operational.

XI Summary

A prototype method for analyzing the behavior and forces acting upon underwater gliders was developed and tested. Underwater tests, wind tunnel tests, and a water recirculation tank were used as the means of collecting empirical evidence on the behavior of the glider models. The research objective was to explore underwater gliding and develop a methodology for testing wing shape, wing angle, and body shape and size.

In order to study the aforementioned variables, three different glider models were constructed and placed in the hydro tank to observe their gliding characteristics. The underwater analysis showed that vehicle 1 with the delta wing shape is better than the cambered wing of vehicle 3 regardless of wing angle. Likewise, vehicle 2 with a thinner, more streamlined fuselage achieved a longer glide ratio than vehicle 3.

The models were subsequently tested in the wind tunnel to further understand their lift and drag characteristics. The wind tunnel studies showed that the lower wing angles of 0°, 5°, and 10° on vehicle 3 induced higher coefficients of lift with the cambered wing than the delta wing on vehicle 1. Additionally, the more slender, aerodynamic fuselage of vehicle 2 yielded higher lift-to-drag ratios than vehicle 3.

Finally, a water recirculation tank with dual-axis sensor was constructed to merge the precepts of the hydro tank with the wind tunnel. In the end, the concept of an underwater sensor system measuring lift was demonstrated. Due to time constraints, only vehicle 3 was tested. In order to determine the functionality of the tank, the data was compared to the results of the wind tunnel. The trends for each angle of attack were closely related, which concluded this proof of concept. Completing this research and providing valuable insights into a new methodology for testing underwater gliders have laid a foundation for future study and development in this direction.

There are many other avenues where further research may also be conducted to improve the understanding of underwater gliders. Foremost, in the design and construction of glider models, it would be favorable to observe wing angles in increments of 1° as opposed to 5° to determine the possibility of a longer glide path. Additionally, varying the airfoil to obtain different iterations of chord, span, and camber will provide further understanding of the resulting lift-to-drag ratio. Another unique inquiry might entail altering the trailing and leading edges of the delta or cambered wings underwater to determine the forces acting on the vehicle. More precise changes in body shape and size would be required in order to determine the limits of efficiency in terms of length and width. Another prime variable when the vehicles are underwater is the buoyancy effect. In this experiment, each vehicle had a negative 0.7 lb force from internal ballast. It would be useful to investigate the optimal buoyancy required for maximum glide ratio.

In reviewing the wind tunnel experiment and determining how to further relate the data to the underwater testing in the hydrodynamics lab, appendixes 4-6 contain Reynolds numbers.

With more data analysis, these numbers can be graphed in relation to lift and drag to extrapolate values at lower Reynolds numbers.

Overall, the concept of a dual-axis sensor measuring lift and drag underwater in a recirculation tank was introduced. While the water flow was laminar and steady, the flow rate was not strong enough to induce a significant change in the resistance of the axial sensor. Therefore, it would be beneficial to install higher rating pumps into the flow straightener to induce a higher lift and drag over the glider models. Since at lower speeds, the drag is smaller, it would be advantageous to identify a means of varying the flow rate to see how the drag of a good shape, such as a streamlined glider, varies with the water velocity. Because the axial sensor only operated for a limited period of time, the first initiative should be to find a means of waterproofing the axial sensor and identifying another means of protecting it from water intrusion to maintain its operability. Another worthwhile study in the water channel is the utilization of colored dyes in the water to determine the pressure distribution and vortices of the water as it flows across the glider models. Data can be taken with still cameras or high-speed videotape recordings. For instance, an airfoil or glider model could be mounted in the water tank to show not only the streamlines associated with a lifting surface, but also the way it is effected by changes in angle of attack. Surface dye ports can be used to show the boundary layer separation that occurs as the angle of attack is increased.

The research of underwater gliding is only just beginning. The technologies for autonomous underwater gliding and its application to mine warfare can prevent the loss of human life and provide for secure navigational passage throughout international waterways and harbors.

XII References

1. Leonard, Naomi and Joshua Graver. “Model-Based Feedback Control of Autonomous Underwater Gliders.” IEEE Journal of Oceanic Engineering,2000.

2. Stommel, H. *The Slocum mission*. IEEE Oceanography, 2:22-25, 1989.

3. Erickson, C.C., T.J. Osse, T. Light, R.D. Wen, T.W. Lehmann, P.L. Sabin, J.W. Ballard, and A.M. Chiodi. “Seaglider: A Long Range Autonomous Underwater Vehicle For Oceanographic Research.” IEEE Journal of Oceanic Engineering, 2001.

4. Sherman, J., R.E. Davis, W.B. Owens, and J. Valdes. “The Autonomous Underwater Glider ‘Spray’.” IEEE Journal of Oceanic Engineering, 2001.

5. Webb, D.C., P.J. Simonetti, and C.P. Jones. “Slocum, An Underwater Glider Propelled By Environmental Energy.” IEEE Journal of Oceanic Engineering, 2001.

6. “MCM CONTECH ’00 WAR GAME: From Concepts to Technology” Sponsored by: Organic Mine Countermeasures Future Naval Capability Program Office. September 2000.

7. Marchaj, C.A. *Sailing Theory and Practice*. Dodd, Mead and Company, New York: 1964.

8. Marchaj, C.A. *Aero-Hydrodynamics of Sailing*. Dodd, Mead and Company, New York: 1979.

9. Shapiro, Ascher H. *Shape and Flow*. Anchor Books: New York, 1961.

10. Franzini, Joseph and John Finnemore. *Fluid Mechanics: Ninth Edition*. McGraw-Hill: Belfast, 1997.

XIII Bibliography

1. Davis, Russ. Valdes, J. "The Autonomous Underwater Glider 'Spray'." IEEE Oceanic Engineering (27 December 1999): 1-17.

2. Franzini, Joseph and John Finnemore. *Fluid Mechanics: Ninth Edition*. McGraw-Hill: Belfast, 1997.

3. Hawley, J.G. Nuckols, M.L. Reader, G.T. I.J. Potter. *Design Aspects of Underwater Intervention* Systems. Kendall: Dubuque, 1996.

4. Hoerner, S.F. *Fluid-Dynamic Drag*. Hoerner: Great Brittan, 1965.

5. Marzek, James. Hang Gliding and Soaring. St Martin's Press: New York, 1976.

14.1 APPENDIX 1 -- Underwater Data for Vehicle 1 sheet 1 of 5

Vehicle 1 – 0° Wing Angle of Attack

Vehicle	Trial	Wing Angle of Attack (degrees)	Horizontal Displacement (inches)	Vertical Displacement (inches)	Total Displacement (inches)	Time of Descent (seconds)	Velocity (ft/s)	Glide Ratio (ft)	Angle of Glide Ratio (degrees)
1	1	0	86.82	36	93.99	7.33	1.07	2.41	25.22
1	2	0	76.94	36	84.95	7.7	0.92	2.14	28.95
1	3	0	84.00	36	91.39	9.8	0.78	2.33	26.18
1	4	0	111.53	36	117.20	10.36	0.94	3.10	19.16
1	5	0	105.18	36	111.17	9.01	1.03	2.92	20.41
1	6	0	93.88	36	100.55	9.86	0.85	2.61	23.11
1	7	0	98.12	36	104.51	7.45	1.17	2.73	22.02
1	8	0	89.65	36	96.61	7.47	1.08	2.49	24.33
1	9	0	77.65	36	85.59	6.56	1.09	2.16	28.65
1	10	0	75.53	36	83.67	5.24	1.33	2.10	29.58

Vehicle	Trial	Wing Angle of Attack (degrees)	Reynolds Number	Velocity of Wind Tunnel (ft/s)	(mph)
1	1	0	98,511.64	31.55	21.51
1	2	0	84,754.09	27.14	18.51
1	3	0	71,643.04	22.94	15.64
1	4	0	86,907.32	27.83	18.98
1	5	0	94,788.51	30.36	20.70
1	6	0	78,343.19	25.09	17.11
1	7	0	107,775.72	34.51	23.53
1	8	0	99,354.02	31.82	21.69
1	9	0	100,232.08	32.10	21.89
1	10	0	122,671.59	39.29	26.79

14.1 APPENDIX 1 -- Underwater Data for Vehicle 1 sheet 2 of 5

Vehicle 1 – 5° Wing Angle of Attack

Vehicle	Trial	Wing Angle of Attack (degrees)	Horizontal Displacement (inches)	Vertical Displacement (inches)	Total Displacement (inches)	Time of Descent (seconds)	Velocity (ft/s)	Glide Ratio (ft)	Angle of Glide Ratio (degrees)
1	1	5	77	36	85.00	5.67	1.25	2.14	28.93
1	2	5	66	36	75.18	4.19	1.50	1.83	34.77
1	3	5	83	36	90.47	6.49	1.16	2.31	26.54
1	4	5	97	36	103.46	6.57	1.31	2.69	22.30
1	5	5	90	36	96.93	5.98	1.35	2.50	24.22
1	6	5	88	36	95.08	5.78	1.37	2.44	24.84
1	7	5	85	36	92.31	5.68	1.35	2.36	25.83
1	8	5	91	36	97.86	6.3	1.29	2.53	23.93
1	9	5	90	36	96.93	5.94	1.36	2.50	24.22
1	10	5	89	36	96.01	6.12	1.31	2.47	24.53

Vehicle	Trial	Wing Angle of Attack (degrees)	Reynolds Number	Velocity of Wind Tunnel (ft/s)	(mph)
1	1	5	115,170.35	36.88	25.15
1	2	5	137,845.27	44.14	30.10
1	3	5	107,095.06	34.30	23.38
1	4	5	120,985.35	38.75	26.42
1	5	5	124,530.33	39.88	27.19
1	6	5	126,375.01	40.47	27.59
1	7	5	124,853.80	39.98	27.26
1	8	5	119,338.07	38.22	26.06
1	9	5	125,368.92	40.15	27.37
1	10	5	120,516.96	38.60	26.31

14.1 APPENDIX 1 -- Underwater Data for Vehicle 1 sheet 3 of 5

Vehicle 1 – 10° Wing Angle of Attack

Vehicle	Trial	Wing Angle of Attack (degrees)	Horizontal Displacement (inches)	Vertical Displacement (inches)	Total Displacement (inches)	Time of Descent (seconds)	Velocity (ft/s)	Glide Ratio (ft)	Angle of Glide Ratio (degrees)
1	1	10	73	36	81.39	9.07	0.75	2.03	30.79
1	2	10	59	36	69.12	6.67	0.86	1.64	40.06
1	3	10	85	36	92.31	7.99	0.96	2.36	25.83
1	4	10	94	36	100.66	8.36	1.00	2.61	23.08
1	5	10	68	36	76.94	6.34	1.01	1.89	33.53
1	6	10	108	36	113.84	14.55	0.76	3.00	19.84
1	7	10	96	36	102.53	7.91	1.08	2.67	22.55
1	8	10	94	36	100.66	7.76	1.08	2.61	23.08
1	9	10	91	36	97.86	7.89	1.03	2.53	23.93
1	10	10	86	36	93.23	7.1	1.09	2.39	25.49

Vehicle	Trial	Wing Angle of Attack (degrees)	Reynolds Number	Velocity of Wind Tunnel (ft/s)	(mph)
1	1	10	68,943.05	22.08	15.05
1	2	10	79,607.98	25.49	17.38
1	3	10	88,757.14	28.42	19.38
1	4	10	92,500.94	29.62	20.20
1	5	10	93,234.45	29.86	20.36
1	6	10	69,688.90	22.32	15.22
1	7	10	99,579.74	31.89	21.74
1	8	10	99,653.07	31.91	21.76
1	9	10	95,288.95	30.52	20.81
1	10	10	100,880.29	32.31	22.03

14.1 APPENDIX 1 -- Underwater Data for Vehicle 1 sheet 4 of 5

Vehicle 1 – 15° Wing Angle of Attack

Vehicle	Trial	Wing Angle of Attack (degrees)	Horizontal Displacement (inches)	Vertical Displacement (inches)	Total Displacement (inches)	Time of Descent (seconds)	Velocity (ft/s)	Glide Ratio (ft)	Angle of Glide Ratio (degrees)
1	1	15	96	36	102.53	11.39	0.75	2.67	22.55
1	2	15	75	36	83.19	6.76	1.03	2.08	29.83
1	3	15	65	36	74.30	6.19	1.00	1.81	35.43
1	4	15	83	36	90.47	8.23	0.92	2.31	26.54
1	5	15	84	36	91.39	9.5	0.80	2.33	26.18
1	6	15	87	36	94.15	9.49	0.83	2.42	25.16
1	7	15	65	36	74.30	5.98	1.04	1.81	35.43
1	8	15	72	36	80.50	6.7	1.00	2.00	31.30
1	9	15	67	36	76.06	7.2	0.88	1.86	34.14
1	10	15	78	36	85.91	7.1	1.01	2.17	28.50

Vehicle	Trial	Wing Angle of Attack (degrees)	Reynolds Number	Velocity of Wind Tunnel (ft/s)	(mph)
1	1	15	69,155.03	22.15	15.10
1	2	15	94,545.87	30.28	20.64
1	3	15	92,219.56	29.53	20.14
1	4	15	84,452.85	27.05	18.44
1	5	15	73,905.45	23.67	16.14
1	6	15	76,221.58	24.41	16.64
1	7	15	95,458.04	30.57	20.84
1	8	15	92,303.36	29.56	20.15
1	9	15	81,156.63	25.99	17.72
1	10	15	92,955.40	29.77	20.30

14.1 APPENDIX 1 -- Underwater Data for Vehicle 1 sheet 5 of 5

Vehicle 1 – 20° Wing Angle of Attack

Vehicle	Trial	Wing Angle of Attack (degrees)	Horizontal Displacement (inches)	Vertical Displacement (inches)	Total Displacement (inches)	Time of Descent (seconds)	Velocity (ft/s)	Glide Ratio (ft)	Angle of Glide Ratio (degrees)
1	1	20	70	36	78.71	6.68	0.98	1.94	32.37
1	2	20	65	36	74.30	8.93	0.69	1.81	35.43
1	3	20	70	36	78.71	7.42	0.88	1.94	32.37
1	4	20	69	36	77.83	6.39	1.01	1.92	32.94
1	5	20	64	36	73.43	5.9	1.04	1.78	36.12
1	6	20	67	36	76.06	6.2	1.02	1.86	34.14
1	7	20	67	36	76.06	6.23	1.02	1.86	34.14
1	8	20	66	36	75.18	6.56	0.96	1.83	34.77
1	9	20	66	36	75.18	7.29	0.86	1.83	34.77
1	10	20	69	36	77.83	7.1	0.91	1.92	32.94

Vehicle	Trial	Wing Angle of Attack (degrees)	Reynolds Number	Velocity of Wind Tunnel (ft/s)	(mph)
1	1	20	90,528.24	28.99	19.77
1	2	20	63,923.75	20.47	13.96
1	3	20	81,499.81	26.10	17.80
1	4	20	93,569.16	29.97	20.43
1	5	20	95,615.38	30.62	20.88
1	6	20	94,246.41	30.18	20.58
1	7	20	93,792.57	30.04	20.48
1	8	20	88,044.46	28.20	19.22
1	9	20	79,227.94	25.37	17.30
1	10	20	84,212.25	26.97	18.39

14.2 APPENDIX 2 -- Underwater Data for Vehicle 2 sheet 1 of 5

Vehicle 2 – 0° Wing Angle of Attack

Vehicle	Trial	Wing Angle of Attack (degrees)	Horizontal Displacement (inches)	Vertical Displacement (inches)	Total Displacement (inches)	Time of Descent (seconds)	Velocity (ft/s)	Glide Ratio	Angle of Glide Ratio (degrees)
2	1	0	93	51	106.07	6.44	1.37	1.82	35.00
2	2	0	85	51	99.13	6.23	1.33	1.67	39.20
2	3	0	103	51	114.93	7.97	1.20	2.02	30.94
2	4	0	84	51	98.27	6.27	1.31	1.65	39.80
2	5	0	74	51	89.87	6.37	1.18	1.45	47.21
2	6	0	78	51	93.19	5.82	1.33	1.53	43.91
2	7	0	72	51	88.23	6.93	1.06	1.41	49.08
2	8	0	87	51	100.85	6.16	1.36	1.71	38.05
2	9	0	73	51	89.05	5.69	1.30	1.43	48.13
2	10	0	89	51	102.58	5.52	1.55	1.75	36.97

Vehicle	Trial	Wing Angle of Attack (degrees)	Reynolds Number	Velocity of Wind Tunnel (ft/s)	(mph)
2	1	0	126,530.49	40.52	27.63
2	2	0	122,237.69	39.15	26.69
2	3	0	110,789.32	35.48	24.19
2	4	0	120,408.84	38.56	26.29
2	5	0	108,390.30	34.71	23.67
2	6	0	123,017.46	39.40	26.86
2	7	0	97,813.97	31.32	21.36
2	8	0	125,772.18	40.28	27.46
2	9	0	120,234.51	38.50	26.25
2	10	0	142,762.74	45.72	31.17

14.2 APPENDIX 2 -- Underwater Data for Vehicle 2 sheet 2 of 5

Vehicle 2 – 5° Wing Angle of Attack

Vehicle	Trial	Wing Angle of Attack (degrees)	Horizontal Displacement (inches)	Vertical Displacement (inches)	Total Displacement (inches)	Time of Descent (seconds)	Velocity (ft/s)	Glide Ratio	Angle of Glide Ratio (degrees)
2	1	5	115	51	125.80	8.09	1.30	2.25	27.22
2	2	5	119	51	129.47	7.96	1.36	2.33	26.18
2	3	5	135	51	144.31	10.4	1.16	2.65	22.74
2	4	5	142	51	150.88	12.32	1.02	2.78	21.51
2	5	5	83	51	97.42	10.51	0.77	1.63	40.43
2	6	5	149	51	157.49	13.33	0.98	2.92	20.41
2	7	5	148	51	156.54	14.37	0.91	2.90	20.56
2	8	5	159	51	166.98	12.79	1.09	3.12	19.04
2	9	5	103	51	114.93	9.12	1.05	2.02	30.94
2	10	5	136	51	145.25	10.56	1.15	2.67	22.55

Vehicle	Trial	Wing Angle of Attack (degrees)	Reynolds Number	Velocity of Wind Tunnel (ft/s)	(mph)
2	1	5	119,465.33	38.26	26.09
2	2	5	124,955.29	40.02	27.28
2	3	5	106,604.22	34.14	23.28
2	4	5	94,086.63	30.13	20.54
2	5	5	71,209.05	22.80	15.55
2	6	5	90,764.92	29.07	19.82
2	7	5	83,690.35	26.80	18.27
2	8	5	100,298.91	32.12	21.90
2	9	5	96,819.18	31.01	21.14
2	10	5	105,669.89	33.84	23.07

14.2 APPENDIX 2 -- Underwater Data for Vehicle 2 sheet 3 of 5

Vehicle 2 – 10° Wing Angle of Attack

Vehicle	Trial	Wing Angle of Attack (degrees)	Horizontal Displacement (inches)	Vertical Displacement (inches)	Total Displacement (inches)	Time of Descent (seconds)	Velocity (ft/s)	Glide Ratio	Angle of Glide Ratio (degrees)
2	1	10	95	51	107.82	7.51	1.20	1.86	34.10
2	2	10	119	51	129.47	10.66	1.01	2.33	26.18
2	3	10	83	51	97.42	8.96	0.91	1.63	40.43
2	4	10	82	51	96.57	8.03	1.00	1.61	41.07
2	5	10	96	51	108.71	7.56	1.20	1.88	33.67
2	6	10	97	51	109.59	8.65	1.06	1.90	33.25
2	7	10	123	51	133.15	10.35	1.07	2.41	25.22
2	8	10	143	51	151.82	11.83	1.07	2.80	21.35
2	9	10	110	51	121.25	10.45	0.97	2.16	28.65
2	10	10	150	51	158.43	12.29	1.07	2.94	20.27

Vehicle	Trial	Wing Angle of Attack (degrees)	Reynolds Number	Velocity of Wind Tunnel (ft/s)	(mph)
2	1	10	110,301.15	35.32	24.08
2	2	10	93,306.20	29.88	20.37
2	3	10	83,527.58	26.75	18.24
2	4	10	92,387.60	29.59	20.17
2	5	10	110,468.04	35.38	24.12
2	6	10	97,333.02	31.17	21.25
2	7	10	98,836.84	31.65	21.58
2	8	10	98,595.15	31.57	21.53
2	9	10	89,137.81	28.55	19.46
2	10	10	99,037.22	31.72	21.62

14.2 APPENDIX 2 -- Underwater Data for Vehicle 2 sheet 4 of 5

Vehicle 2 – 15° Wing Angle of Attack

Vehicle	Trial	Wing Angle of Attack (degrees)	Horizontal Distance (inches)	Vertical Distance (inches)	Total Distance (inches)	Time of Descent (seconds)	Velocity (ft/s)	Glide Ratio	Angle of Glide Ratio (degrees)
2	1	15	135	51	144.31	11.21	1.07	2.65	22.74
2	2	15	104	51	115.83	13.78	0.70	2.04	30.59
2	3	15	109	51	120.34	9.97	1.01	2.14	28.95
2	4	15	107	51	118.53	10.35	0.95	2.10	29.58
2	5	15	120	51	130.39	11.16	0.97	2.35	25.93
2	6	15	100	51	112.25	11.12	0.84	1.96	32.05
2	7	15	82	51	96.57	6.77	1.19	1.61	41.07
2	8	15	83	51	97.42	7.12	1.14	1.63	40.43
2	9	15	130	51	139.65	12.32	0.94	2.55	23.71
2	10	15	89	51	102.58	7.16	1.19	1.75	36.97

Vehicle	Trial	Wing Angle of Attack (degrees)	Reynolds Number	Velocity of Wind Tunnel (ft/s)	(mph)
2	1	15	98,901	31.67	21.60
2	2	15	64,578	20.68	14.10
2	3	15	92,731	29.70	20.25
2	4	15	87,984	28.18	19.21
2	5	15	89,759	28.75	19.60
2	6	15	77,554	24.84	16.93
2	7	15	109,582	35.09	23.93
2	8	15	105,113	33.66	22.95
2	9	15	87,081	27.89	19.01
2	10	15	110,063	35.25	24.03

14.2 APPENDIX 2 -- Underwater Data for Vehicle 2 sheet 5 of 5

Vehicle 2 – 20° Wing Angle of Attack

Vehicle	Trial	Wing Angle of Attack (degrees)	Horizontal Distance (inches)	Vertical Distance (inches)	Total Distance (inches)	Time of Descent (seconds)	Velocity (ft/s)	Glide Ratio	Angle of Glide Ratio (degrees)
2	1	20	89	51	102.58	10.89	0.78	1.75	36.97
2	2	20	94	51	106.94	9.88	0.90	1.84	34.54
2	3	20	96	51	108.71	12.97	0.70	1.88	33.67
2	4	20	80	51	94.87	13.96	0.57	1.57	42.44
2	5	20	93	51	106.07	11.9	0.74	1.82	35.00
2	6	20	130	51	139.65	11.28	1.03	2.55	23.71
2	7	20	74	51	89.87	9.46	0.79	1.45	47.21
2	8	20	85	51	99.13	8.67	0.95	1.67	39.20
2	9	20	86	51	99.98	10.86	0.77	1.69	38.61
2	10	20	85	51	99.13	10.86	0.76	1.67	39.20

Vehicle	Trial	Wing Angle of Attack (degrees)	Reynolds Number	Velocity of Wind Tunnel (ft/s)	(mph)
2	1	20	72,365	23.17	0.00
2	2	20	83,158	26.63	0.68
2	3	20	64,390	20.62	1.36
2	4	20	52,211	16.72	2.05
2	5	20	68,475	21.93	2.73
2	6	20	95,110	30.46	3.41
2	7	20	72,986	23.37	4.09
2	8	20	87,836	28.13	4.77
2	9	20	70,731	22.65	5.45
2	10	20	70,123	22.46	6.14

14.3 APPENDIX 3 -- Underwater Data for Vehicle 3 sheet 1 of 5

Vehicle 3 – 0° Wing Angle of Attack

Vehicle	Trial	Wing Angle of Attack (degrees)	Horizontal Displacement (inches)	Vertical Displacement (inches)	Total Displacement (inches)	Time of Descent (seconds)	Velocity (ft/s)	Glide Ratio (ft)	Angle of Glide Ratio (degrees)
3	1	0	88.24	36	95.30	11.07	0.72	2.45	24.77
3	2	0	69.18	36	77.98	12.44	0.52	1.92	32.84
3	3	0	93.18	36	99.89	11.57	0.72	2.59	23.31
3	4	0	79.06	36	86.87	7.81	0.93	2.20	28.06
3	5	0	83.29	36	90.74	7.29	1.04	2.31	26.43
3	6	0	72.00	36	80.50	7.58	0.88	2.00	31.30
3	7	0	86.82	36	93.99	7.42	1.06	2.41	25.22
3	8	0	79.06	36	86.87	7.63	0.95	2.20	28.06
3	9	0	81.18	36	88.80	7.87	0.94	2.25	27.22
3	10	0	68.47	36	77.36	8.6	0.75	1.90	33.25

Vehicle	Trial	Wing Angle of Attack (degrees)	Reynolds Number	Velocity of Wind Tunnel (ft/s)	(mph)
3	1	0	66,135.58	21.18	14.44
3	2	0	48,159.91	15.42	10.52
3	3	0	66,326.95	21.24	14.48
3	4	0	85,451.71	27.37	18.66
3	5	0	95,626.96	30.62	20.88
3	6	0	81,587.40	26.13	17.81
3	7	0	97,316.75	31.17	21.25
3	8	0	87,467.61	28.01	19.10
3	9	0	86,685.80	27.76	18.93
3	10	0	69,105.11	22.13	15.09

14.3 APPENDIX 3 -- Underwater Data for Vehicle 3 sheet 2 of 5

Vehicle 3 – 5° Wing Angle of Attack

Vehicle	Trial	Wing Angle of Attack (degrees)	Horizontal Displacement (inches)	Vertical Displacement (inches)	Total Displacement (inches)	Time of Descent (seconds)	Velocity (ft/s)	Glide Ratio (ft)	Angle of Glide Ratio (degrees)
3	1	5	61	36	70.83	7.42	0.80	1.69	38.38
3	2	5	65	36	74.30	7.47	0.83	1.81	35.43
3	3	5	89	36	96.01	7.23	1.11	2.47	24.53
3	4	5	55	36	65.73	6	0.91	1.53	43.97
3	5	5	63	36	72.56	6.9	0.88	1.75	36.84
3	6	5	72	36	80.50	7.23	0.93	2.00	31.30
3	7	5	68	36	76.94	7.14	0.90	1.89	33.53
3	8	5	55	36	65.73	6.87	0.80	1.53	43.97
3	9	5	56	36	66.57	6.67	0.83	1.56	42.91
3	10	5	57	36	67.42	7.2	0.78	1.58	41.91

Vehicle	Trial	Wing Angle of Attack (degrees)	Reynolds Number	Velocity of Wind Tunnel (ft/s)	(mph)
3	1	5	73,336.97	23.49	16.01
3	2	5	76,417.55	24.47	16.69
3	3	5	102,014.36	32.67	22.27
3	4	5	84,167.75	26.95	18.38
3	5	5	80,789.50	25.87	17.64
3	6	5	85,537.00	27.39	18.68
3	7	5	82,788.01	26.51	18.08
3	8	5	73,508.95	23.54	16.05
3	9	5	76,679.43	24.56	16.74
3	10	5	71,934.84	23.04	15.71

14.3 APPENDIX 3 -- Underwater Data for Vehicle 3 sheet 3 of 5

Vehicle 3 – 10° Wing Angle of Attack

Vehicle	Trial	Wing Angle of Attack (degrees)	Horizontal Displacement (inches)	Vertical Displacement (inches)	Total Displacement (inches)	Time of Descent (seconds)	Velocity (ft/s)	Glide Ratio (ft)	Angle of Glide Ratio (degrees)
3	1	10	54	36	64.90	5.68	0.95	1.50	45.08
3	2	10	51	36	62.43	5.78	0.90	1.42	48.84
3	3	10	63	36	72.56	5.8	1.04	1.75	36.84
3	4	10	63	36	72.56	5.75	1.05	1.75	36.84
3	5	10	64	36	73.43	5.76	1.06	1.78	36.12
3	6	10	67	36	76.06	7.1	0.89	1.86	34.14
3	7	10	68	36	76.94	5.8	1.11	1.89	33.53
3	8	10	53	36	64.07	6.32	0.84	1.47	46.26
3	9	10	59	36	69.12	6.12	0.94	1.64	40.06
3	10	10	62	36	71.69	6.23	0.96	1.72	37.59

Vehicle	Trial	Wing Angle of Attack (degrees)	Reynolds Number	Velocity of Wind Tunnel (ft/s)	(mph)
3	1	10	87,781.03	28.11	19.17
3	2	10	82,974.03	26.57	18.12
3	3	10	96,111.64	30.78	20.99
3	4	10	96,947.40	31.05	21.17
3	5	10	97,939.36	31.36	21.39
3	6	10	82,299.68	26.36	17.97
3	7	10	101,914.90	32.64	22.25
3	8	10	77,883.29	24.94	17.01
3	9	10	86,762.29	27.79	18.94
3	10	10	88,409.38	28.31	19.30

14.3 APPENDIX 3 -- Underwater Data for Vehicle 3 sheet 4 of 5

Vehicle 3 – 15° Wing Angle of Attack

Vehicle	Trial	Wing Angle of Attack (degrees)	Horizontal Displacement (inches)	Vertical Displacement (inches)	Total Displacement (inches)	Time of Descent (seconds)	Velocity (ft/s)	Glide Ratio (ft)	Angle of Glide Ratio (degrees)
3	1	15	65	36	74.30	5.3	1.17	1.81	35.43
3	2	15	54	36	64.90	5.36	1.01	1.50	45.08
3	3	15	49	36	60.80	5.03	1.01	1.36	51.76
3	4	15	45	36	57.63	5.66	0.85	1.25	58.99
3	5	15	48	36	60.00	5.71	0.88	1.33	53.38
3	6	15	51	36	62.43	6.83	0.76	1.42	48.84
3	7	15	48	36	60.00	6.12	0.82	1.33	53.38
3	8	15	53	36	64.07	6.43	0.83	1.47	46.26
3	9	15	52	36	63.25	5.89	0.89	1.44	47.51
3	10	15	57	36	67.42	5.97	0.94	1.58	41.91

Vehicle	Trial	Wing Angle of Attack (degrees)	Reynolds Number	Velocity of Wind Tunnel (ft/s)	(mph)
3	1	15	107,705.48	34.49	23.52
3	2	15	93,021.69	29.79	20.31
3	3	15	92,867.03	29.74	20.28
3	4	15	78,220.90	25.05	17.08
3	5	15	80,727.21	25.85	17.63
3	6	15	70,218.14	22.49	15.33
3	7	15	75,319.02	24.12	16.45
3	8	15	76,550.92	24.52	16.71
3	9	15	82,493.46	26.42	18.01
3	10	15	86,755.58	27.78	18.94

14.3 APPENDIX 3 -- Underwater Data for Vehicle 3 sheet 5 of 5

Vehicle 3 – 20° Wing Angle of Attack

Vehicle	Trial	Wing Angle of Attack (degrees)	Horizontal Displacement (inches)	Vertical Displacement (inches)	Total Displacement (inches)	Time of Descent (seconds)	Velocity (ft/s)	Glide Ratio (ft)	Angle of Glide Ratio (degrees)
3	1	20	42	36	55.32	5.73	0.80	1.17	66.17
3	2	20	36	36	50.91	4.73	0.90	1.00	89.23
3	3	20	38	36	52.35	4.93	0.88	1.06	79.68
3	4	20	35	36	50.21	5.12	0.82	0.97	95.10
3	5	20	34	36	49.52	5.55	0.74	0.94	101.96
3	6	20	36	36	50.91	5.13	0.83	1.00	89.23
3	7	20	37	36	51.62	5.17	0.83	1.03	84.14
3	8	20	38	36	52.35	6.12	0.71	1.06	79.68
3	9	20	40	36	53.81	5.83	0.77	1.11	72.20
3	10	20	41	36	54.56	5.07	0.90	1.14	69.03

Vehicle	Trial	Wing Angle of Attack (degrees)	Reynolds Number	Velocity of Wind Tunnel (ft/s)	(mph)
3	1	20	74,167.03	23.75	16.19
3	2	20	82,691.56	26.48	18.06
3	3	20	81,570.51	26.12	17.81
3	4	20	75,339.25	24.13	16.45
3	5	20	68,544.41	21.95	14.97
3	6	20	76,243.87	24.42	16.65
3	7	20	76,711.92	24.57	16.75
3	8	20	65,709.58	21.04	14.35
3	9	20	70,914.58	22.71	15.48
3	10	20	82,677.30	26.48	18.05

14.4 APPENDIX 4 -- Wind Tunnel Data for Vehicle 1 sheet 1 of 5

Vehicle 1 - 0° Wing Angle of Attack

Sting AOA	Body Forces		Lift	Drag	C_L	C_D	L/D
(degrees)	N (lbs)	A (lbs)					
0.00	0.15	0.13	0.15	0.13	0.10	0.08	1.19
2.00	0.25	0.15	0.24	0.16	0.16	0.11	1.54
4.00	0.32	0.14	0.31	0.17	0.21	0.11	1.89
6.00	0.43	0.15	0.41	0.19	0.28	0.13	2.16
8.00	0.52	0.14	0.50	0.21	0.33	0.14	2.40
10.00	0.59	0.11	0.56	0.21	0.38	0.14	2.67
12.00	0.64	0.12	0.60	0.25	0.40	0.17	2.44
14.00	0.71	0.11	0.66	0.28	0.44	0.19	2.35
16.00	0.75	0.11	0.69	0.31	0.46	0.21	2.21
18.00	0.75	0.11	0.68	0.33	0.45	0.22	2.04
20.00	0.83	0.10	0.74	0.38	0.50	0.25	1.95

Indicated	Body Forces		Reynolds	C_L	C_D	L/D
Airspeed	N (lbs)	A (lbs)	Number			
(mph)						
20.00	0.18	0.01	126952	0.17	0.04	4.25
25.00	0.31	0.02	158690	0.31	0.07	4.34
30.00	0.42	0.04	190428	0.41	0.11	3.65
35.00	0.55	0.05	222166	0.53	0.15	3.59
40.00	0.68	0.07	253904	0.66	0.19	3.52
45.00	0.89	0.09	285642	0.86	0.25	3.49
50.00	1.06	0.12	317380	1.02	0.30	3.42
55.00	1.28	0.14	349118	1.24	0.36	3.47
60.00	1.46	0.16	380856	1.41	0.41	3.43
65.00	1.68	0.19	412594	1.62	0.48	3.39
70.00	1.95	0.21	444332	1.88	0.55	3.43
75.00	2.15	0.24	476070	2.08	0.61	3.39
80.00	2.37	0.27	507807	2.29	0.68	3.38

14. 4 APPENDIX 4 -- Wind Tunnel Data for Vehicle 1 sheet 2 of 5

Vehicle 1 - 5° Wing Angle of Attack

Sting AOA	Body Forces		Lift	Drag	C_L	C_D	L/D
(degrees)	N (lbs)	A (lbs)					
0.00	0.39	0.11	0.39	0.11	0.26	0.07	3.52
2.00	0.42	0.11	0.42	0.12	0.28	0.08	3.46
4.00	0.50	0.11	0.49	0.14	0.33	0.10	3.42
6.00	0.57	0.11	0.55	0.17	0.37	0.11	3.34
8.00	0.64	0.09	0.62	0.18	0.42	0.12	3.42
10.00	0.73	0.11	0.70	0.23	0.47	0.16	3.04
12.00	0.81	0.11	0.77	0.27	0.51	0.18	2.82
14.00	0.82	0.10	0.77	0.30	0.52	0.20	2.58
16.00	0.84	0.11	0.78	0.34	0.52	0.23	2.30
18.00	0.89	0.11	0.81	0.38	0.54	0.26	2.12
20.00	0.94	0.12	0.84	0.43	0.56	0.29	1.95

Indicated	Body Forces		Reynolds	C_L	C_D	L/D
Airspeed	N (lbs)	A (lbs)	Number			
(mph)						
20.00	0.03	0.03	126952	0.03	0.03	0.88
25.00	0.11	0.05	158690	0.11	0.05	2.47
30.00	0.19	0.06	190428	0.19	0.06	3.02
35.00	0.27	0.09	222166	0.27	0.09	3.04
40.00	0.34	0.11	253904	0.34	0.11	3.06
45.00	0.43	0.14	285642	0.43	0.14	2.98
50.00	0.51	0.17	317380	0.51	0.17	2.92
55.00	0.56	0.21	349118	0.56	0.21	2.70
60.00	0.63	0.24	380856	0.63	0.24	2.64
65.00	0.69	0.27	412594	0.69	0.27	2.58
70.00	0.79	0.32	444332	0.79	0.32	2.48
75.00	0.86	0.35	476070	0.86	0.35	2.47
80.00	0.95	0.39	507807	0.95	0.39	2.41

14. 4 APPENDIX 4 -- Wind Tunnel Data for Vehicle 1 sheet 3 of 5

Vehicle 1 - 10° Wing Angle of Attack

Sting AOA	Body Forces		Lift	Drag	C_L	C_D	L/D
(degrees)	N (lbs)	A (lbs)					
0.00	0.53	0.15	0.53	0.15	0.36	0.10	3.64
2.00	0.62	0.16	0.61	0.18	0.41	0.12	3.32
4.00	0.69	0.17	0.68	0.21	0.45	0.14	3.17
6.00	0.79	0.18	0.77	0.26	0.51	0.17	2.93
8.00	0.86	0.18	0.83	0.30	0.55	0.20	2.77
10.00	0.88	0.20	0.83	0.35	0.56	0.23	2.40
12.00	0.86	0.20	0.80	0.37	0.53	0.25	2.14
14.00	0.89	0.21	0.81	0.42	0.54	0.28	1.92
16.00	0.97	0.22	0.87	0.48	0.58	0.32	1.80
18.00	0.96	0.23	0.85	0.52	0.56	0.35	1.64
20.00	0.88	0.24	0.75	0.52	0.50	0.35	1.43

Indicated	Body Forces		Reynolds	C_L	C_D	L/D
Airspeed	N (lbs)	A (lbs)	Number			
(mph)						
20.00	0.06	0.03	126952	0.06	0.03	2.11
25.00	0.13	0.05	158690	0.13	0.05	2.39
30.00	0.21	0.08	190428	0.21	0.08	2.52
35.00	0.34	0.12	222166	0.34	0.12	2.89
40.00	0.44	0.14	253904	0.44	0.14	3.20
45.00	0.58	0.18	285642	0.58	0.18	3.16
50.00	0.75	0.23	317380	0.75	0.23	3.29
55.00	0.95	0.28	349118	0.95	0.28	3.42
60.00	1.09	0.32	380856	1.09	0.32	3.45
65.00	1.23	0.37	412594	1.23	0.37	3.35
70.00	1.38	0.42	444332	1.38	0.42	3.29
75.00	1.57	0.48	476070	1.57	0.48	3.30
80.00	1.78	0.55	507807	1.78	0.55	3.24

14. 4 APPENDIX 4 -- Wind Tunnel Data for Vehicle 1 sheet 4 of 5

Vehicle 1 - 15° Wing Angle of Attack

Sting AOA	Body Forces		Lift	Drag	C_L	C_D	L/D
(degrees)	N (lbs)	A (lbs)					
0.00	0.55	0.23	0.55	0.23	0.37	0.15	2.43
2.00	0.62	0.23	0.61	0.25	0.41	0.17	2.45
4.00	0.71	0.24	0.69	0.29	0.46	0.19	2.42
6.00	0.74	0.25	0.71	0.33	0.47	0.22	2.17
8.00	0.85	0.26	0.81	0.38	0.54	0.25	2.14
10.00	0.94	0.28	0.88	0.44	0.59	0.29	2.00
12.00	1.07	0.29	0.99	0.50	0.66	0.34	1.97
14.00	1.12	0.29	1.02	0.56	0.68	0.37	1.83
16.00	1.11	0.30	0.99	0.60	0.66	0.40	1.65
18.00	1.07	0.32	0.92	0.64	0.62	0.43	1.45
20.00	1.08	0.31	0.91	0.66	0.61	0.44	1.38

Indicated	Body Forces		Reynolds	C_L	C_D	L/D
Airspeed	N (lbs)	A (lbs)	Number			
(mph)						
20.00	0.16	0.08	126952	0.16	0.08	2.10
25.00	0.28	0.12	158690	0.28	0.12	2.43
30.00	0.45	0.18	190428	0.45	0.18	2.55
35.00	0.54	0.21	222166	0.54	0.21	2.56
40.00	0.75	0.28	253904	0.75	0.28	2.70
45.00	0.95	0.35	285642	0.95	0.35	2.74
50.00	1.07	0.38	317380	1.07	0.38	2.82
55.00	1.29	0.44	349118	1.29	0.44	2.90
60.00	1.59	0.54	380856	1.59	0.54	2.97
65.00	1.85	0.62	412594	1.85	0.62	2.97
70.00	2.03	0.69	444332	2.03	0.69	2.95
75.00	2.36	0.80	476070	2.36	0.80	2.96
80.00	2.67	0.89	507807	2.67	0.89	2.99

14. 4 APPENDIX 4 -- Wind Tunnel Data for Vehicle 1 sheet 5 of 5

Vehicle 1 - 20° Wing Angle of Attack

Sting AOA	Body Forces		Lift	Drag	C_L	C_D	L/D
(degrees)	N (lbs)	A (lbs)					
0.00	0.74	0.30	0.74	0.30	0.49	0.20	2.44
2.00	0.80	0.31	0.79	0.33	0.53	0.22	2.35
4.00	0.80	0.32	0.77	0.37	0.52	0.25	2.08
6.00	0.85	0.33	0.81	0.42	0.54	0.28	1.93
8.00	0.95	0.35	0.89	0.48	0.60	0.32	1.86
10.00	1.02	0.36	0.94	0.54	0.63	0.36	1.76
12.00	1.05	0.37	0.95	0.58	0.63	0.39	1.64
14.00	1.09	0.37	0.96	0.62	0.65	0.42	1.55
16.00	1.09	0.37	0.94	0.66	0.63	0.44	1.43
18.00	1.11	0.38	0.93	0.71	0.62	0.47	1.32
20.00	1.10	0.38	0.90	0.73	0.60	0.49	1.23

Indicated	Body Forces		Reynolds	C_L	C_D	L/D
Airspeed	N (lbs)	A (lbs)	Number			
(mph)						
20.00	0.25	0.11	126952	0.25	0.11	2.30
25.00	0.42	0.18	158690	0.42	0.18	2.33
30.00	0.60	0.25	190428	0.60	0.25	2.42
35.00	0.77	0.31	222166	0.77	0.31	2.45
40.00	0.91	0.39	253904	0.91	0.39	2.33
45.00	1.18	0.50	285642	1.18	0.50	2.37
50.00	1.35	0.57	317380	1.35	0.57	2.38
55.00	1.63	0.67	349118	1.63	0.67	2.42
60.00	2.02	0.82	380856	2.02	0.82	2.48
65.00	2.36	0.94	412594	2.36	0.94	2.51
70.00	2.69	1.06	444332	2.69	1.06	2.53
75.00	3.08	1.21	476070	3.08	1.21	2.55
80.00	3.51	1.33	507807	3.51	1.33	2.63

14.5 APPENDIX 5 -- Wind Tunnel Data for Vehicle 2 sheet 1 of 5

Vehicle 2 - 0° Wing Angle of Attack

Sting AOA	Body Forces		Lift	Drag	C_L	C_D	L/D
(degrees)	N (lbs)	A (lbs)					
0.00	0.25	0.12	0.25	0.12	0.17	0.08	2.08
2.00	0.45	0.09	0.45	0.11	0.30	0.07	4.15
4.00	0.69	0.05	0.68	0.10	0.46	0.07	7.04
6.00	0.87	0.02	0.86	0.11	0.58	0.07	7.79
8.00	1.05	-0.01	1.04	0.14	0.69	0.09	7.47
10.00	1.37	-0.11	1.37	0.13	0.92	0.09	10.28
12.00	1.48	-0.16	1.48	0.15	0.99	0.10	10.03
14.00	1.45	-0.14	1.44	0.21	0.96	0.14	6.82
16.00	1.30	-0.05	1.26	0.31	0.84	0.21	4.03
18.00	1.23	-0.03	1.18	0.35	0.79	0.24	3.35
20.00	1.22	0.01	1.14	0.42	0.76	0.28	2.70

Indicated	Body Forces		Reynolds	C_L	C_D	L/D
Airspeed	N (lbs)	A (lbs)	Number			
(mph)						
20.00	0.04	0.03	126952	0.04	0.03	1.33
25.00	0.06	0.04	158690	0.06	0.04	1.50
30.00	0.11	0.06	190428	0.11	0.06	1.83
35.00	0.16	0.10	222166	0.16	0.10	1.60
40.00	0.20	0.12	253904	0.20	0.12	1.67
45.00	0.32	0.16	285642	0.32	0.16	2.00
50.00	0.43	0.20	317380	0.43	0.20	2.17
55.00	0.50	0.24	349118	0.50	0.24	2.10
60.00	0.59	0.27	380856	0.59	0.27	2.17
65.00	0.75	0.32	412594	0.75	0.32	2.33
70.00	0.89	0.36	444332	0.89	0.36	2.51
75.00	1.10	0.42	476070	1.10	0.42	2.61
80.00	1.32	0.46	507807	1.32	0.46	2.87

14.5 APPENDIX 5 -- Wind Tunnel Data for Vehicle 2 sheet 2 of 5

Vehicle 2 - 5° Wing Angle of Attack

Sting AOA	Body Forces		Lift	Drag	C_L	C_D	L/D
(degrees)	N (lbs)	A (lbs)					
0.00	0.89	0.15	0.89	0.15	0.59	0.10	5.91
2.00	1.01	0.13	1.00	0.17	0.67	0.11	5.97
4.00	1.43	0.07	1.42	0.17	0.95	0.12	8.23
6.00	1.56	0.03	1.55	0.19	1.04	0.13	8.04
8.00	1.65	-0.01	1.63	0.22	1.09	0.15	7.33
10.00	1.43	0.08	1.39	0.33	0.93	0.22	4.22
12.00	1.29	0.10	1.24	0.37	0.83	0.25	3.36
14.00	1.32	0.13	1.25	0.44	0.83	0.30	2.80
16.00	1.35	0.13	1.26	0.50	0.84	0.33	2.53
18.00	1.31	0.16	1.20	0.55	0.80	0.37	2.16
20.00	1.33	0.15	1.20	0.59	0.80	0.40	2.03

Indicated	Body Forces		Reynolds	C_L	C_D	L/D
Airspeed	N (lbs)	A (lbs)	Number			
(mph)						
20.00	0.18	0.03	126952	0.18	0.03	6.00
25.00	0.28	0.06	158690	0.28	0.06	4.72
30.00	0.40	0.08	190428	0.40	0.08	5.29
35.00	0.55	0.10	222166	0.55	0.10	5.50
40.00	0.79	0.14	253904	0.79	0.14	5.62
45.00	0.98	0.19	285642	0.98	0.19	5.18
50.00	1.24	0.24	317380	1.24	0.24	5.17
55.00	1.62	0.29	349118	1.62	0.29	5.59
60.00	1.85	0.33	380856	1.85	0.33	5.61
65.00	2.43	0.39	412594	2.43	0.39	6.23
70.00	2.87	0.44	444332	2.87	0.44	6.52
75.00	3.82	0.47	476070	3.82	0.47	8.19
80.00	4.86	0.51	507807	4.86	0.51	9.47

14.5 APPENDIX 5 -- Wind Tunnel Data for Vehicle 2 sheet 3 of 5

Vehicle 2 - 10° Wing Angle of Attack

Sting AOA	Body Forces		Lift	Drag	C_L	C_D	L/D
(degrees)	N (lbs)	A (lbs)					
0.00	0.85	0.16	0.85	0.16	0.57	0.10	5.43
2.00	1.13	0.13	1.12	0.17	0.75	0.12	6.52
4.00	1.29	0.08	1.28	0.17	0.86	0.11	7.70
6.00	1.31	0.05	1.30	0.19	0.87	0.13	6.84
8.00	1.22	0.10	1.19	0.27	0.80	0.18	4.50
10.00	1.08	0.16	1.04	0.34	0.70	0.23	3.04
12.00	0.98	0.17	0.92	0.37	0.62	0.25	2.49
14.00	0.96	0.18	0.89	0.41	0.60	0.27	2.17
16.00	0.93	0.18	0.85	0.43	0.57	0.29	1.95
18.00	0.96	0.18	0.86	0.47	0.57	0.31	1.82
20.00	0.99	0.19	0.87	0.52	0.58	0.35	1.67

Indicated	Body Forces		Reynolds	C_L	C_D	L/D
Airspeed	N (lbs)	A (lbs)	Number			
(mph)						
20.00	0.24	0.06	126952	0.24	0.06	4.31
25.00	0.31	0.07	158690	0.31	0.07	4.29
30.00	0.46	0.10	190428	0.46	0.10	4.49
35.00	0.64	0.15	222166	0.64	0.15	4.24
40.00	0.82	0.17	253904	0.82	0.17	4.73
45.00	1.12	0.22	285642	1.12	0.22	5.02
50.00	1.50	0.27	317380	1.50	0.27	5.48
55.00	1.89	0.31	349118	1.89	0.31	6.03
60.00	2.34	0.35	380856	2.34	0.35	6.70
65.00	3.27	0.38	412594	3.27	0.38	8.52
70.00	3.92	0.43	444332	3.92	0.43	9.11
75.00	4.60	0.48	476070	4.60	0.48	9.53
80.00	5.32	0.55	507807	5.32	0.55	9.62

14.5 APPENDIX 5 -- Wind Tunnel Data for Vehicle 2 sheet 4 of 5

Vehicle 2 - 15° Wing Angle of Attack

Sting AOA	Body Forces		Lift	Drag	C_L	C_D	L/D
(degrees)	N (lbs)	A (lbs)					
0.00	1.36	0.20	1.36	0.20	0.91	0.13	6.80
2.00	1.15	0.26	1.14	0.30	0.76	0.20	3.85
4.00	1.09	0.27	1.07	0.35	0.71	0.23	3.09
6.00	1.08	0.28	1.05	0.39	0.70	0.26	2.68
8.00	1.07	0.28	1.02	0.42	0.68	0.28	2.41
10.00	1.10	0.28	1.04	0.46	0.69	0.31	2.23
12.00	1.06	0.28	0.98	0.49	0.65	0.33	1.99
14.00	1.05	0.29	0.95	0.53	0.63	0.36	1.78
16.00	1.06	0.29	0.94	0.57	0.63	0.38	1.63
18.00	1.10	0.30	0.96	0.62	0.64	0.42	1.54
20.00	1.12	0.30	0.95	0.66	0.63	0.44	1.43

Indicated	Body Forces		Reynolds	C_L	C_D	L/D
Airspeed	N (lbs)	A (lbs)	Number			
(mph)						
20.00	0.37	0.05	126952	0.37	0.05	6.98
25.00	0.54	0.08	158690	0.54	0.08	6.71
30.00	0.76	0.11	190428	0.76	0.11	6.72
35.00	1.13	0.17	222166	1.13	0.17	6.76
40.00	1.38	0.21	253904	1.38	0.21	6.70
45.00	1.83	0.28	285642	1.83	0.28	6.60
50.00	2.23	0.34	317380	2.23	0.34	6.55
55.00	2.70	0.42	349118	2.70	0.42	6.42
60.00	3.16	0.49	380856	3.16	0.49	6.49
65.00	3.72	0.58	412594	3.72	0.58	6.45
70.00	4.26	0.66	444332	4.26	0.66	6.46
75.00	4.96	0.75	476070	4.96	0.75	6.58
80.00	5.63	0.86	507807	5.63	0.86	6.53

14.5 APPENDIX 5 -- Wind Tunnel Data for Vehicle 2 sheet 5 of 5

Vehicle 2 - 20° Wing Angle of Attack

Sting AOA	Body Forces		Lift	Drag	C_L	C_D	L/D
(degrees)	N (lbs)	A (lbs)					
0.00	1.05	0.41	1.05	0.41	0.70	0.27	2.58
2.00	1.03	0.38	1.02	0.41	0.68	0.28	2.47
4.00	1.04	0.38	1.01	0.45	0.68	0.30	2.25
6.00	1.06	0.38	1.01	0.49	0.68	0.33	2.06
8.00	1.06	0.39	1.00	0.53	0.67	0.35	1.88
10.00	1.05	0.39	0.96	0.57	0.64	0.38	1.70
12.00	1.06	0.41	0.95	0.62	0.64	0.42	1.53
14.00	1.06	0.40	0.93	0.65	0.62	0.43	1.44
16.00	1.09	0.40	0.94	0.69	0.63	0.46	1.36
18.00	1.11	0.41	0.93	0.74	0.62	0.49	1.26
20.00	1.13	0.42	0.92	0.78	0.61	0.52	1.18

Indicated	Body Forces		Reynolds	C_L	C_D	L/D
Airspeed	N (lbs)	A (lbs)	Number			
(mph)						
20.00	0.22	0.10	126952	0.22	0.10	2.20
25.00	0.39	0.17	158690	0.39	0.17	2.36
30.00	0.63	0.25	190428	0.63	0.25	2.51
35.00	0.82	0.32	222166	0.82	0.32	2.60
40.00	1.00	0.38	253904	1.00	0.38	2.62
45.00	1.38	0.53	285642	1.38	0.53	2.61
50.00	1.73	0.66	317380	1.73	0.66	2.61
55.00	2.16	0.81	349118	2.16	0.81	2.68
60.00	2.55	0.95	380856	2.55	0.95	2.68
65.00	3.24	1.15	412594	3.24	1.15	2.81
70.00	3.95	1.44	444332	3.95	1.44	2.74
75.00	4.76	1.70	476070	4.76	1.70	2.80
80.00	5.44	1.93	507807	5.44	1.93	2.81

14.6 APPENDIX 6 -- Wind Tunnel Data for Vehicle 3 sheet 1 of 5

Vehicle 3 - 0° Wing Angle of Attack

Sting AOA	Body Forces		Lift	Drag	C_L	C_D	L/D
(degrees)	N (lbs)	A (lbs)					
0.00	0.81	0.17	0.81	0.17	0.54	0.11	4.76
2.00	0.93	0.14	0.92	0.17	0.62	0.12	5.30
4.00	1.07	0.13	1.06	0.20	0.71	0.14	5.19
6.00	1.39	0.08	1.37	0.23	0.92	0.15	6.03
8.00	1.66	0.01	1.64	0.24	1.10	0.16	6.73
10.00	1.73	-0.01	1.71	0.29	1.14	0.19	5.87
12.00	1.75	-0.03	1.72	0.34	1.15	0.23	5.09
14.00	1.59	0.11	1.52	0.49	1.01	0.33	3.06
16.00	1.52	0.13	1.43	0.54	0.95	0.36	2.62
18.00	1.50	0.15	1.38	0.61	0.92	0.41	2.28
20.00	1.50	0.16	1.35	0.66	0.91	0.44	2.04

Indicated	Body Forces		Reynolds	C_L	C_D	L/D
Airspeed	N (lbs)	A (lbs)	Number			
(mph)						
20.00	0.18	0.05	126952	0.18	0.05	3.82
25.00	0.33	0.08	158690	0.33	0.08	4.13
30.00	0.41	0.11	190428	0.41	0.11	3.88
35.00	0.53	0.14	222166	0.53	0.14	3.88
40.00	0.72	0.17	253904	0.72	0.17	4.22
45.00	0.89	0.23	285642	0.89	0.23	3.91
50.00	1.10	0.28	317380	1.10	0.28	3.94
55.00	1.31	0.33	349118	1.31	0.33	3.98
60.00	1.58	0.39	380856	1.58	0.39	4.08
65.00	1.86	0.46	412594	1.86	0.46	4.08
70.00	2.16	0.52	444332	2.16	0.52	4.17
75.00	2.59	0.59	476070	2.59	0.59	4.39
80.00	3.07	0.65	507807	3.07	0.65	4.75

14.6 APPENDIX 6 -- Wind Tunnel Data for Vehicle 3 sheet 2 of 5

Vehicle 3 - 5° Wing Angle of Attack

Sting AOA	Body Forces		Lift	Drag	C_L	C_D	L/D
(degrees)	N (lbs)	A (lbs)					
0.00	0.91	0.18	0.91	0.18	0.61	0.12	4.95
2.00	1.02	0.17	1.02	0.21	0.68	0.14	4.87
4.00	1.23	0.15	1.22	0.24	0.81	0.16	5.17
6.00	1.55	0.07	1.53	0.23	1.03	0.15	6.62
8.00	1.62	0.04	1.60	0.26	1.07	0.18	6.11
10.00	1.63	0.02	1.60	0.31	1.07	0.20	5.23
12.00	1.43	0.14	1.37	0.43	0.92	0.29	3.18
14.00	1.35	0.18	1.27	0.50	0.85	0.33	2.54
16.00	1.35	0.18	1.25	0.55	0.84	0.37	2.29
18.00	1.31	0.19	1.19	0.58	0.80	0.39	2.04
20.00	1.28	0.19	1.14	0.62	0.76	0.41	1.84

Indicated	Body Forces		Reynolds	C_L	C_D	L/D
Airspeed	N (lbs)	A (lbs)	Number			
(mph)						
20.00	0.26	0.06	126952	0.26	0.06	4.62
25.00	0.35	0.08	158690	0.35	0.08	4.63
30.00	0.48	0.10	190428	0.48	0.10	4.87
35.00	0.70	0.15	222166	0.70	0.15	4.75
40.00	0.88	0.18	253904	0.88	0.18	4.90
45.00	1.09	0.24	285642	1.09	0.24	4.62
50.00	1.41	0.31	317380	1.41	0.31	4.61
55.00	1.66	0.37	349118	1.66	0.37	4.54
60.00	1.95	0.42	380856	1.95	0.42	4.61
65.00	2.40	0.51	412594	2.40	0.51	4.73
70.00	2.88	0.57	444332	2.88	0.57	5.02
75.00	3.56	0.64	476070	3.56	0.64	5.56
80.00	4.26	0.68	507807	4.26	0.68	6.30

14.6 APPENDIX 6 -- Wind Tunnel Data for Vehicle 3 sheet 3 of 5

Vehicle 3 - 10° Wing Angle of Attack

Sting AOA	Body Forces		Lift	Drag	C_L	C_D	L/D
(degrees)	N (lbs)	A (lbs)					
0.00	1.09	0.20	1.09	0.20	0.73	0.13	5.43
2.00	1.47	0.15	1.46	0.20	0.98	0.14	7.15
4.00	1.59	0.13	1.58	0.24	1.05	0.16	6.65
6.00	1.65	0.09	1.63	0.26	1.09	0.17	6.22
8.00	1.63	0.10	1.60	0.33	1.07	0.22	4.91
10.00	1.42	0.21	1.36	0.45	0.91	0.30	3.00
12.00	1.35	0.23	1.28	0.51	0.85	0.34	2.50
14.00	1.36	0.24	1.26	0.56	0.84	0.38	2.24
16.00	1.30	0.24	1.18	0.59	0.79	0.40	1.99
18.00	1.28	0.25	1.14	0.63	0.76	0.42	1.80
20.00	1.27	0.26	1.11	0.68	0.74	0.45	1.64

Indicated	Body Forces		Reynolds	C_L	C_D	L/D
Airspeed	N (lbs)	A (lbs)	Number			
(mph)						
20.00	0.27	0.05	126952	0.27	0.05	5.87
25.00	0.39	0.07	158690	0.39	0.07	5.57
30.00	0.58	0.11	190428	0.58	0.11	5.24
35.00	0.85	0.16	222166	0.85	0.16	5.21
40.00	1.04	0.20	253904	1.04	0.20	5.27
45.00	1.36	0.25	285642	1.36	0.25	5.37
50.00	1.75	0.31	317380	1.75	0.31	5.63
55.00	2.20	0.37	349118	2.20	0.37	6.00
60.00	3.13	0.40	380856	3.13	0.40	7.83
65.00	3.87	0.48	412594	3.87	0.48	8.11
70.00	4.46	0.55	444332	4.46	0.55	8.12
75.00	5.22	0.64	476070	5.22	0.64	8.11
80.00	5.79	0.72	507807	5.79	0.72	8.08

14.6 APPENDIX 6 -- Wind Tunnel Data for Vehicle 3 sheet 4 of 5

Vehicle 3 - 15° Wing Angle of Attack

Sting AOA	Body Forces		Lift	Drag	C_L	C_D	L/D
(degrees)	N (lbs)	A (lbs)					
0.00	1.57	0.20	1.57	0.20	1.05	0.14	7.74
2.00	1.61	0.16	1.60	0.21	1.07	0.14	7.53
4.00	1.63	0.14	1.62	0.25	1.08	0.17	6.48
6.00	1.50	0.19	1.47	0.34	0.98	0.23	4.30
8.00	1.33	0.25	1.28	0.44	0.85	0.29	2.94
10.00	1.31	0.26	1.25	0.48	0.83	0.32	2.58
12.00	1.25	0.28	1.17	0.53	0.78	0.36	2.20
14.00	1.29	0.29	1.19	0.59	0.79	0.40	2.01
16.00	1.28	0.29	1.15	0.64	0.77	0.43	1.81
18.00	1.22	0.31	1.06	0.67	0.71	0.45	1.58
20.00	1.20	0.32	1.02	0.71	0.68	0.48	1.43

Indicated	Body Forces		Reynolds	C_L	C_D	L/D
Airspeed	N (lbs)	A (lbs)	Number			
(mph)						
20.00	0.31	0.05	126952	0.31	0.05	5.84
25.00	0.43	0.08	158690	0.43	0.08	5.63
30.00	0.81	0.10	190428	0.81	0.10	7.85
35.00	1.15	0.14	222166	1.15	0.14	8.06
40.00	1.49	0.19	253904	1.49	0.19	7.99
45.00	1.86	0.24	285642	1.86	0.24	7.76
50.00	2.36	0.31	317380	2.36	0.31	7.55
55.00	2.84	0.38	349118	2.84	0.38	7.47
60.00	3.35	0.45	380856	3.35	0.45	7.50
65.00	3.93	0.53	412594	3.93	0.53	7.47
70.00	4.47	0.60	444332	4.47	0.60	7.46
75.00	5.15	0.70	476070	5.15	0.70	7.39
80.00	5.95	0.81	507807	5.95	0.81	7.37

14.6 APPENDIX 6 -- Wind Tunnel Data for Vehicle 3 sheet 5 of 5

Vehicle 3 - 20° Wing Angle of Attack

Sting AOA	Body Forces		Lift	Drag	C_L	C_D	L/D
(degrees)	N (lbs)	A (lbs)					
0.00	1.19	0.45	1.19	0.46	0.79	0.31	2.59
2.00	1.13	0.45	1.11	0.51	0.74	0.34	2.19
4.00	1.13	0.46	1.09	0.55	0.73	0.37	1.98
6.00	1.11	0.47	1.04	0.60	0.70	0.40	1.75
8.00	1.11	0.49	1.03	0.65	0.69	0.44	1.58
10.00	1.09	0.50	0.98	0.69	0.65	0.46	1.41
12.00	1.07	0.52	0.93	0.74	0.62	0.50	1.26
14.00	1.03	0.53	0.86	0.78	0.57	0.52	1.11
16.00	1.02	0.54	0.82	0.81	0.55	0.54	1.01
18.00	1.02	0.56	0.78	0.85	0.52	0.57	0.92
20.00	1.03	0.56	0.78	0.88	0.52	0.59	0.88

Indicated	Body Forces		Reynolds	C_L	C_D	L/D
Airspeed	N (lbs)	A (lbs)	Number			
(mph)						
20.00	0.44	0.14	148111	0.44	0.14	3.10
25.00	0.69	0.24	179848	0.69	0.24	2.84
30.00	0.91	0.34	211586	0.91	0.34	2.67
35.00	1.15	0.43	243324	1.15	0.43	2.67
40.00	1.42	0.54	275062	1.42	0.54	2.62
45.00	1.78	0.68	306800	1.78	0.68	2.61
50.00	2.13	0.85	338538	2.13	0.85	2.50
55.00	2.64	1.03	370276	2.64	1.03	2.56
60.00	3.47	1.29	402014	3.47	1.29	2.69
65.00	4.03	1.53	433752	4.03	1.53	2.64
70.00	4.72	1.75	465490	4.72	1.75	2.69
75.00	5.80	2.12	497228	5.80	2.12	2.73
80.00	6.12	2.25	507807	6.12	2.25	2.72

14.7 APPENDIX 7 -- Flow rates of recirculation tank sheet 1 of 5

Grid	Static Tube		Pitot Tube		Velocity of Flow	
Coordinate	Height	Pressure	Height	Pressure	(m/s)	(ft/s)
	(mm)	(kN/m^2)	(mm)	(kN/m^2)		
A 0	1.0	9.6	2.0	19.2	0.1	0.5
A 1	1.0	9.6	2.0	19.2	0.1	0.5
A 2	1.0	9.6	3.0	28.8	0.2	0.6
A 3	1.0	9.6	3.0	28.8	0.2	0.6
A 4	1.0	9.6	4.0	38.4	0.2	0.8
A 5	1.0	9.6	4.0	38.4	0.2	0.8
A 6	1.0	9.6	3.0	28.8	0.2	0.6
A 7	1.0	9.6	3.0	28.8	0.2	0.6
A 8	1.0	9.6	2.0	19.2	0.1	0.5
A 9	1.0	9.6	4.0	38.4	0.2	0.8
A 10	1.0	9.6	4.0	38.4	0.2	0.8
A 11	1.0	9.6	4.0	38.4	0.2	0.8
A 12	1.0	9.6	3.0	28.8	0.2	0.6
A 13	1.0	9.6	4.0	38.4	0.2	0.8
A 14	1.0	9.6	2.0	19.2	0.1	0.5
A 15	1.0	9.6	3.0	28.8	0.2	0.6
A 16	1.0	9.6	4.0	38.4	0.2	0.8
A 17	1.0	9.6	4.0	38.4	0.2	0.8
A 18	1.0	9.6	2.0	19.2	0.1	0.5
A 19	1.0	9.6	3.0	28.8	0.2	0.6
A 20	1.0	9.6	3.0	28.8	0.2	0.6
A 21	1.0	9.6	4.0	38.4	0.2	0.8
A 22	1.0	9.6	3.0	28.8	0.2	0.6

14.7 APPENDIX 7 -- Flow rates of recirculation tank sheet 2 of 5

Grid	Static Tube		Pitot Tube		Velocity of Flow	
Coordinate	Height	Pressure	Height	Pressure	(m/s)	(ft/s)
	(mm)	(kN/m^2)	(mm)	(kN/m^2)		
B 0	1.0	9.6	3.0	28.8	0.2	0.6
B 1	1.0	9.6	3.0	28.8	0.2	0.6
B 2	1.0	9.6	3.0	28.8	0.2	0.6
B 3	1.0	9.6	3.0	28.8	0.2	0.6
B 4	1.0	9.6	3.0	28.8	0.2	0.6
B 5	1.0	9.6	4.0	38.4	0.2	0.8
B 6	1.0	9.6	3.0	28.8	0.2	0.6
B 7	1.0	9.6	4.0	38.4	0.2	0.8
B 8	1.0	9.6	3.0	28.8	0.2	0.6
B 9	1.0	9.6	4.0	38.4	0.2	0.8
B 10	1.0	9.6	3.0	28.8	0.2	0.6
B 11	1.0	9.6	4.0	38.4	0.2	0.8
B 12	1.0	9.6	3.0	28.8	0.2	0.6
B 13	1.0	9.6	4.0	38.4	0.2	0.8
B 14	1.0	9.6	3.0	28.8	0.2	0.6
B 15	1.0	9.6	4.0	38.4	0.2	0.8
B 16	1.0	9.6	3.0	28.8	0.2	0.6
B 17	1.0	9.6	4.0	38.4	0.2	0.8
B 18	1.0	9.6	3.0	28.8	0.2	0.6
B 19	1.0	9.6	4.0	38.4	0.2	0.8
B 20	1.0	9.6	3.0	28.8	0.2	0.6
B 21	1.0	9.6	4.0	38.4	0.2	0.8
B 22	1.0	9.6	3.0	28.8	0.2	0.6

14.7 APPENDIX 7 -- Flow rates of recirculation tank sheet 3 of 5

Grid	Static Tube		Pitot Tube		Velocity of Flow	
Coordinate	Height	Pressure	Height	Pressure	(m/s)	(ft/s)
	(mm)	(kN/m^2)	(mm)	(kN/m^2)		
C 0	2.0	19.2	3.0	28.8	0.1	0.5
C 1	2.0	19.2	3.0	28.8	0.1	0.5
C 2	1.0	9.6	4.0	38.4	0.2	0.8
C 3	1.0	9.6	6.0	57.5	0.3	1.0
C 4	1.0	9.6	6.0	57.5	0.3	1.0
C 5	2.0	19.2	5.0	47.9	0.2	0.8
C 6	1.0	9.6	3.0	28.8	0.2	0.6
C 7	1.0	9.6	4.0	38.4	0.2	0.8
C 8	2.0	19.2	3.0	28.8	0.1	0.5
C 9	3.0	28.8	7.0	67.1	0.3	0.9
C 10	1.0	9.6	6.0	57.5	0.3	1.0
C 11	1.0	9.6	5.0	47.9	0.3	0.9
C 12	2.0	19.2	6.0	57.5	0.3	0.9
C 13	2.0	19.2	4.0	38.4	0.2	0.6
C 14	1.0	9.6	4.0	38.4	0.2	0.8
C 15	1.0	9.6	4.0	38.4	0.2	0.8
C 16	2.0	19.2	5.0	47.9	0.2	0.8
C 17	1.0	9.6	4.0	38.4	0.2	0.8
C 18	1.0	9.6	4.0	38.4	0.2	0.8
C 19	1.0	9.6	4.0	38.4	0.2	0.8
C 20	1.0	9.6	4.0	38.4	0.2	0.8
C 21	1.0	9.6	4.0	38.4	0.2	0.8
C 22	1.0	9.6	4.0	38.4	0.2	0.8

14.7 APPENDIX 7 – Flow rates of recirculation tank sheet 4 of 5

Grid	Static Tube		Pitot Tube		Velocity of Flow	
Coordinate	Height	Pressure	Height	Pressure	(m/s)	(ft/s)
	(mm)	(kN/m^2)	(mm)	(kN/m^2)		
D 0	4.0	38.4	4.0	38.4	0.0	0.0
D 1	4.0	38.4	4.0	38.4	0.0	0.0
D 2	2.0	19.2	3.0	28.8	0.1	0.5
D 3	3.0	28.8	11.0	105.5	0.4	1.3
D 4	4.0	38.4	8.0	76.7	0.3	0.9
D 5	4.0	38.4	7.0	67.1	0.2	0.8
D 6	3.0	28.8	6.0	57.5	0.2	0.8
D 7	2.0	19.2	5.0	47.9	0.2	0.8
D 8	3.0	28.8	8.0	76.7	0.3	1.0
D 9	3.0	28.8	11.0	105.5	0.4	1.3
D 10	3.0	28.8	7.0	67.1	0.3	0.9
D 11	4.0	38.4	6.0	57.5	0.2	0.6
D 12	4.0	38.4	7.0	67.1	0.2	0.8
D 13	4.0	38.4	8.0	76.7	0.3	0.9
D 14	3.0	28.8	11.0	105.5	0.4	1.3
D 15	3.0	28.8	7.0	67.1	0.3	0.9
D 16	2.0	19.2	12.0	115.1	0.4	1.5
D 17	2.0	19.2	7.0	67.1	0.3	1.0
D 18	2.0	19.2	5.0	47.9	0.2	0.8
D 19	3.0	28.8	6.0	57.5	0.2	0.8
D 20	2.0	19.2	11.0	105.5	0.4	1.4
D 21	2.0	19.2	11.0	105.5	0.4	1.4
D 22	3.0	28.8	6.0	57.5	0.2	0.8

14.7 APPENDIX 7 – Flow rates of recirculation tank sheet 5 of 5

Grid	Static Tube		Pitot Tube		Velocity of Flow	
Coordinate	Height	Pressure	Height	Pressure	(m/s)	(ft/s)
	(mm)	(kN/m^2)	(mm)	(kN/m^2)		
E0	2.0	19.2	4.0	38.4	0.2	0.6
E 1	2.0	19.2	4.0	38.4	0.2	0.6
E 2	2.0	19.2	3.0	28.8	0.1	0.5
E 3	3.0	28.8	5.0	47.9	0.2	0.6
E 4	1.0	9.6	4.0	38.4	0.2	0.8
E 5	2.0	19.2	4.0	38.4	0.2	0.6
E 6	2.0	19.2	4.0	38.4	0.2	0.6
E 7	1.0	9.6	3.0	28.8	0.2	0.6
E 8	2.0	19.2	2.0	19.2	0.0	0.0
E 9	2.0	19.2	3.0	28.8	0.1	0.5
E 10	2.0	19.2	5.0	47.9	0.2	0.8
E 11	2.0	19.2	4.0	38.4	0.2	0.6
E 12	3.0	28.8	6.0	57.5	0.2	0.8
E 13	2.0	19.2	3.0	28.8	0.1	0.5
E 14	2.0	19.2	3.0	28.8	0.1	0.5
E 15	3.0	28.8	4.0	38.4	0.1	0.5
E 16	2.0	19.2	4.0	38.4	0.2	0.6
E 17	2.0	19.2	3.0	28.8	0.1	0.5
E 18	2.0	19.2	2.0	19.2	0.0	0.0
E 19	3.0	28.8	5.0	47.9	0.2	0.6
E 20	2.0	19.2	5.0	47.9	0.2	0.8
E 21	2.0	19.2	4.0	38.4	0.2	0.6
E 22	3.0	28.8	6.0	57.5	0.2	0.8

14.8 APPENDIX 8 -- UniForce Sensor Calibration

Axial Force Sensor	
Weight	Resistance
(lbs)	(kohms)
0.05	1550
0.10	1030
0.15	830
0.20	760
0.25	630
0.30	540
0.35	440
0.40	384
0.45	312
0.50	285
0.55	281
0.60	228
0.65	201
0.70	177
0.75	159
0.80	148
0.85	141
0.90	134
0.95	124
1.00	119
1.05	111
1.10	105
1.15	94
1.20	88
1.25	88
1.30	87
1.35	83
1.40	77
1.45	74
1.50	68
1.55	65
1.60	63
1.65	61
1.70	60
1.75	59
1.80	58
1.85	58
1.90	58
1.95	56
2.00	53

Normal Force Sensor	
Weight	Resistance
(lbs)	(kohms)
0.05	1950
0.10	1820
0.15	1700
0.20	1606
0.25	1530
0.30	1498
0.35	1406
0.40	1330
0.45	1266
0.50	1110
0.55	1070
0.60	930
0.65	865
0.70	816
0.75	797
0.80	780
0.85	735
0.90	670
0.95	664
1.00	660
1.05	595
1.10	560
1.15	546
1.20	530
1.25	512
1.30	480
1.35	472
1.40	465
1.45	454
1.50	446
1.55	438
1.60	432
1.65	426
1.70	420
1.75	410
1.80	402
1.85	379
1.90	361
1.95	348
2.00	340

14.9 APPENDIX 9 – Force calibration between weight and voltage

Axial Force Sensor		
Weight	Resistance	Voltage
	(kohms)	(volts)
0.20	760	5.00
0.25	630	4.97
0.30	540	3.65
0.35	440	1.09
0.40	384	-0.35
0.45	312	-2.67
0.50	285	-3.74
0.55	281	-3.93
0.60	228	-4.87
0.65	201	-5.00

Normal Force Sensor		
Weight	Resistance	Voltage
	(kohms)	(volts)
0.35	1606	4.99
0.40	1530	4.86
0.45	1498	4.65
0.50	1406	4.01
0.55	1330	3.41
0.60	1266	2.73
0.65	1110	1.30
0.70	1070	0.67
0.05	930	-0.68
0.65	865	-1.54
0.70	816	-2.31
0.75	797	-2.60
0.80	780	-2.70
0.85	735	-3.50
0.90	670	-4.45
0.95	664	-4.58
1.00	660	-4.60
1.05	595	-5.00

14.10 APPENDIX 10 -- Recirculation Data for Vehicle 3 sheet 1 of 2

0° Wing Angle of Attack

AOA	Tare Data		Raw Data		Actual Data	Lift
(Degrees)	R (kohms)	N (lbs)	R (kohms)	N (lbs)	N (lbs)	N (lbs)
0.00	644	0.67	466	1.26	0.59	0.59
2.00	635	0.70	423	1.40	0.70	0.70
4.00	605	0.80	397	1.49	0.69	0.68
6.00	592	0.84	346	1.65	0.81	0.81
8.00	586	0.86	345	1.66	0.80	0.79
10.00	604	0.80	334	1.69	0.89	0.88

5° Wing Angle of Attack

AOA	Tare Data		Raw Data		Actual Data	Lift
(Degrees)	R (kohms)	N (lbs)	R (kohms)	N (lbs)	N (lbs)	N (lbs)
0.00	640	0.68	440	1.34	0.66	0.66
2.00	642	0.68	395	1.49	0.81	0.81
4.00	621	0.75	359	1.61	0.86	0.86
6.00	608	0.79	332	1.70	0.91	0.91
8.00	602	0.81	288	1.85	1.04	1.03
10.00	585	0.87	282	1.86	1.00	0.98

10° Wing Angle of Attack

AOA	Tare Data				Raw Data	
(Degrees)	R (kohms)	N (lbs)	R (kohms)	N (lbs)	N (lbs)	N (lbs)
0.00	695	0.50	419	1.41	0.91	0.91
2.00	684	0.54	404	1.46	0.92	0.92
4.00	678	0.56	391	1.51	0.95	0.94
6.00	664	0.60	335	1.69	1.09	1.08
8.00	685	0.54	321	1.74	1.20	1.19
10.00	640	0.68	329	1.71	1.03	1.01

15° Wing Angle of Attack

AOA	Tare Data				Raw Data	
(Degrees)	R (kohms)	N (lbs)	R (kohms)	N (lbs)	N (lbs)	N (lbs)
0.00	657	0.63	388	1.52	0.89	0.89
2.00	632	0.71	348	1.65	0.94	0.94
4.00	540	1.01	242	2.00	0.98	0.98
6.00	594	0.84	262	1.93	1.10	1.09
8.00	602	0.81	271	1.90	1.09	1.08
10.00	612	0.78	320	1.74	0.96	0.95

14.10 APPENDIX 10 -- Recirculation Data for Vehicle 3 sheet 2 of 2

20° Wing Angle of Attack

AOA	Tare Data		Raw Data		Actual Data	Lift
(Degrees)	R (kohms)	N (lbs)	R (kohms)	N (lbs)	N (lbs)	N (lbs)
0.00	650	0.65	297	1.82	1.16	1.16
2.00	655	0.63	287	1.85	1.21	1.21
4.00	659	0.62	272	1.90	1.28	1.27
6.00	659	0.62	278	1.88	1.26	1.25
8.00	679	0.56	309	1.78	1.22	1.21
10.00	699	0.49	337	1.68	1.19	1.18